PATIENT-SPECIFIC MODELING OF THE BIOMECHANICS OF VULNERABLE
CORONARY ARTERY PLAQUES

by Mostafa Mahmoudi

A Dissertation

Submitted in Partial Fulfillment

of the Requirements for the Degree of

Doctor of Philosophy

in Bioengineering

Northern Arizona University,

August 2022

Approved:

Amirhossein Arzani, Ph.D., Chair

Thomas Acker , Ph.D.

Timothy Becker, Ph.D.

Kiisa Carla Nishikawa, Ph.D.

ABSTRACT

PATIENT-SPECIFIC MODELING OF THE BIOMECHANICS OF VULNERABLE CORONARY ARTERY PLAQUES

MOSTAFA MAHMOUDI

Coronary artery atherosclerosis is a local, multifactorial, complex disease, and the leading cause of death in the US. Complex interactions between biochemical transport and biomechanical forces influence disease growth. Wall shear stress (WSS) affects coronary artery atherosclerosis by inducing endothelial cell mechanotransduction and by controlling the near- wall transport processes involved in atherosclerosis. The current management guidelines for detection of atherosclerotic plaques focus on morphological characterizations and the blockage percentage of the stenosis based on coronary computed tomography angiography (CCTA). Despite the progress achieved in therapeutics, the relation between hemodynamic environment and the composition of atherosclerotic plaques remains unexplored. This dissertation is divided into two main sections: the association between hemodynamics/biotransport and longitudinal changes in the plaque vulnerability characteristics and developing a 1D automatic vascular network generation package with the ability to be coupled with a 3D patient-specific model.

Biochemical-specific mass transport models were developed to study low-density lipoprotein, nitric oxide, adenosine triphosphate, oxygen, monocyte chemoattractant protein-1, and monocyte transport. The transport results were compared with WSS vectors and WSS Lagrangian coherent structures (WSS LCS). High WSS magnitude protected against atherosclerosis by increasing the production or flux of atheroprotective biochemicals and decreasing the near-wall localization of atherogenic biochemicals. Low WSS magnitude promoted atherosclerosis by increasing atherogenic biochemical localization.

To find the association between hemodynamics/biotransport and longitudinal changes in the atherosclerotic plaque characteristics, a plaque quantification software was developed

with the aim of performing a segment-specific assessment to accurately calculate the volumes of low attenuation plaque (LAP), fibrous plaque (FP), calcium plaque (CP), and vessel wall and identify the quantitative plaque characteristics including spotty calcification, presence of napkin-ring sign, and positive remodeling. The changes in the different plaque characteristics were compared against the hemodynamic/biotransport parameters. The results showed that WSS magnitude is moderately correlated with the longitudinal changes in LAP, FP, and vessel wall volumes. Also, WSS magnitude and local concentration of nitric oxide (NO) showed a meaningful correlation with the presence of positive remodeling in the follow-up.

A hybrid 1D-3D solver was developed in *Simvascular* software and validated against the existing data in the literature. The results of our coupled 1D-3D solver showed a good agreement with the 3D, deformable wall models. This solver can be used to solve the blood flow in a large network of 1D vessels coupled with a patient-specific 3D model. Finally, an automatic vascular network generation framework was developed using the Constraint Constructive Optimization (CCO) algorithm to study the generation of arterial trees based on theoretical perfusion maps. The algorithm simulated angiogenesis by optimizing the total vessel volume governed by physiological and geometrical constraints.

Keywords: Coronary artery disease, Biochemical transport, Lagrangian coherent structures, Mechanotransduction, Endothelial cells, Hemodynamics, Longitudinal study, Vulnerable plaque quantification, coupled 1D-3D solver, Automatic arterial tree generation, Constraint constructive optimization.

ACKNOWLEDGMENTS

I would like to thank my esteemed supervisor – Dr. Amirhossein Arzani for his invaluable supervision, support and tutelage during the course of my PhD degree. His immense knowledge and plentiful experience have encouraged me in all the time of my academic research and daily life. Amir was everything a PhD student could ask for. He was always open to my new and crazy ideas and provided an environment where I could grow and choose my field of research. Spending half of my PhD during a global pandemic, Amir supported and advised me with patience throughout my journey. Whenever I had a question or a problem, I knew I could talk to Amir via a click of mouse on the 'Skype Call' and he was always ready to help. He taught me the art of presentation and always encouraged me to find conferences I liked so I could share my work with other researchers.

I would also like to acknowledge our collaborators. This dissertation could not be done without the support of many people. Thanks to Dr. Matthew Budoff and Dr. Kim-Lien Nguyen from David Geffen School of Medicine, UCLA, Dr. Alex Barker from University of Colorado, Dr. Jolanda Wentzel from Erasmus MC who provided us with the required datasets, medical images, and guidance. I would like to thank Dr. Kashif Shaikh and Dr. Shone Almeida for assistance in providing the CCTA data.

I wish to thank my committee members who were more than generous with their expertise and precious time. Thank you Dr. Thomas Acker, Dr. Timothy Becker, and Dr. Kiisa Carla Nishikawa for agreeing to serve on my committee. I am also very thankful to my very friendly lab-mates. Mohammadreza Soltany who helped me a lot during my first days, Milad Habibi, Maryam Aliakbari, and Ali Farghadan who provided an environment in the Cardiovascular Biomechanics Lab for everyone to grow and reach their goals.

TABLE OF CONTENTS

LIST OF TABLES

LIST OF FIGURES

DEDICATION

I dedicate my dissertation work to my family and many friends. A special feeling of gratitude to my loving parents whose words of encouragement and push for tenacity ring in my ears.

Chapter 1

Introduction

1.1 Longitudinal association between vulnerable plaque characteristics and the hemodynamic features

Cardiovascular diseases (CVDs) are responsible for one out of every three deaths in the United States [1]. The major form of CVDs is atherosclerosis, a progressive condition in which deposits of fatty and inflammatory material build up inside the arterial wall, create plaque, and obstruct the normal blood flow. Pathological studies have suggested that specific atherosclerotic plaques show shared features related to acute coronary syndrome (ASC) [2, 3]. Usually, these types of plaques, called vulnerable plaques, are unstable and typically do not show significant blockage of the coronary arteries. Recently, an effort has been organized to use coronary computed tomography angiography (CCTA) in high risk patients to investigate the presence of such vulnerable plaques [4, 5, 6].

Although the exact underlying mechanisms of atherosclerotic plaque growth are not fully understood, many scientists believe it begins with a damage to the inner wall of the artery,

called endothelial cell (EC) layer. It has been shown that ECs are sensitive to the biochemical and biomechanical environment surrounding them [7, 8]. When ECs are subjected to forces related to cardiac function, such as wall shear stress (WSS), they can alter their functions, activities, and even their phenotype [9, 10]. This leads to various physiological and pathophysiological changes in the arteries. On the other hand, a damage to ECs can change their permeability toward various biochemicals and cells, facilitating the transport of them into the vessel wall. The major biochemical and cells in blood flow that protect/prevent atherosclerosis are known to be low-density lipoprotein, nitric oxide, adenosine triphosphate, oxygen, monocytes, and monocyte chemoattractant protein-1. The localization or lack of them on the arterial wall is a key factor in progression of the disease.

Among the aforementioned biochemicals and cells, LDL is one of the most important players in the atherosclerosis. As an atherogenic biochemical, presence of LDL macromolecules inside the arterial wall tissue releases bio-signals to the immune system and causes inflammation inside the vessel wall [11]. On the other hand, nitric oxide is an atheroprotective biochemical which regulates the vascular tone and permeability of ECs. It's been shown that NO plays an important role in preventing excessive transport of monocytes and T-cells into the arterial wall and decreasing the rate of LDL oxidation. It's been shown that production of NO inside the arterial wall depends on the exerted WSS.

Arguably, WSS is the most important factor in the biomechanics of atherosclerosis. WSS provides valuable information about the near-wall biotransport and also can directly affect the ECs mediated regulation of vascular health by means of mechanotransduction [12, 13]. Mechanotransduction is the process of converting mechanical forces into a series of bio-signals. It has been shown that various mechanosensors exist inside and on the surface of ECs. These mechanosensors consist of ion channels, G-proteins, receptors for vascular endothelial growth factor type-2, adhesion molecules, and the endothelial glycocalyx [7, 8, 14, 15].

Extracting the hemodynamic and biotransport *in vivo* data for coronary arteries is close

to impossible. Computational fluid dynamics (CFD) provides this opportunity to study the hemodynamics and biotransport in small arteries using the physiologic-derived principals. With recent advances in medical imaging techniques, researchers are able to reconstruct the coronary arteries from CCTA images with acceptable accuracies. However, most of the patient-specific studies are focused on the blood flow patterns and hemodynamics. Unfortunately, the high resolution, patient-specific study of near-wall transport of various biochemicals has not gained attention.

Although the patient-specific studies provide a detailed representation of hemodynamics and biotransport in coronary arteries and improve our understanding of the flow conditions in diseased and healthy arteries, the results of them should be correlated to the longitudinal progression of the atherosclerosis. In recent years, an effort to associate the hemodynamics features in the baseline to the longitudinal changes in the volume of the plaques has gained momentum [16, 17]. However, the association of hemodynamic and biotransport to vulnerable plaque characteristics is a new perspective in bioengineering field. This type of study needs high resolution CCTA images, a control group of patients, access to plaque quantification software, and registration of CCTA images with 3D CFD results. Currently, there is no platform that offers the scientists all the required technologies to study the effect of biotransport and hemodynamics on the vulnerable plaque characteristics.

1.2 Automatic generation of vascular networks

The cardiovascular system consists of various sections which each has its own physiological and functional behavior. The patient-specific 3D models are well suited for studying the effect of geometry on the blood flow [18, 19]. However, the use of 3D models to simulate the blood flow inside a large network of vessels is impractical. In the case of coronary arterial tree, the CCTA images only can visualize the arteries to a certain extent and they miss the

3

structure of the arterial network with small diameters. Also, the high resolution 3D modeling of the arterial tree, considering the deformable arterial wall, is computationally expensive. The deformability of the arterial wall plays a role in the propagation of pressure waves from the heart to the distal arteries [20, 21]. These waves play an important role in regulating the blood pressure in the coronary arteries. Thus, the simulation of the entire arterial network supplying blood to the heart tissue faces two limitations: computational cost and lack of medical imaging technology to capture the structure of a large network of vessels.

To resolve the aforementioned limitations, 1D models have been developed as an alternative to describe the arterial network. The 1D models provide the opportunity to obtain the large scale characteristics of hemodynamics at different sections of the arterial network [22]. It has been shown that the current non-linear 1D models of hemodynamic can generate accurate pressure and flow waveforms inside an arterial network. One of the major limitations of the 1D models is their incapability in simulating the small scale flow features. These small-scale feature include the flow structure in the plaque region, flow structure around bifurcations, and local measurement of WSS. The multiscale approach of coupled 1D-3D can address the limitations regarding the small-scale flow structures in region of interest (3D) and the computational cost of simulating a network of arteries with deformable walls (1D) [23]. Unfortunately, no open-source software provides the option of a hybrid 1D-3D simulation.

To address the limitation regarding the resolution of medical images, various arterial tree generation algorithms have been developed. These algorithms are governed by mathematical and physiological principals derived from anatomical data. These detailed models of vascular tree made it possible to quantitatively analyze the blood flow distribution inside a large network of vessels. The most well-known algorithm to generate arterial networks is Constrained Constructive Optimization (CCO) [24, 25]. This algorithm uses Poiseuille's law for simulating the blood flow and uses physiological-derived laws such as Murray's law for creating the bifurcations. CCO is an iterative approach and starts from a starting node called

the root. Root is the most proximal segment that supplies blood to the arterial network. It has been shown that CCO results in a qualitatively sound arterial network structures. There are limitations on the use of CCO algorithm that mostly are related to the various assumptions made to develop the model. The most important assumptions in CCO are as follows: (1) The arterial network segments are solid straight cylinders, (2) the vessel wall is rigid, (3) Blood behaves as a Newtonian, incompressible fluid, (4) The pressures at the terminal segments are equal, (5) Symmetric branching pattern, and (6) terminal nodes are added randomly.

1.3   Thesis outline and objectives

The thesis is divided into two main sections: the association of hemodynamic and biotransport at baseline to the changes in vulnerability characteristics of atherosclerotic plaques, and developing a framework to automatically generate a vascular tree based on perfusion maps using a hybrid 1D-3D approach. In Chapter 2 the high resolution patient-specific simulations of coronary arteries showing atherosclerosis are presented and the underlying CFD methods are described. In Chapter 3, the steps in developing a plaque quantification software and the algorithms used to increase the accuracy of the quantification process are described in details. Then, the developed software was used to quantify the longitudinal changes in the plaque characteristics from baseline to follow up. Finally, the correlations between the hemodynamic/biotransport results from Chapter 1 and the changes in various vulnerable plaque features are presented. Chapter 4 discusses the development of a hybrid 1D-3D solver in the open-source software package *Simvascular*. The validation results for the developed coupled 1D-3D solver are discussed. In Chapter 5, the algorithm behind the CCO algorithm for arterial tree generation is discussed in details and the results of applying this approach to theoretical perfusion maps are presented. Chapter 6 summarizes the most

important findings of the present dissertation and outlines the future work.

Chapter 2

The story of wall shear stress in coronary artery atherosclerosis: biochemical transport and mechanotransduction

2.1 Introduction

2.1.1 Overview

Atherosclerosis is the major form of cardiovascular disease and the leading cause of mortality and morbidity in the US. This progressive condition is a process in which deposits of fatty and inflammatory material build up inside arterial walls, create plaques, and obstruct normal blood flow. Atherosclerotic plaques are commonly developed in the coronary arteries and the resulting thrombus formed after their rupture can ultimately occlude an artery downstream

to the plaque causing myocardial infarction. This inflammatory disease is characterized by endothelial dysfunction [2], immune cell migration and differentiation [10], and extracellular matrix remodeling [2, 3]. Although the exact causes of atherosclerosis are still not fully understood [26], many scientists believe it begins with damage to the inner wall of an artery, called the endothelium [27]. The endothelial cells (ECs) sit at the interface between blood flow and the arterial wall and tend to be sensitive to their biomechanical and biochemical environment [28].

Elevated levels of low-density lipoprotein (LDL) in blood increase the risk of developing coronary artery atherosclerotic plaques. The circulating LDL macromolecules do not directly contribute to atherosclerosis, however, when they penetrate the arterial wall in atherogenic regions, because of the presence of free radicals in the intima, they become oxidized (ox-LDL) [11]. This is believed to be the first stage of atherosclerotic plaque formation. The ox-LDL in intima launches an immune response by ECs and smooth muscle cells (SMC) in which monocyte chemoattractant protein-1 (MCP-1) is secreted by the ECs [10]. MCP-1 signals the recruitment of monocytes and T-cells by the ECs. Then, monocytes and T-cells squeeze into the gaps between ECs, differentiate into macrophages, devour apoptotic cells, and endocytose the ox-LDL turning them into foam cells [9]. By secreting interleukin IL-12, the foam cells activate T-cells in the intima leading to secretion of interferon INF-γ, promoting more monocytes recruitment to the site [29]. Meanwhile, as a response to chemical signals, smooth muscle cells (SMCs) migrate towards the foam cells forming a fibromuscular cap on the lesion. The disease can slowly progress and the resulting plaque may ultimately reduce blood flow supply to the downstream tissue.

Biomechanical and biochemical cues strongly regulate the process of atherosclerosis. When ECs are subjected to forces such as wall shear stress (WSS) and mechanical stretch, their functions, activities, integrity, as well as their phenotype might be altered, resulting in physiological and pathophysiological changes in blood vessels [9, 10]. The dysfunctional ECs

8

at regions susceptible to atherosclerosis show a change in the permeability of endothelium, facilitating the transport of various biochemicals and cells into the subendothelial layer [30, 31, 32]. The major biochemicals and cells in blood that promote or protect atherosclerosis growth are known to be low-density lipoprotein (LDL) [33, 34, 35, 36], nitric oxide (NO) [37, 38, 39], adenosine triphosphate (ATP) [40, 41, 42], oxygen [43, 44, 45], monocytes [46, 47, 48] and monocytes chemoattractant protein-1 (MCP-1) [49, 50]. The surface concentration, flux, and transport of each of these biochemicals/cells play a unique role in the development of disease at regions with dysfunctional endothelium [46].

2.1.2 Important biochemicals

LDL is likely one of the most important biochemical players in atherosclerosis and has been the main focus in biochemical studies related to atherosclerosis. While in earlier studies, it was assumed that the endothelium shows a constant permeability and diffusivity [51], more recent publications are taking advantage of *in vitro* experiments on cultured ECs and assume more complex shear-dependent permeability for the transport of LDL into the arterial wall. The most promising model, which considers various transport pathways in the endothelium is called the three-pore model [52, 53]. This model accounts for the WSS-dependent pathways that LDL molecules can penetrate through the endothelium, i.e. vesicular pathway, leaky junctions, and normal junctions [54, 55]. Monocytes are the other important atherogenic player that together with LDL perform a crucial role in creating atherosclerotic plaques. Monocyte transport has been studied using discrete Lagrangian models [56] as well as aggregated continuum models [46].

NO is an atheroprotective biochemical mediating vasodilation. It is well established that NO lowers vascular tone through endothelium-derived hyperpolarizing factor (EDHF) [12], reducing the EC permeability by inhibiting the translocation of cell adhesion molecules [9,

13], preventing excessive transport of monocytes into the arterial wall, and slowing down the rate of LDL oxidation [57]. The transport and production of NO strongly depends on the exerted WSS from the blood flow on the ECs. Various *in vitro* studies have shown that NO production is elevated with higher WSS magnitude [58, 59, 60]. Based on this observation, computational models are introduced to simulate the transport of NO in arteries [38, 37, 61].

Adenine nucleotide ATP is another atheroprotective biochemical. ECs are known to trigger mobilization of intracellular calcium in response to shear stress signals [62, 9]. It has been shown that intracellular calcium changes through mechanotransduction signaling by ECs and surface concentration of ATP is believed to affect the calcium mobilization. Also, another key role ATP plays is mediating the vasodilation and vascular tone [63]. Finally, oxygen is known to protect against atherosclerosis [45]. Hypoxia (lack of oxygen) is one of the initial steps in the formation of atherosclerotic lesions [45]. *In vitro* studies showed that disturbed flow, as well as hypoxia due to reduced oxygen transport, promote EC dysfunction by activation of hypoxia-inducible factor-1α (HIF1-α) [45].

2.1.3   Role of biomechanics and study design

The importance of WSS in the pathology of atherosclerosis has been well accepted by the research community and is arguably the most important parameter in the biomechanics of atherosclerosis [64]. Our group has shown that WSS provides valuable information about near-wall biotransport [65, 61]. It is also known that WSS directly affects EC mediated regulation of vascular health through mechanotransduction [28, 66]. WSS affects biotransport processes via an interplay between WSS-mediated EC permeability/flux and near-wall localization of biochemicals controlled by WSS topology (stable and unstable manifolds in the WSS vector field) [61]. Additionally, WSS regulation of atherosclerosis via mechanotransduction is well studied and understood [3]. These biochemical and biomechanical pathways

are both important in atherosclerosis, and they are both strongly influenced by WSS, albeit with different mechanisms. The goal of this study is to first review our knowledge of WSS-mediated mechanotransduction in atherosclerosis, perform a comprehensive investigation of atherogenic and atheroprotective biotransport processes in patient-specific coronary artery geometries, and finally summarize our knowledge of how WSS influences atherosclerosis.

The manuscript is structured as follows. First, in Sec. 2.1.4, we review our prior knowledge of shear stress and mechanotransduction in atherosclerosis. Subsequently, we explain our patient-specific computational fluid dynamics (CFD) procedure for obtaining hemodynamics data in left anterior descending and left circumflex arteries in four human coronary arteries with atherosclerotic lesions (8 models total) as well as two healthy left anterior descending artery swine models. We explain the biochemical transport models (NO, ATP, oxygen, LDL, MCP-1, and monocyte) and WSS processing. Finally, the results are presented and discussed. We summarize our findings and present them with the goal to move towards a comprehensive hypothesis for WSS in atherosclerosis.

2.1.4   Wall shear stress (WSS) and mechanotransduction

The role of ECs cannot be underestimated as only an interface and barrier between blood flow and the underlying tissues. The ECs actively regulate various pathways in atherosclerosis ranging from the recruitment of immune cells and regulation of vascular tone to changing the permeability to various biochemicals and cells. ECs can also sense mechanical forces such as WSS, which is the frictional force exerted from the blood flow onto the ECs. The ECs sense these mechanical forces and respond to them in the form of biochemical formation, cell shape change, cell proliferation, protein secretion, and alteration of gene expression. The process of converting mechanical forces into a series of biochemical signaling events is called mechanotransduction [67]. In this section, we will provide a mini-review on how WSS affects

the EC mechanotransduction in atherosclerosis.

The endothelium consists of a monolayer of polygonal ECs covering the blood vessel wall and providing a barrier to keep the plasma and blood cells in the lumen. ECs are connected in an edge-to-edge pattern [7]. The structure of ECs consists of an actin-myosin cytoskeleton, intercellular clefts, gap junctions, glycocalyx, caveolae, and vesicles. Different mechanosensors are present on the EC surface and can sense WSS signals. Some known EC mechanosensors include ion channels [7], G-proteins [8], receptors for vascular endothelial growth factor type 2 (VEGFR2) [14], adhesion molecules (e.g., platelet endothelial cell adhesion molecules PECAM-1) [68], primary cilium [69], and the endothelial glycocalyx [15].

In vivo studies show that pro-inflammatory genes can be activated in ECs in regions with disturbed blood flow [70, 71, 8]. Disturbed flow is loosely defined in the literature, however, the common consensus is that low (< 0.4 Pa) and oscillatory (lack of a dominant time-average direction) shear stress define disturbed flow [72]. It is well established that disturbed flow activates a series of responses in ECs. For example, low/disturbed WSS triggers induction of KLF4 in ECs [73, 74], activation of sterol regulatory element-binding protein 2 (SREBP2) [75, 76], expression of adhesion molecules and cytokines via nuclear factor NF-κB [3, 77], and activation of HIF1-α [78], while physiological WSS mediates NO production as a result of endothelial nitric oxide synthase (eNOS) enzyme expression [79, 80], activates integrins [81], and regulates Ca^{2+} concentration [82].

The glycocalyx is the first contact point between blood flow and the ECs in sensing the WSS and has received notable attention in recent years [32]. The glycocalyx protein complex includes sialoglycoprotein, syndecan-1, glypican, and hyaluronan, which are linked to the cortical actin cytoskeleton and potentially transduce the WSS signals into the EC cytoskeleton [83, 84]. Another prominent mechanism for sensing WSS is lateral diffusion and molecular translocation [9]. The translocation of P-selectin into the surface of ECs in the presence of an inflammatory agonist or shear stress is one example of this process.

Stress fibers are another crucial component of ECs and are bundled inside the cortical actin. The stress fibers are connected to the core proteins in glycocalyx on the surface of ECs, linked to transmembrane proteins such as integrin, and are connected to the neighboring ECs by vascular endothelial cadherin (VE-cadherin) [85]. One of the key functions of stress fibers is regulation of cell adhesion. The stress in these filaments is transmitted to the focal adhesion sites activating integrin and reinforcing the cytoskeleton by changing the shape of stress fibers [86]. It is believed that stress fibers structure affect the EC shape, polarity, and orientation based on the WSS patterns [87]. The stress fibers inside ECs are disassembled and generated periodically [88] and when the stress is released from the stress fibers, they become degraded and under shear stress the actin filaments are formed in a direction parallel to the applied shear stress, transmitting the stress to the focal adhesion sites.

Focal adhesions, comprised of protein complexes, provide sites where integrins bind to the extracellular matrix (ECM). They are mechanosensors, which contain a high density of actin-binding proteins such as α-actinin, talin, vinculin, zymin, and Src tyrosine kinase (called focal adhesion kinase FAK) [81]. Focal adhesions are capable of sensing signals coming from WSS. It has been shown that some of these proteins change their activity depending on the applied force [89]. Also, shear stress affects the cellular polarization and alignment of ECs via activating the small G-proteins at focal adhesions and forming the stress fibers in sites close to the applied stress. Regions with an aligned stress fiber network in the direction of applied physiological WSS are shown to suppress atherogenesis, while stress fiber networks under low and oscillatory forces promote atherosclerosis. Under pathological shear stress or activation of mechanoreceptors such as PECAM-1, integrins increase their affinity towards ligands. As a result, the cell adhesion molecules (CAMs) undergo a conformational change and control the adhesion of monocytes to ECs [75].

Physiological and high WSS values stimulate endothelial nitric oxide synthase (eNOS) phosphorylation via FAK and shear stress dependent Ca^{2+} channels [82]. This leads to subsequent

NO production and flow-induced vasodilation, which protect against atherosclerosis. It is reported that inflamed tissues with dysfunctional ECs show a drop in the concentration of NO and Ca^{2+} [80]. Also, shear-dependent expression of CAMs via NF-κB, such as ICAM-1, VCAM-1, and E-selectin under low/disturbed WSS contributes to the early formation of atherosclerosis lesion [90, 32]. The shear-dependent NF-κB-mediated gene expression regulated by PECAM-1 reduces NO production and promotes atherosclerosis.

The permeability of ECs toward various biochemicals/cells affects atherosclerosis progression. The permeability of endothelial intercellular clefts is not constant and it changes in response to WSS and biochemical signaling. It is known that NO production as well as endothelial cyclic guanosine monophosphate (cGMP) mediate the permeability of ECs [91]. Through mechanosensitive processes, integrins, by activation of NF-κB, regulate the EC permeability, while caveolin-1 can mediate the gap junctions and regulate the transport of macromolecules like LDL into the arterial wall. While monocytes can penetrate through the gap junction by squeezing themselves, LDL molecules cannot easily pass the endothelium. It has been shown that the permeability of ECs towards LDL macromolecules depends on the number of mitotic cells and leaky junctions [34]. *In vitro* studies showed that the number of leaky junctions in cultured ECs increased in low WSS regions [34].

2.2   Methods

2.2.1   Image processing

Coronary computed tomography angiography (CCTA) images from four human patients (left anterior descending LAD and left circumflex LCx arteries, in total 8 models) and two healthy swine models (LAD) were collected, de-identified, and securely stored with IRB approval. The human patients were part of the "Effect of Aged Garlic Extract (AGE) on Improv-

ing Coronary Atherosclerosis in People With Type 2 Diabetes Mellitus" clinical trial [92]. Individuals with a bodyweight > 300 lbs, a history of bleeding disorders or those taking anticoagulants, those with hypertensive encephalopathy or a cerebrovascular event, a known history of coronary artery disease, myocardial infarction, stroke or life-threatening arrhythmia within the prior 6 months were excluded from the study. The following imaging and reconstruction variables were applied: slice thickness of 0.625 mm, tube voltage 100–120 kV, tube current 350–780 mA and a matrix size of 512×512 with x- and y-axis resolution of $0.3516mm$. The human patients showed multiple atherosclerotic plaques in their coronary artery tree. The patient information and plaque characteristics are presented in Table 2.1, and the 10 reconstructed luminal surfaces of coronary arteries are shown in Fig. 2.1. For human patients, the arterial centerlines were created by following the lumen cross-sections between CCTA slices and 3D patient-specific models were created using the open-source software package SimVascular [93]. Because of the anatomical complexity in coronary arteries, cross-sectional segments were created manually to capture the fibrous and calcified plaques. Using Hounsfield units (HU) allows differentiation of plaques into noncalcified, mixed, and calcified plaque classes. In this study, regions with HU value of 79 ± 34 were considered as lipid-rich plaque, 90 ± 27 as fibrous plaque, and 772 ± 251 as calcified plaque [94]. Figure 2.2 shows an example of calcified plaque, the 3D rendition of CCTA images for Patient 1, and an overview of the hemodynamic analysis performed. For swine models, the fusion of intravascular ultrasound (IVUS) and CCTA is used to reconstruct the 3D arterial models, as explained in [95, 96].

2.2.2 Computational fluid dynamics (CFD)

After locally smoothing the arterial bifurcations using a volume preservation method, a mesh with 4 boundary layers next to the wall (global edge size of 0.015cm and first boundary layer size of 0.006cm) is generated in SimVascular. For transport models, another mesh is created

Table 2.1: Plaque characteristics of different patients from coronary computed tomography angiography (CCTA).

Patient ID	Age	Sex	Comments
P1	35	M	Both soft and calcified plaques in LAD artery; the soft plaque starts before the 1st diagonal/ LAD bifurcation connecting to the calcified plaque. The maximum blockage is 46%. In LCx, both soft and calcified plaques are located between 1st and 2nd marginal branches. The maximum blockage is 21%.
P2	64	F	An elongated soft plaque in LAD artery; the soft plaque starts right after 1st diagonal and ends before LAD/2nd diagonal bifurcation. The maximum blockage is 57%. Small calcified plaque in LCx artery; the plaque is located at proximal LCx. The maximum blockage is 23%.
P3	51	M	Three calcified plaques in LAD; one right before LAD/1st diagonal bifurcation; one before LAD/2nd diagonal bifurcation; and the other one at the proximal part of 2nd diagonal branch. The maximum blockage is 6%. Multiple small calcified plaques in LCx; plaques are located at proximal LCx and around the LCx/1st marginal branch. The maximum blockage is 18%.
P4	59	M	Multiple soft and calcified plaques in LAD; plaques are located between 1st and 2nd diagonal branches. The maximum blockage is 21%. Multiple soft and calcified plaques in LCx; plaques are scattered between proximal LCx artery and 2nd marginal branch. The maximum blockage is 17%.
P5 P6	-	-	LAD artery from 2 adult familial hypercholesterolemia Bretoncelles Meishan mini-pigs with a low-density lipoprotein receptor mutation fed a high fat diet were considered. Baseline data without plaque were selected.

with 10 boundary layers with global edge size of 0.009cm where the first layer is considered to be $5.0\mu m$ in size to capture thin concentration boundary layers that arise in cardiovascular mass transport problems [97, 98]. Table 2.2 lists the total number of elements in the meshes for different models used in this study. For CFD and mass transport simulations, quadratic elements (P2-P1 elements) and linear elements are used, respectively. A sample of the cross-sectional 3D mesh in the plaque region of P1-LCx is shown in Fig. 2.2.

Table 2.2: Number of elements used for CFD and mass transport simulations.

	Number of elements									
	P1		P2		P3		P4		P5	P6
	LAD	LCx	LAD	LCx	LAD	LCx	LAD	LCx	LAD	LAD
CFD	3 M (24 M)*	3 M (24 M)	7 M (56 M)	4.7 M (37.6 M)	3.2 M (25.6 M)	3.6 M (28.8 M)	2.4 M (19.2 M)	3.7 M (29.6 M)	5 M (40 M)	3.8 M (30.4 M)
Transport	6.6 M	11 M	7 M	7.2 M	6.1 M	5.2 M	4.4 M	4.1 M	5 M	5.5 M

* The number in parenthesis is the number of equivalent linear elements.
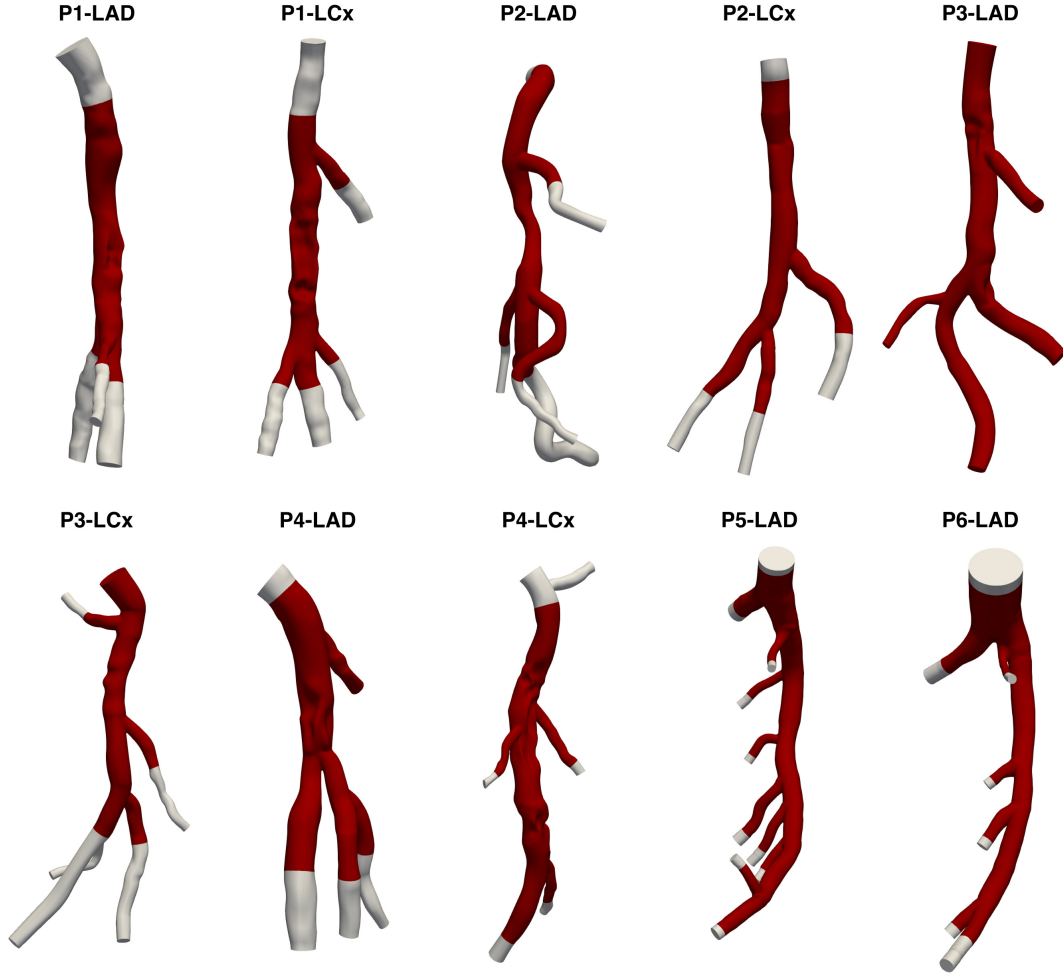
Figure 2.1: Geometry of the 10 coronary artery models used in blood flow simulations. Patient 1-4 models include human left anterior descending (LAD) and left circumflex (LCx) artery models with plaques; 5–6 are healthy swine LAD models. The red color indicates the region of interest for solving the transport of various biochemicals and cells.

CFD simulations are carried out using the open-source software package Oasis [99]. Oasis offers minimally dissipative (without any stabilization) fractional step solvers for Navier-Stokes and leverages the flexible Python interface offered by FEniCS to implement the governing equations in a finite element framework. A physiological pulsatile waveform using a parabolic velocity profile is applied as the inflow condition at the beginning of LAD and LCx arteries based on the waveforms reported in [100]. Resistance boundary conditions are prescribed at the outlets and tuned iteratively such that the flow rates obey the physiological scaling law for coronary arteries [101]. The resistance tuning is performed using a custom code devel-
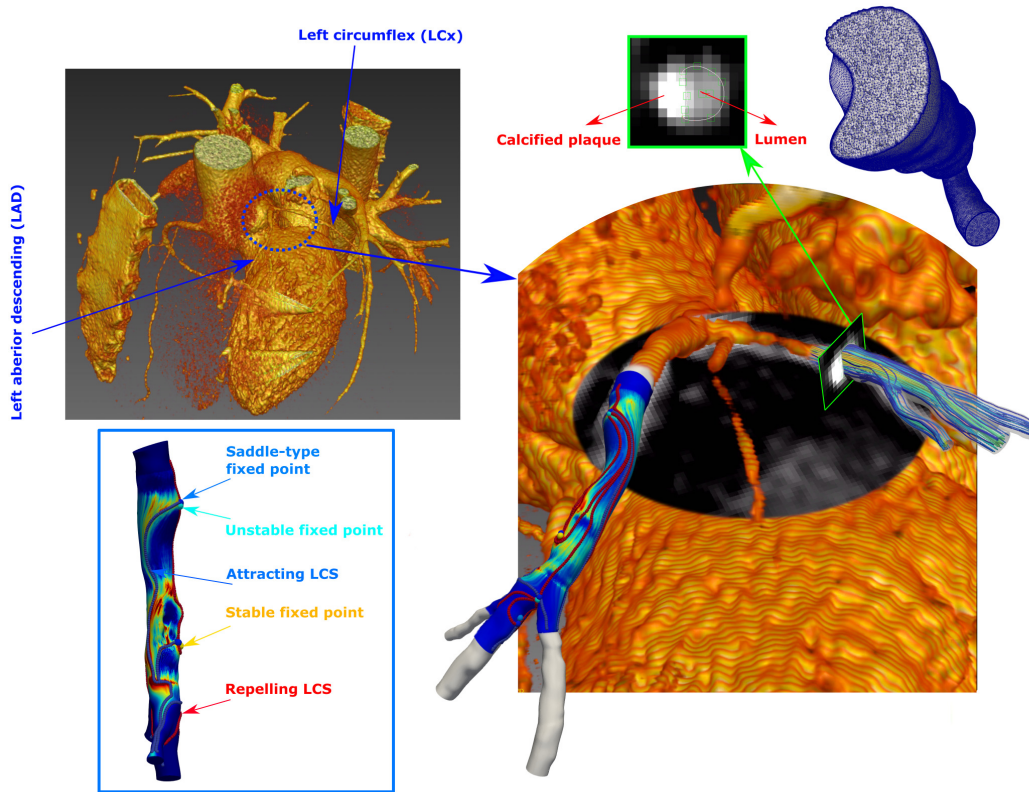
Figure 2.2: An overview of the analysis performed in this study is shown. 3D render of the CCTA images is shown for P1. In the right panel, an example of luminal segmentation, computational mesh, blood flow streamlines in LAD, luminal surface concentration of LDL, as well as WSS Lagrangian coherent structures (WSS LCS) for P1-LCx in the presence of a calcified plaque are shown. Different types of fixed-point and WSS topological features alongside with the color code used for visualization of them in the present paper are shown in the bottom-left panel.

oped in FEniCS/Oasis to reach the desired outflow distribution. A total number of 20,000 time-steps per cardiac cycle are used for all simulations. The large number of time-steps is necessary due to the high spatial resolution (quadratic elements). Blood is assumed to be Newtonian [102] with μ=0.04P and ρ=1.06 g/cm^3. The arterial wall is assumed to be rigid, which is a reasonable assumption in coronary arteries [103]. The 3D coronary artery models as well as the regions of interest for solving the transport equations are shown in Fig. 2.1. The region of interest in each model is chosen in a way that includes all of the plaques and extends to a point in the arterial branches where there is no flow recirculation.

2.2.3 Wall shear stress (WSS) analysis

WSS Lagrangian coherent structures (WSS LCS) have provided a new theory for the role of WSS in regulating near-wall biotransport processes in cardiovascular flows [104, 65]. These structures appear as lines that are embedded within the wall surface. WSS LCS are computed from stable/unstable manifolds of time-averaged WSS (TAWSS) vector field. The direct calculation of WSS manifolds from the steady TAWSS vector field is computationally efficient and takes less than a few seconds on a desktop. More details around calculation of WSS LCS are provided in our prior publications [65, 105]. Recently, a simple Eulerian method based on WSS divergence has also been proposed to identify WSS manifolds [106]. The attracting WSS LCS (unstable manifolds) attract biochemicals in their vicinity and lead to near-wall accumulation of biochemicals. The repelling WSS LCS (stable manifolds) tend to push away biochemicals by forming near-wall transport barriers. Additionally, stable and unstable type fixed points in the WSS vector field influence surface concentration patterns [105]. The stable and unstable WSS fixed points are points where the WSS vector is zero and the surrounding vectors point towards and away from the fixed point, respectively [105]. A dramatic change in WSS directionality occurs around these fixed points that could lead to locally elevated or decreased surface concentration.

2.2.4 Biotransport analysis

In the following, the models utilized to simulate the near-wall transport of low-density lipoprotein (LDL), nitric oxide (NO), adenosine triphosphate (ATP), oxygen, monocytes, and monocytes chemoattractant protein-1 (MCP-1) are provided. The values of the parameters used in these models are reported in Table 2.3.

The surface concentration and flux of various biochemicals are obtained by solving the proper advection-diffusion-(reaction) equations. The wall boundary conditions are extracted from

19

previous *in vitro* studies. The instantaneous velocity field obtained from hemodynamic simulation was used in transport equations and was interpolated to the more resolved transport mesh using Python codes developed with the visualization toolkit (VTK) libraries. The initial condition for solving each biochemical/cell transport was set to zero. Since the prescribed parabolic velocity boundary condition is of 3D nature and the instantaneous velocities were used in the transport governing equations, the sensitivity to the initial condition is reduced [107]. Given the nonlinearities present in cardiovascular flows, it is important to use a method capable of resolving high temporal frequencies. In this paper, the generalized-α method [108] was incorporated in a stabilized finite element formulation with a time-step of 2×10^{-4} s. The quasi-steady luminal surface concentration/flux was obtained after 10 cardiac cycles for NO, ATP, and oxygen, 15 cardiac cycles for monocytes and MCP-1, and 80 cardiac cycles for LDL concentration. Due to the small diffusivity and the highly heterogeneous permeability and flux boundary condition in LDL simulations, a large number of cardiac cycles were required to reach a quasi-steady solution. All simulations were performed using codes developed in the open-source finite element solver FEniCS and all of the results were visualized in ParaView.

Low-density lipoprotein (LDL) transport

Transport of LDL, a cholesterol carrying biochemical, into the arterial wall is one of the early stages of atherosclerosis. To model the transport of LDL, a three-pore model is utilized to account for the three pathways responsible for the transport of LDL into the arterial wall. i.e., the vesicular pathway, the normal junctions, and the leaky junctions [34]. The transport equation for LDL is written as

$$\frac{\partial c_{LDL}}{\partial t} + u \cdot \nabla c_{LDL} = D_{LDL} \nabla^2 c_{LDL} \ , \tag{2.1a}$$

$$- D_{LDL} \frac{\partial c_{LDL}}{\partial n} = -P_{app} c_{LDL} \ ; \text{Wall boundary condition,} \tag{2.1b}$$

where $P_{app} = P_v + P_{app,nj} + P_{app,lj}$ is the apparent permeability of ECs, in which the effects of vesicular pathways (P_v), normal junctions ($P_{app,nj}$), and leaky junctions ($P_{app,lj}$) are taken into account. Normal junctions block the transport of solutes with a radius larger than 2 nm. Thus, LDL molecules, having a radius of 11 nm, cannot pass through normal junctions ($P_{app,nj} = 0$) [109]. It is shown that leaky junctions are responsible for 90% of LDL transport [34]. The apparent permeability of leaky junctions depends on the fractional reduction factor in LDL concentration gradient at the pore entrance (Z_{lj}), diffusive permeability (P_{lj}), volume flux ($J_{v,lj}$), and solvent-drag reflection coefficient ($\sigma_{f,lj}$) of leaky junctions as follows:

$$P_{app,lj} = P_{lj} Z_{lj} + J_{v,lj}(1 - \sigma_{f,lj}) \ , \tag{2.2}$$

where $Z_{lj} = Pe_{lj}/exp(Pe_{lj} - 1)$, and the modified Péclet number is defined as $Pe_{lj} = J_{v,lj}(1 - \sigma_{lj})/P_{lj}$. The volume flux is $J_{v,lj} = L_{p,lj} \Delta P$ where the hydraulic conductivity is $L_{p,lj} = \frac{A_p}{S} L_{p,slj}$. The hydraulic conductivity of a single leaky junction is $L_{p,slj} = \frac{w^2}{3\mu_p l_{lj}}$ and the fraction of surface area occupied by the leaky junctions is $\frac{A_p}{S} = \frac{4w}{R_{cell}} \phi$. The fraction of leaky junctions is $\phi = \frac{\#LC \times \pi R_{cell}^2}{\text{unit area}}$, in which number of leaky cells is $\#LC = a_1 + a_2(\#MC)$, number of mitotic cells is $\#MC = b_1 exp(b_2 SI)$, and the EC shape index is defined based on time-average WSS (TAWSS) as $SI = c_1 exp(c_2 TAWSS) + c_3 exp(c_4 TAWSS)$. The diffusive permeability of leaky junctions is as follows

$$P_{lj} = \frac{A_P}{S} \Phi_{lj} P_{slj} \ , \tag{2.3}$$

where $\Phi_{lj} = 1 - \alpha_{lj}$ is the partition coefficient and $\alpha_{lj} = a/w$ is the ratio of the pore area available for LDL transport to the total pore area. The diffusive permeability of a single leaky junction is $P_{slj} = D_{lj}/l_{lj}$ where $D_{lj} = D_{LDL}\Phi F(\alpha_{lj})\frac{A_p}{S}$ and $F(\alpha_{lj})$ is the hinderance factor in a pore given in [110]. A constant LDL concentration $c_{LDL,0}$ is applied at the inlet. The values of the parameters used in three-pore model are reported in Table 2.3.

Nitric oxide (NO) transport

NO is an atheroprotective biochemical produced by the ECs. NO plays various positive roles in the prevention of atherosclerosis such as preventing smooth muscle cell migration and monocyte adhesion, reducing EC permeability, and suppressing platelet adhesion [111]. The equations governing the transport of NO can be written as [37, 38]

$$\frac{\partial c_{NO}}{\partial t} + u \cdot \nabla c_{NO} = D_{NO}\nabla^2 c_{NO} - K_d c_{NO} , \tag{2.4a}$$

$$- D_{NO}\frac{\partial c_{NO}}{\partial n} = -d \times (R_{basal} + R_{max}\frac{WSS}{WSS + WSS_0}) \text{ ; Wall boundary condition,} \tag{2.4b}$$

where K_d is NO degradation, d is the EC thickness, WSS is the wall shear stress magnitude, WSS_0 is a reference WSS value, and R_{basal} and R_{max} are the basal and maximum NO production rates, respectively. Since NO has a short half-life in blood [112], zero concentration is applied at the inlet.

Adenosine triphosphate (ATP) transport

ATP is an important biochemical that induces the production of vasoactive substances by the ECs, and therefore plays a positive role in preventing atherosclerosis [113]. The near-wall transport of ATP is governed by [114, 115]

22

$$\frac{\partial c_{ATP}}{\partial t} + u \cdot \nabla c_{ATP} = D_{ATP} \nabla^2 c_{ATP} \,, \tag{2.5a}$$

$$- D_{ATP} \frac{\partial c_{ATP}}{\partial n} = - \frac{V_{max} c_{ATP}}{K_m + c_{ATP}} + S_{max}[1 + exp(\frac{-WSS}{WSS_0})] \; ; \text{Wall boundary condition}, \tag{2.5b}$$

where V_{max} is the maximum enzyme reaction velocity for ATP hydrolysis, K_m is the Michaelis constant for the enzyme, S_{max} is maximum ATP release rate, WSS is the wall shear stress magnitude, and WSS_0 is the reference shear stress that regulates the rate at which the maximum ATP release is attained. The first term on the right-hand side of Eq. 2.5b describes the kinetics of ATP hydrolysis and the second term accounts for ATP release due to shear stress. A constant ATP concentration $c_{ATP,0}$ is used at the inlet.

Oxygen transport

It is believed that reduced availability of oxygen at the wall is a key factor in the development of atherosclerotic plaques [45]. The equation governing the transport of oxygen from blood to the arterial wall could be written as [116]

$$\frac{\partial c_{O2}}{\partial t} + u \cdot \nabla c_{O2} = D_{O2} \nabla^2 c_{O2} \,. \tag{2.6}$$

Constant oxygen concentrations of $c_{O2,0}$ and $c_{O2,w}$ are applied at the inlet and the blood-arterial wall interface, respectively [116].

Monocyte and monocyte chemoattractant protein-1 (MCP-1) transport

The excessive transport of monocytes into the arterial wall is one of the hallmarks of atherosclerosis. The transport of monocytes is modeled as a combination of advection-

diffusion and chemotaxis

$$\frac{\partial c_M}{\partial t} + u \cdot \nabla c_M = D_M \nabla^2 c_M - \nabla \cdot (c_M \chi \nabla c_{MCP1}) \ , \tag{2.7a}$$

$$- D_M \frac{\partial c_M}{\partial n} = \frac{m_r}{1 + \frac{WSS}{WSS_0}} c_{LDL,ox} c_M \ ; \text{Wall boundary condition,} \tag{2.7b}$$

where χ is the chemotactic sensitivity parameter, c_{MCP1} is the concentration of MCP-1, $c_{LDL,ox}$ is the concentration of oxidized-LDL molecules inside the arterial wall. Cilla et al. [117] showed that in long term, the concentration of oxidized-LDL molecules tends to be constant. m_r is a rate at which monocytes enter the arterial wall. A constant monocyte concentration $c_{M,0}$ is applied at the inlet. MCP-1 transport is modeled as

$$\frac{\partial c_{MCP1}}{\partial t} + u \cdot \nabla c_{MCP1} = D_{MCP1} \nabla^2 c_{MCP1} \ , \tag{2.8a}$$

$$- D_{MCP1} \frac{\partial c_{MCP1}}{\partial n} = -J_{0,MCP1} exp(K_{MCP1} TAWSS) \ ; \text{Wall boundary condition.} \tag{2.8b}$$

The constant coefficients in the WSS-dependent MCP-1 flux are calculated based on the in-vitro study performed by Yu et al. [118]. For the inlet boundary condition, a constant concentration, $c_{MCP1,0}$, is applied.

2.3 Results

2.3.1 WSS patterns

WSS streamlines can be used to visualize the near-wall velocity patterns. TAWSS vector direction and magnitude for different models are shown in Fig. 2.3. WSS LCS, TAWSS streamlines, and TAWSS fixed points are shown in Fig. 2.4. The location of soft and calcified

Table 2.3: List of biological parameters used in simulations.

Patameter	Value	Description	Reference
ATP transport			
D_{ATP}	$2.36 \times 10^{-6} [\frac{cm^2}{s}]$	ATP diffusion coefficient	[115, 114, 119]
K_m	$475 [\mu M]$	Michaelis constant	[115, 114, 119]
V_{max}	$0.8 \times 10^{-10} [\frac{mol}{cm^2 \cdot s}]$	maximum enzyme reaction velocity for ATP hydrolysis	[115, 114, 119]
S_{max}	$1 \times 10^{-13} [\frac{mol}{cm^2 \cdot s}]$	maximum ATP release rate	[115, 114, 119]
WSS_0	$0.1 [Pa]$	Reference WSS	[115]
$c_{ATP,0}$	$1 \times 10^{-10} [\frac{mol}{cm^3}]$	Inlet concentration of ATP	[115]
NO transport			
D_{NO}	$3.3 \times 10^{-5} [\frac{cm^2}{s}]$	NO diffusion coefficient	[38]
K_d	$693 \times 10^{-2} [\frac{1}{s}]$	NO degradation rate	[61]
R_{basal}	$2.13 \times 10^{-12} [\frac{mol}{cm^3}]$	Basal NO production rate	[38]
R_{max}	$457.5 \times 10^{-12} [\frac{mol}{cm^3}]$	Maximum NO production rate	[38]
d	$2 \times 10^{-4} [cm]$	EC thickness	[38]
WSS_0	$3.5 [Pa]$	Reference WSS	[38]
O_2 transport			
D_{O2}	$1.2 \times 10^{-5} [\frac{cm^2}{s}]$	Oxygen diffusion coefficient	[116]
$c_{O2,w}$	$1.044 \times 10^{-7} [\frac{mol}{cm^3}]$	Oxygen concentration at arterial wall	[116]
$c_{O2,0}$	$1.305 \times 10^{-7} [\frac{mol}{cm^3}]$	Oxygen concentration at the inlet	[116]
LDL transport			
D_{LDL}	$2.8 \times 10^{-7} [\frac{cm^2}{s}]$	LDL diffusion coefficient	[120]
l_{lj}	$2 \times 10^{-4} [cm]$	Length of a leaky junction	[46]
P_v	$1.92 \times 10^{-9} [\frac{cm}{s}]$	Permeability of vesicular pathway	[109]
Δp_{end}	$2400 [Pa]$	Pressure difference through the endothelium	[46]
μ_p	$1 \times 10^{-3} [Pa \cdot s]$	Plasma viscosity	[46]
a	$11 \times 10^{-7} [cm]$	Radius of LDL molecules	[109]
w	$20 \times 10^{-7} [cm]$	Half-width of leaky-junctions	[109]
R_{cell}	$15 \times 10^{-4} [cm]$	EC radius	[46]
unit area	$6.4 \times 10^{-1} [cm^2]$	-	[46]
a_1	$0.307 [cells]$	Constant in number of leaky cells formula	[33]
a_2	0.805	Constant in number of leaky cells formula	[33]
b_1	$0.003797 [cells]$	Constant in number of mitotic cells formula	[33]
b_2	14.75	Constant in number of mitotic cells formula	[33]
c_1	0.380	Constant in EC shape index formula	[33]
c_2	-0.79	Constant in EC shape index formula	[33]
c_3	0.225	Constant in EC shape index formula	[33]
c_4	-0.043	Constant in EC shape index formula	[33]
$c_{LDL,0}$	$3.12 \times 10^{-6} [\frac{mol}{cm^3}]$	Inlet concentration of LDL	[109]
Monocytes transport			
D_M	$1 \times 10^{-7} [\frac{cm^2}{s}]^*$	Monocyte diffusion coefficient	-
χ	$0.2 [\frac{cm^5}{g \cdot s}]$	Chemotactic sensitivity parameter	[46]
m_r	$6.37 \times 10^{-3} [\frac{cm^3}{mol \cdot s}]$	Rate at which monocytes enter the arterial wall	[46]
$c_{LDL,ox}$	$1 \times 10^{-7} [\frac{mol}{cm^3}]$	Concentration of oxidized LDL	[46]
WSS_0	$1 [Pa]$	Reference WSS	[46]
$c_{M,0}$	$5.5 \times 10^5 [\frac{cells}{cm^3}]$	Inlet concentration of monocytes	[46]
MCP-1 transport			
D_{MCP1}	$2 \times 10^{-4} [\frac{cm^2}{s}]$	MCP-1 diffusion coefficient	[50]
$c_{MCP1,0}$	$1 \times 10^{-9} [\frac{g}{cm^3}]$	MCP-1 inlet concentration	[50]
$J_{0,MCP1}$	$1.842 \times 10^{-18} [\frac{cm}{s}]$	A constant in MCP-1 flux equation	[118]
K_{MCP1}	$-1.391 [\frac{cm^2}{dyne}]$	Exponential constant in MCP-1 flux equation	[118]

* The physiological value for D_M is $1 \times 10^{-11} [\frac{cm^2}{s}]$ [46]. For the sake of numerical stability, a higher value is used in the simulations.

plaques are marked in Fig. 2.4. Comparing the diseased arteries (P1-P4) with healthy swine LAD arteries (P5 and P6) shows that the presence of plaque results in more complex WSS topological features. For instance, these topological features around the plaques in P1-LCx/LAD, P2-LAD, and P4-LCx models show multiple fixed-points and a complex WSS LCS pattern. In the healthy models, WSS fixed-points are located around the bifurcations, while the complex blood flow in diseased arteries leads to the emergence of additional fixed points and consequently complicated WSS LCS patterns.
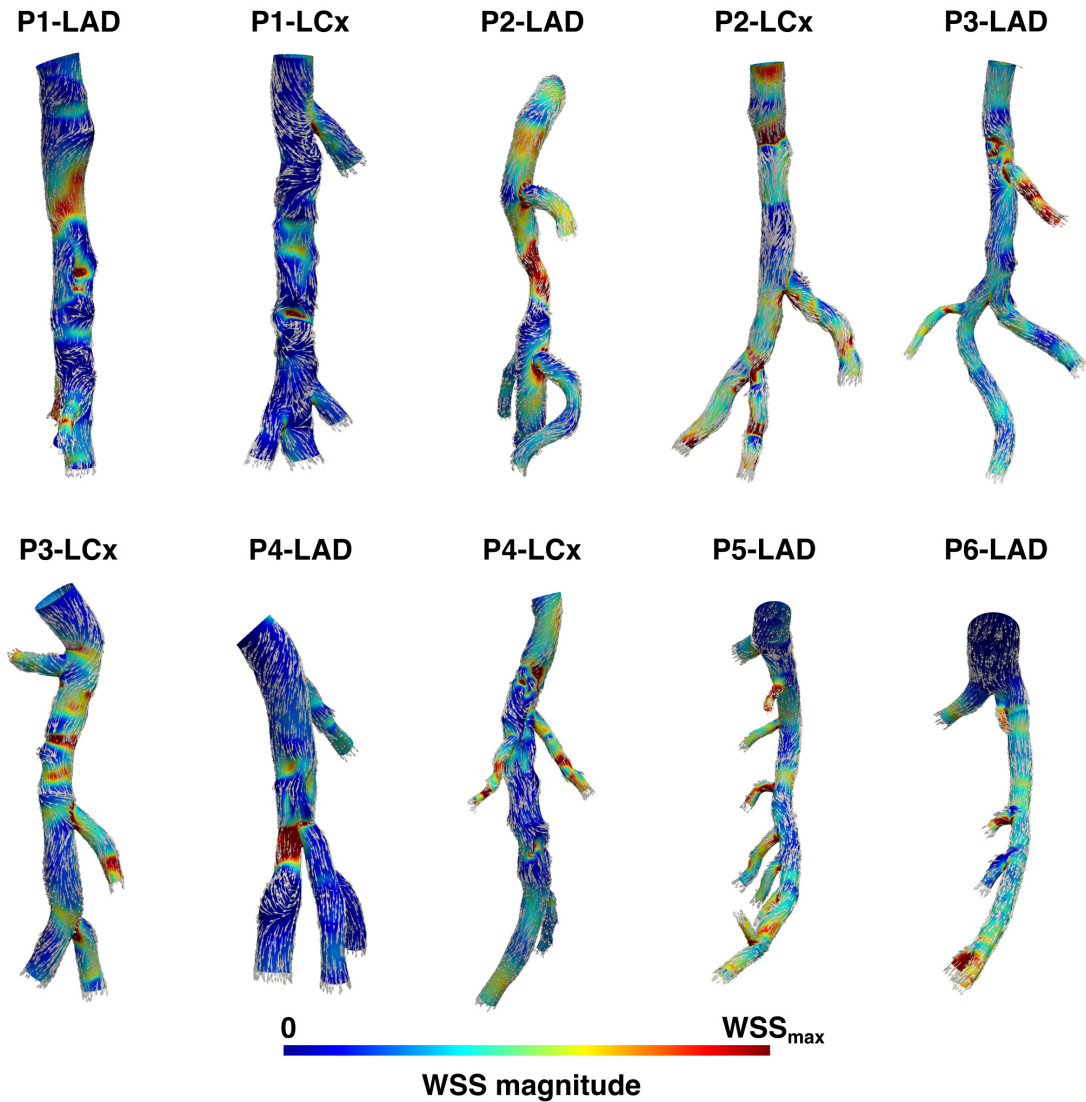
Figure 2.3: The distribution of WSS magnitude and direction for the 10 coronary artery models. The presence of atherosclerotic plaque results in complicated WSS patterns. WSS vectors are normalized for appropriate visualization of direction. The values of WSS_{max} for patients 1-4 (LAD/LCx) are 20/30, 90/70, 30/40, 20/25 $dyne/cm^2$, and models 5-6 (LAD) are 30 and 25 $dyne/cm^2$, respectively.

26
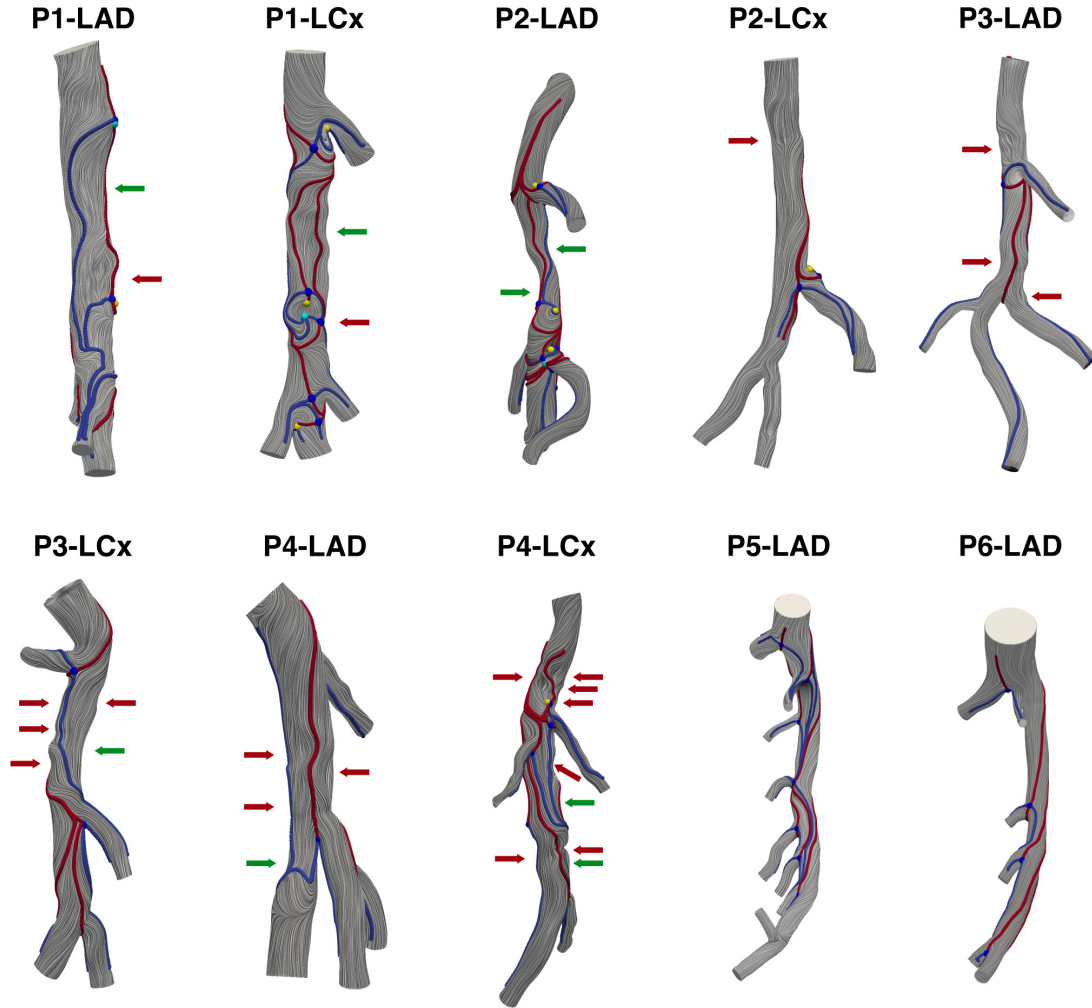
Figure 2.4: The distribution of WSS streamlines and WSS Lagrangian coherent structures (LCS). The attracting WSS LCS (blue lines) and repelling WSS LCS (red lines) are shown. The saddle-type fixed point (blue), stable fixed point (yellow), and unstable fixed point (cyan) are shown on top of the WSS streamlines. Green and red arrows point to the soft and calcified plaques, respectively.

2.3.2 Biochemical transport

The following figures show surface concentration or flux of the biochemicals and cells studied. The results are based on the region of interest for each model as shown in Fig. 2.1. The luminal surface concentration of LDL is shown in Fig. 2.5. Comparing the results with the prior WSS figures, it is observed that LDL concentration is high around the attracting WSS LCS, and in some cases inside the basin of attraction formed by the repelling WSS LCS. LDL concentration is higher at the vessel wall compared to the lumen, which is due

to the concentration polarization phenomenon, in which the LDL uptake by the wall is slow considering the size of LDL macromolecules, and therefore the LDL molecules accumulate on the arterial wall [121]. The LDL concentration patterns show spotty elevation in regions with low WSS magnitude. These spotty accumulations are related to regions where the ECs are more permeable due to leaky junctions. Elevated EC apparent permeability occurs in the distal region of the plaque where ECs have high leaky junction hydraulic conductivity ($L_{p,lj}$) values due to low WSS.
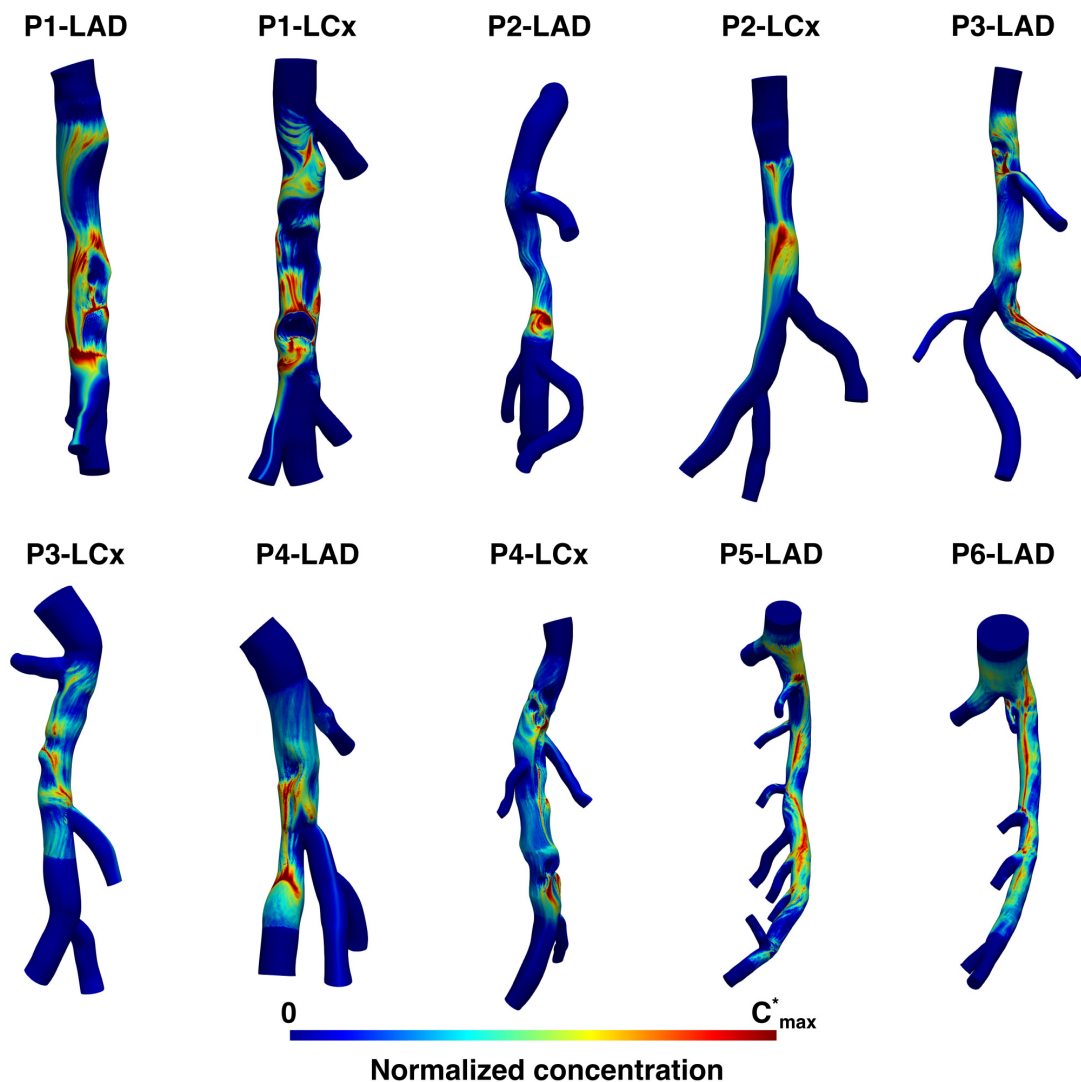
Figure 2.5: Distribution of LDL concentration for the 10 coronary artery models. The values of C^*_{max} on the color bar for patients 1-4 (LAD/LCx) are 0.400/0.367, 0.267/0.300, 0.400/0.433, 0.500/0.833, and models 5-6 (LAD) are 0.400 and 0.467, respectively. The normalized LDL concentration is defined as $C^* = (C_{LDL} - C_{LDL,0})/(C_{max} - C_{LDL,0})$ where $C_{max} = 3.1203 \times 10^{-6}$ mol/cm^3.

The surface concentration of NO is shown in Fig. 2.6. It can be seen that the surface concentration of NO around the attracting WSS LCS is locally high. The repelling WSS LCS forms a basin of attraction and pushes the surface concentration towards the attracting one. According to Fig. 2.6, the surface concentration of NO is high right after and around the atherosclerotic plaques where an attracting WSS LCS is present. Another atheroprotective biochemical studied here is ATP. Figure 2.7 shows the ATP surface concentration for all models. The elevated values of ATP concentration can be seen around the attracting WSS LCS. Although higher NO and ATP are produced in regions of high WSS magnitude, the present transport results show that the concentration of NO and ATP in these regions will be washed away by the near-wall velocity after a few cardiac cycles and ultimately the WSS LCS dictate the surface concentration pattern where elevated concentrations happen around the attracting WSS LCS. That is, high WSS magnitudes increase the overall ATP and NO concentration levels, however locally elevated NO and ATP concentrations do not match high WSS regions.

The story for oxygen transport is different from the other biochemicals. The wall boundary condition for oxygen transport is constant concentration. Specification of a constant concentration conforms with the assumption that the excessive oxygen is consumed and the wall acts as a sink [43]. The oxygen flux on the arterial wall is shown in Fig. 2.8. The flux is higher in regions having higher WSS magnitude. An interesting take out from these results is that the flux of oxygen around the attracting WSS LCS has the lowest value.

The transport of MCP-1 highly depends on the directionality of WSS vectors as well as the WSS LCS. As can be seen in Fig. 2.9, the flow separation region downstream of the stenosis and bifurcations (healthy models) can be visualized from the backward WSS vectors where elevated MCP-1 concentration occurs. Finally, the luminal surface flux patterns for monocyte transport (Fig. 2.10) show a higher uptake of monocyte cells in regions with elevated values of MCP-1 concentration. Overall, elevated monocyte flux occurs in regions with high MCP-1

29
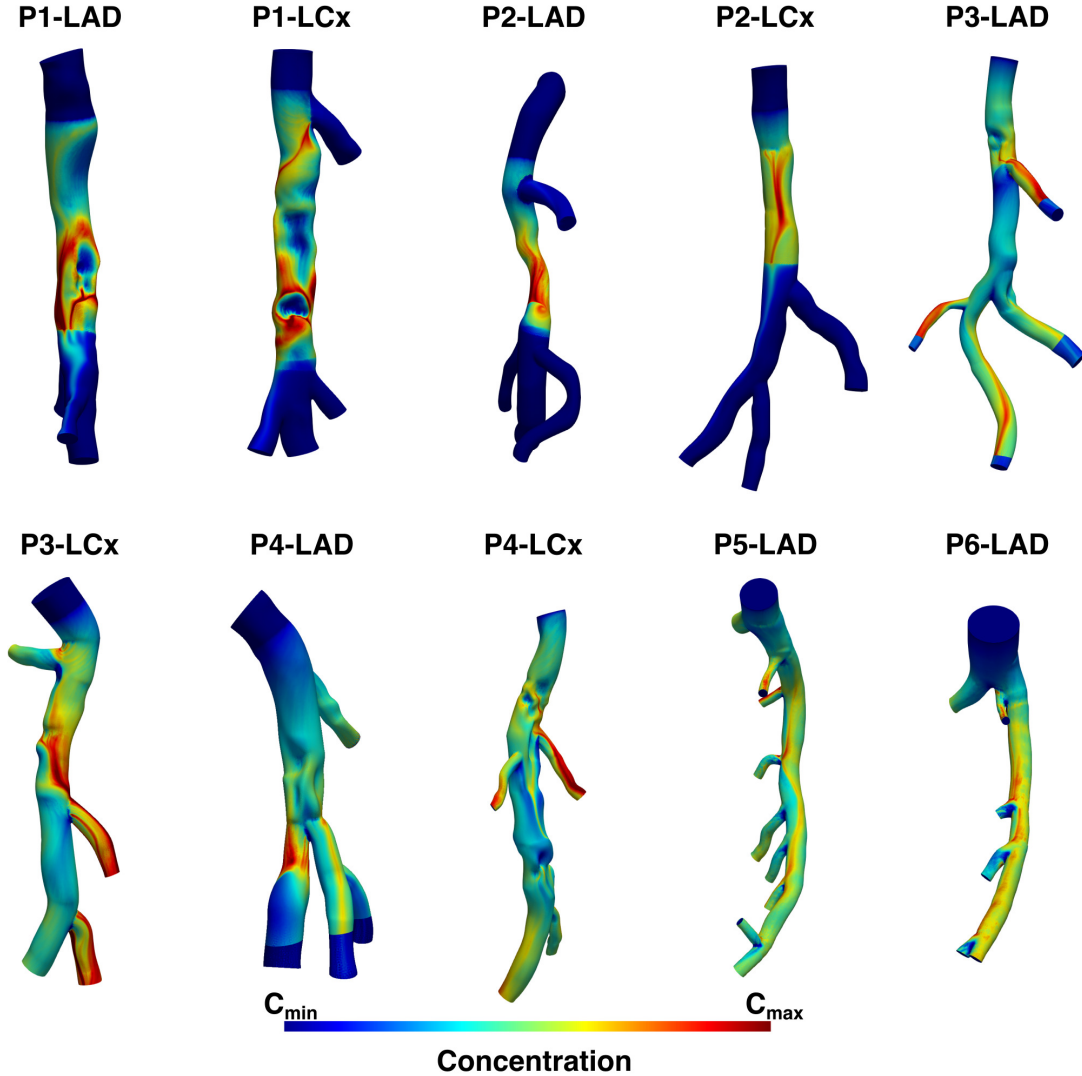
Figure 2.6: Distribution of NO concentration for the 10 coronary artery models. The values of C_{max} on the color bar for patients 1-4 (LAD/LCx) are $21 \times 10^{-12}/33 \times 10^{-12}$, $10 \times 10^{-12}/10 \times 10^{-12}$, $10 \times 10^{-12}/9 \times 10^{-12}$, $8 \times 10^{-12}/9 \times 10^{-12}$ mol/cm^3, and models 5-6 are 12×10^{-12} and 12×10^{-12} mol/cm^3, respectively. $C_{min} = 0$ mol/cm^3.

concentration, which attracts monocytes and regions with low WSS magnitude where higher cell adhesion occurs.

To quantify the effect of the plaques on the overall surface concentration/flux results, Fig. 2.11 shows the ratio of surface-averaged concentration/flux in the healthy part of the artery (proximal to the stenosis) to the stenosis region in the human coronary artery models. Our results show that the average concentration of NO, ATP, LDL, and MCP-1 in the stenosis part of the arteries is mostly higher than the average concentration in the healthy, proximal part of
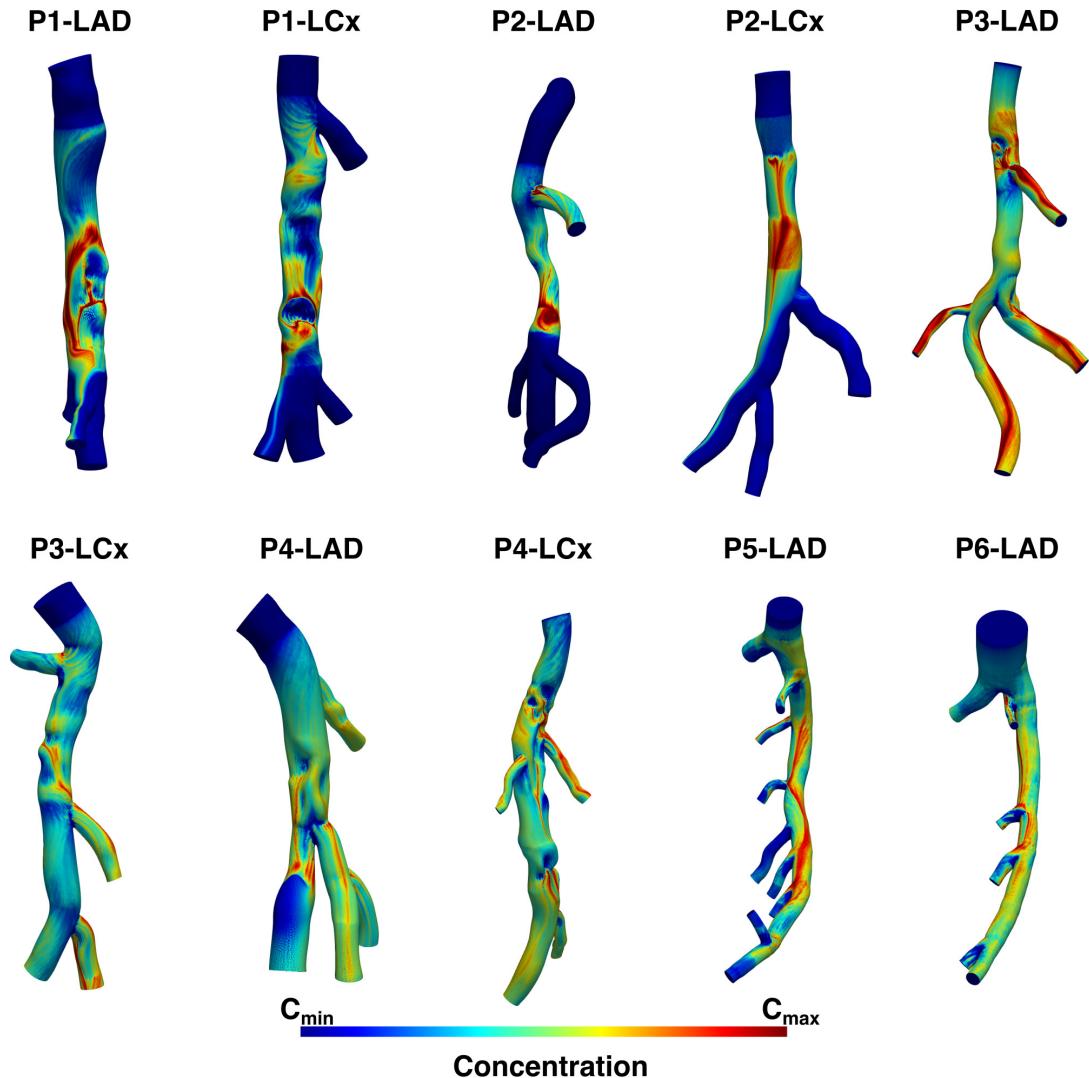
Figure 2.7: Distribution of ATP concentration for the 10 coronary artery models. The value of C_{max} on the color bar is $2 \times 10^{-9} mol/cm^3$ and C_{min} is the inlet concentration $c_{ATP,0}$.

the arteries. In contrast, oxygen flux is lower in the stenosis region and the monocyte results show high variability among patients.

2.4   Discussion

In this paper, the near-wall transport of some of the prominent biochemicals/cell in atherosclerosis were studied in 10 coronary artery models (LAD and LCx). Eight models showed
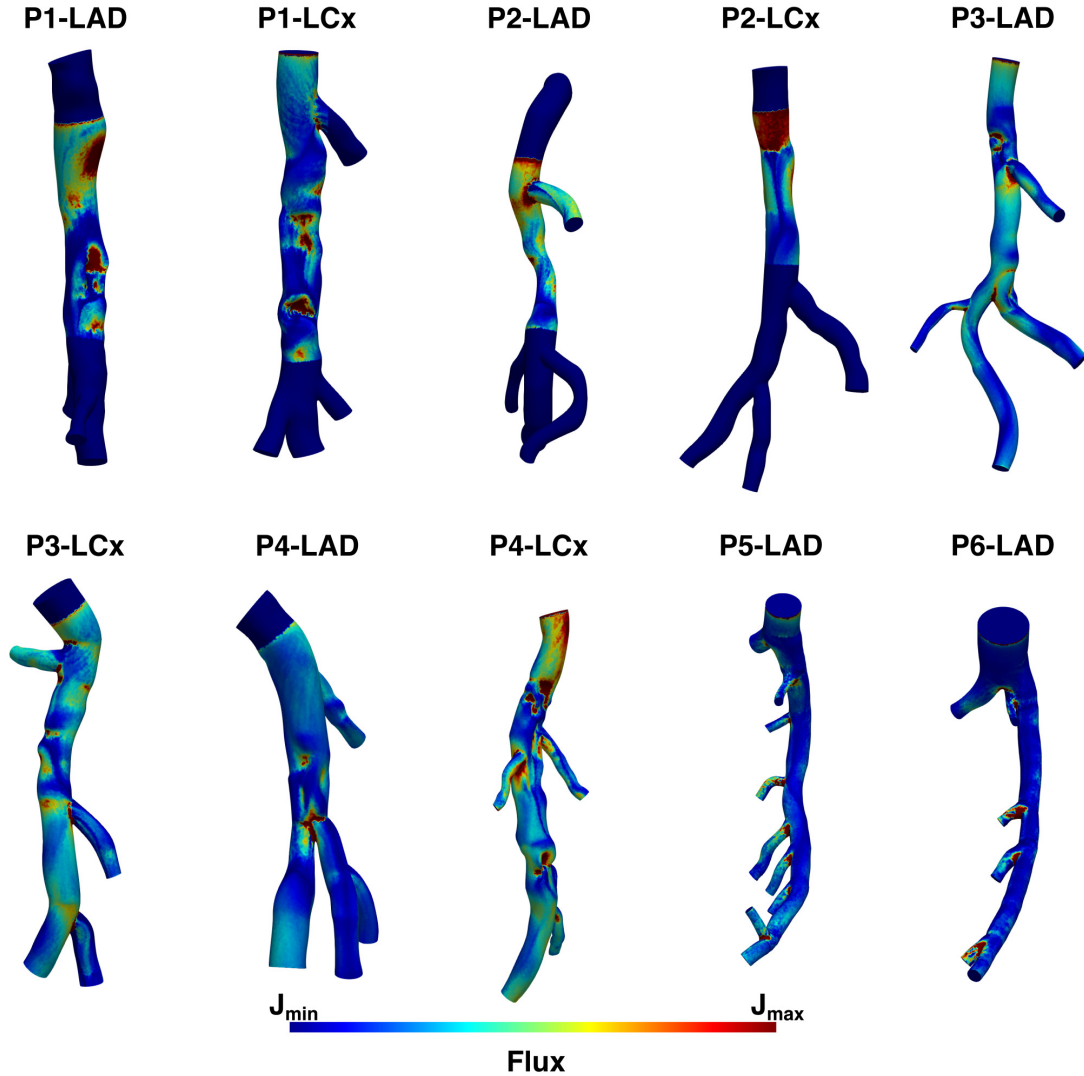
Figure 2.8: Distribution of oxygen flux for the 10 coronary artery models. The value of J_{max} on the color bar is $2.1 \times 10^{-12} mol/cm^3 \cdot s$ and $J_{min} = 0\ mol/cm^3 \cdot s$.

multiple atherosclerotic plaques with complex morphologies, leading to complex near-wall flow patterns. Our results showed that the luminal surface concentration and flux patterns of these biochemicals could be explained using WSS vectors. Different studies have looked into each of these biochemical and cell transport processes in different arterial complications. However, a unified investigation of these transport processes in patient-specific atherosclerotic coronary arteries has not been carried out. Particularly, using high-resolution computational models, this work tries to fill the knowledge gap in the field of coronary artery atherosclerosis related to transport and provide a mechanistic explanation for these transport
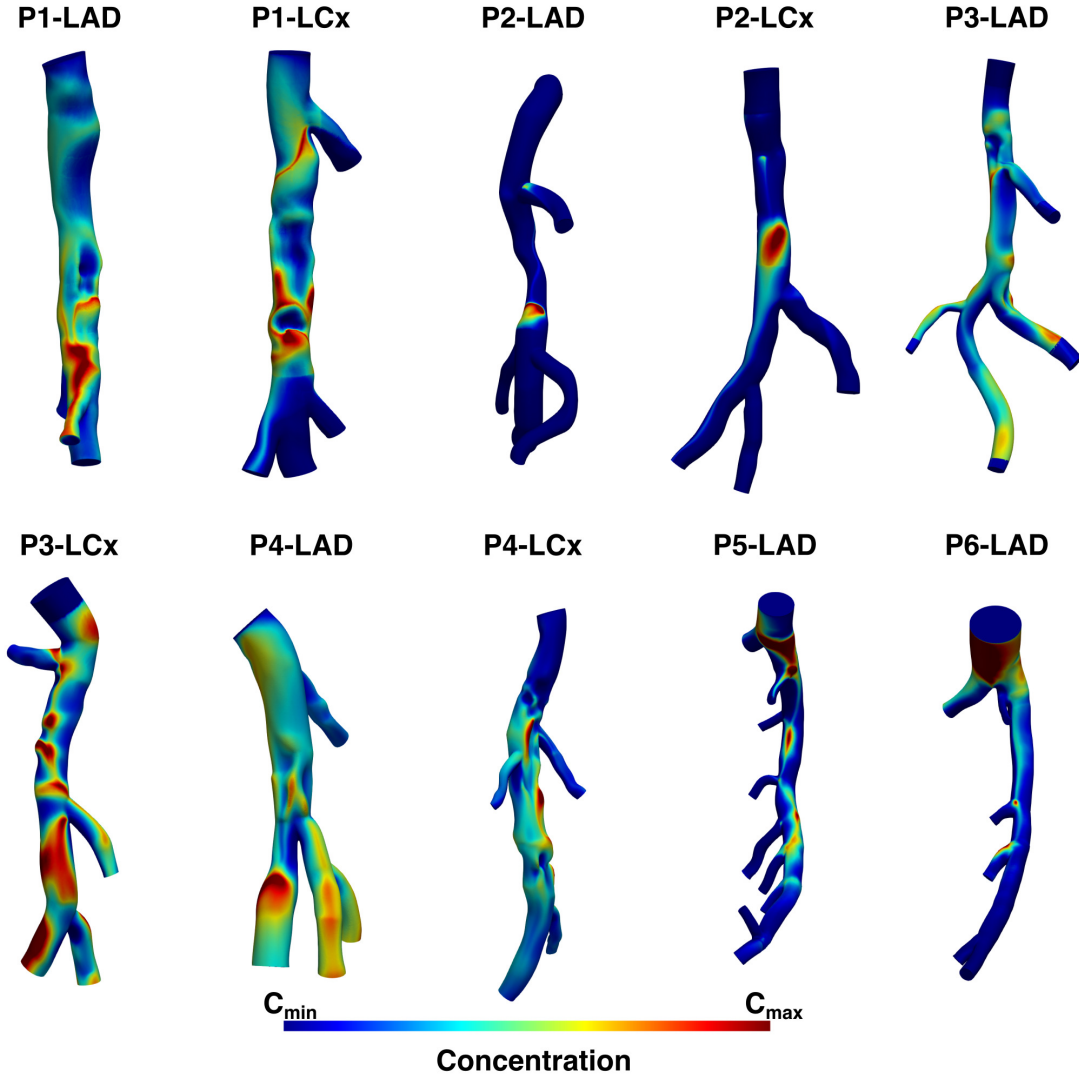
Figure 2.9: Distribution of MCP-1 concentration for the 10 coronary artery models. The value of C_{max} on the color bar is $5.498 \times 10^5 cells/cm^3$ and C_{min} is the inlet concentration $c_{MCP1,0}$.

processes.

Our results show that the presence of atherosclerotic plaques result in a complicated near-wall blood flow pattern and accordingly complex WSS LCS patterns with multiple WSS fixed points. The main difference between diseased (P1-P4) and healthy (P5 and P6) models was the distribution of WSS LCS. In healthy models, the saddle type fixed points were observed to be located at the bifurcations and the resulting attracting and repelling WSS LCS were aligned with the bulk flow. The presence of atherosclerotic plaques resulted in multidirec-
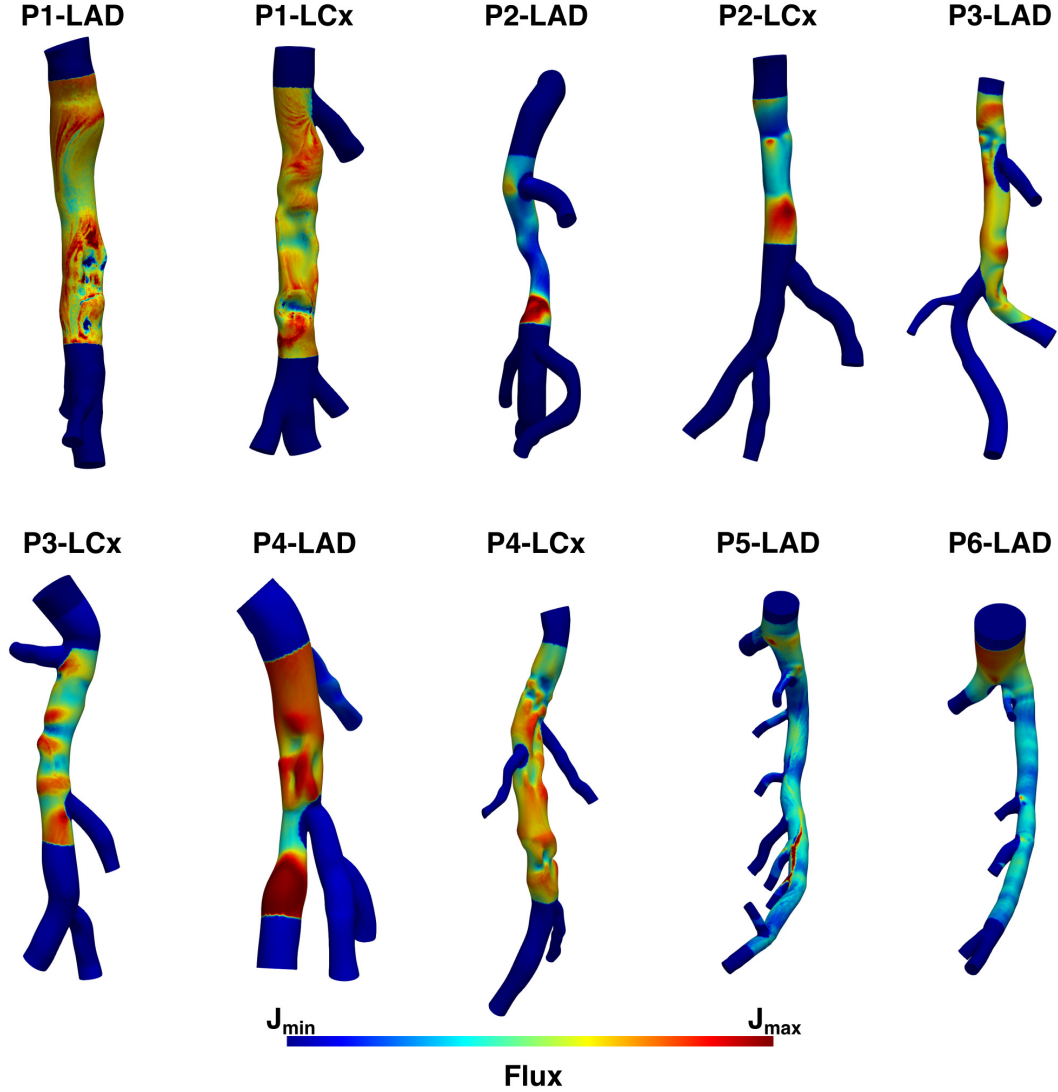
Figure 2.10: Distribution of monocyte flux for the 10 coronary artery models. The value of J_{max} on the color bar is $4 \times 10^{-4} cells/cm^3 \cdot s$ and J_{min} is $1 \times 10^{-4} cells/cm^3 \cdot s$.

tional WSS patterns with manifolds in the transverse direction. In the distal vicinity of most plaques, repelling WSS LCS was formed, which pushed biochemical concentrations towards the attracting WSS LCS.

It has been shown in the literature that low and oscillatory WSS [122] and more recently transverse WSS [95] correlate with atherosclerosis growth. Shear stress mediated endothelial cell behavior is the major motivation behind these studies. Herein, we have shown that WSS patterns also control all of the atherogenic and atheroprotective biotransport processes in
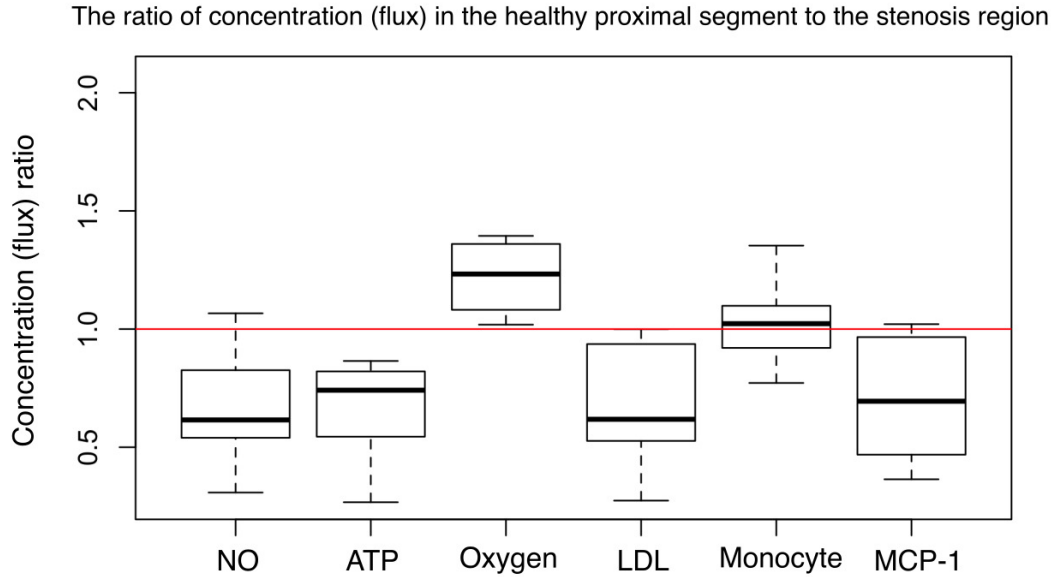
Figure 2.11: Box plots showing ratios of surface-averaged concentration/flux at the proximal, healthy artery segment to the stenosis part of the artery. The data is based on the 8 human models. The median, first, and third quartiles are shown. The whiskers correspond to the minimum and 99th percentile of the data.

atherosclerosis. Therefore, our study further substantiates the utility of WSS as a comprehensive parameter in studying atherosclerotic disease. In particular, we have shown that the combination of WSS topology (WSS directionality and manifolds) as well as WSS magnitude can completely explain the biochemical and cell localization patterns in coronary artery atherosclerosis.

Our results and prior work in the literature on WSS mediated endothelial cell mechanotransduction motivate a comprehensive theory for WSS in atherosclerosis. Despite some conflicting results in the literature [123], we propose that once WSS is mechanistically interpreted in the context of mechanotransduction together with blood flow mediated near-wall transport, we can provide a complete picture for its role in atherosclerosis. Towards this goal, Fig. 2.12 summarizes our findings in a single graph. As shown in the graph, low WSS promotes and high WSS prevents atherosclerosis via mechanotransduction pathways. Similar conclusions are made for WSS magnitude mediated biotransport processes in atherosclerosis. On the other hand, the attracting and converging WSS vector patterns show inconsistent results. These patterns promote near-wall accumulation of NO and ATP, which protect

against atherosclerosis, however, this type of directional WSS pattern also increases near-wall LDL and MCP-1 concentration, promotes monocyte flux into the wall, and reduces oxygen flux, all of which promote atherosclerosis. We can conclude that low WSS promotes atherosclerosis, high WSS prevents atherosclerosis, and attracting/converging WSS leads to conflicting results and likely competition between different pathways.
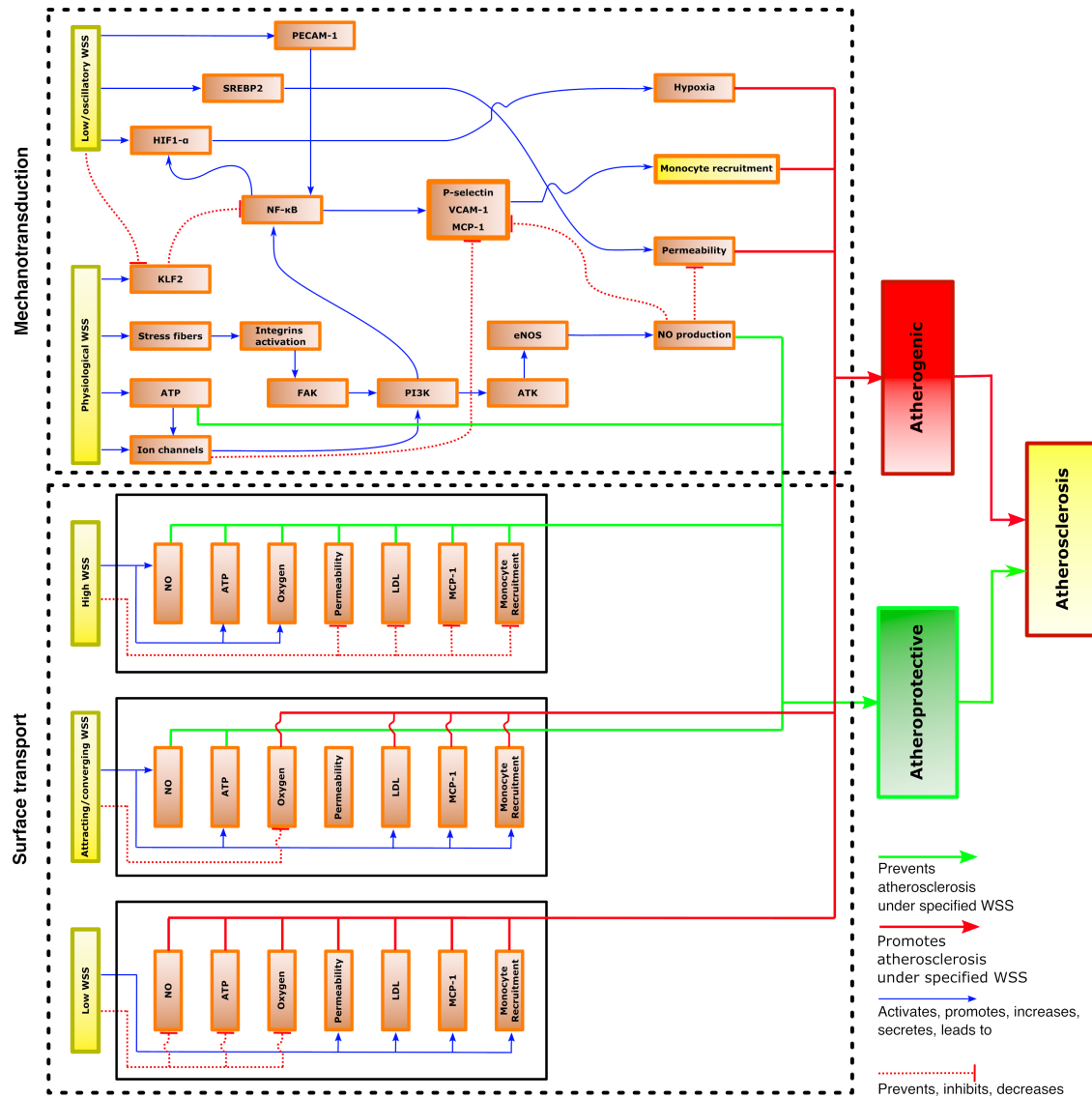
Figure 2.12: A summary of the role of WSS in atherosclerosis. The schematic diagram shows endothelial mechanotransduction and signaling induced by shear stress as well as WSS-dependent near-wall surface concentration of various biochemicals. ATP adenosine triphosphate; LDL low-density lipoprotein; NO nitric oxide; MCP-1 monocyte chemoattractant protein-1; KLF2 Krüppel-like factor 2; FAK focal adhesion kinase; PI3K phosphatidylinositol-3-kinase; AKT protein kinase B; eNOS endothelial nitric oxide synthase; NF-κB Nuclear factor kappa B; VCAM-1 vascular cell adhesion molecule; PECAM-1 platelet endothelial cell adhesion molecule-1; SREBP2 sterol regulatory element-binding proteins2; HIF1-α Hypoxia-inducible factor-1α.

The transport results could be explained in the context of WSS magnitude and vectorial

features. Low WSS increases permeability to LDL and therefore leads to higher LDL concentration values. At the same time, LDL concentration hotspots localize near the attracting WSS LCS and match with the attracting WSS LCS pattern. NO and ATP both possess similar transport mechanisms where they are produced via WSS-dependent flux by the endothelial cells. The qualitative NO and ATP patterns were similar where both were attracted by the attracting WSS LCS and localized around these manifolds. Interestingly, while high WSS magnitude increases the amount of NO and ATP production and therefore ultimately contributes to higher concentration values, locally, it does not correlate with high NO and ATP surface concentration. That is, the locally elevated NO and ATP concentration values typically do not coincide with elevated WSS values. Oxygen flux is increased in regions of high WSS and is reduced around the attracting WSS LCS. As the effective oxygen transport is from the lumen into the wall, it tends to localize with regions where the near-wall normal velocity is towards the wall (e.g., impingement), which typically have higher WSS values surrounding them. On the other hand, near the attracting WSS LCS, the near-wall normal flow is away from the wall, which resists oxygen transport into the wall. It should be noted that even though one might think of LDL as having a similar transport mechanism, mathematically, LDL has an inward (towards the lumen) flux boundary condition at the wall due to the concentration polarization effect [121] and therefore its transport pattern is different from oxygen. MCP-1 has higher inward flux in low WSS regions, and it localizes around regions of low WSS and attracting WSS LCS. Finally, monocyte patterns were similar to MCP-1 and higher monocyte recruitment tends to happen in regions of low WSS magnitude.

In this study, we observed another WSS singular point beyond what was previously introduced [105]. This type of fixed point is seen in Fig. 2.13 where saddle and node fixed points coincide and the dynamical system undergoes a saddle-node bifurcation. An example in P2-LCx is shown in Fig. 2.13. As can be seen in the figure, the WSS vectors uniformly approach the atherosclerotic plaque where a saddle-node fixed point is present and then the vectors are converged to an attractor downstream of the fixed point. This non-hyperbolic behavior can

be observed in P2-LCx, P4-LAD, and P4-LCx models, and similar to the attracting WSS LCS they attract biochemicals and cells except oxygen. These attracting vectors explain the locally elevated concentration patterns that do not match with the attracting WSS LCS.
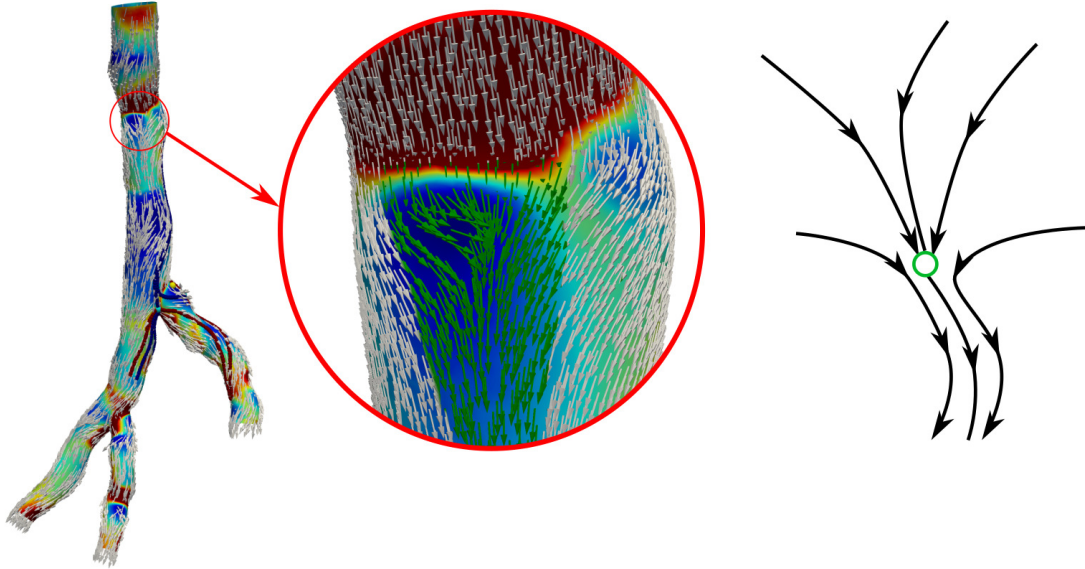
Figure 2.13: Saddle-node bifurcation structure. The WSS vectors show an almost uniform structure upstream of the saddle-node bifurcation and then because of the presence of saddle-node fixed points the WSS vectors converge towards the manifold downstream. This results in attracting WSS vectors (shown in green) that attract biochemicals and lead to high concentration similar to attracting WSS LCS.

Our results show that in general plaques create backward and attracting WSS patterns downstream of the plaque, which tend to attract atherogenic biochemicals like LDL. While this is in line with previous clinical data where preferential plaque growth usually occurred downstream of a plaque [124, 125], it is important to note that atheroprotective biochemicals such as NO and ATP also localize in similar regions. It is not clear how the combination of these competing effects play out in the process of atherosclerosis. We should note that here we discuss NO localization on the lumen side where it can reduce endothelial cell permeability and prevent platelet adhesion [111]. NO concentration in the vessel wall also plays an important atheroprotective role by regulating smooth muscle cell behavior. In regions with low WSS, a lower amount of NO is produced, and therefore lower NO concentration exists inside the vessel wall.

The summary of our findings and prior research on mechanotransduction in Fig. 2.12 highlights the importance of low WSS in promoting atherosclerosis via multiple pathways. The increase in expression of CAMs regulated by PECAM-1 due to low WSS results in a reduction in the production of NO, increases the EC permeability, and recruits more monocytes to the site. At the same time, inflammation triggered by low WSS results in MCP-1 production, which enhances monocyte recruitment. Low WSS leads to activation of HIF1-α, which results in hypoxia. Interestingly, from a transport point of view, regions of low WSS also accompany lower oxygen flux, which again promotes hypoxia. Low shear stress prevents NO production and downregulates the proatherogenic gene SREBP2, which both result in an increase in EC permeability in regions with low WSS, and therefore a higher uptake of atherogenic macromolecules like LDL. On the other hand, high (physiologic) WSS protects against atherosclerosis progression. Physiological WSS can be transmitted to stress fibers, leading to integrin activation and phosphorylation of FAK, which results in the activation of PI3K/ATK, regulating the expression of eNOS and finally production of NO. Production of NO downregulates the translocation of CAMs and prevents monocyte recruitment into the site. Platelet recruitment is another proatherogenic pathway, which is inhibited by NO [111]. Finally, high WSS promotes KLF2 expression, which inhibits the transcription factor NF-κB and ultimately prevents monocyte recruitment. From a transport point of view, high WSS increases the production of NO and ATP, leads to a localized elevation in oxygen flux, and reduces near-wall localization of atherogenic factors like LDL and monocytes. It should be pointed out that while high WSS prevents atherosclerosis growth, at the same time it can promote plaque vulnerability and rupture for established plaques [126].

There are some potential limitations that could affect the results of this study. One of these limitations is the application of initial and boundary conditions for the numerical simulations. The choice of inflow boundary conditions was based on the general coronary artery waveforms with parabolic profiles. In reality, the blood flow waveform is patient-specific and might vary between patients. Also, the initial condition for biochemical/cell transport in coronary

39

arteries could affect the accuracy of the computational simulations. De Nisco *et al.* [107] showed how initial conditions can affect the accuracy of computational mass transport models in the aorta. They concluded that using a 3D phase-planar flow map as inflow velocity condition will mostly eliminate the sensitivity of LDL blood-to-wall transfer to the LDL initial condition. Due to the lack of this data for our patients, general coronary artery waveforms with parabolic spatial distribution was the closest choice to the patient-specific 3D phase-planar flow map. Although a large number of cardiac cycles were used to obtain a quasi-steady state biochemical transport pattern and reduce the sensitivity to the applied zero initial condition, this might not fully eliminate this limitation. The other limitation is related to the choice of rigid wall for coronary arteries. It is well known that the presence of calcified plaques significantly increases the arterial wall stiffness. Additionally, it has been recently shown that the effect of coronary wall elasticity on TAWSS results is negligible [103]. Another limitation is related to the blood-to-wall transport of oxygen in coronary arteries. The utilized governing equation in the present study does not take into account hemoglobin's oxygen-binding capacity. Previous studies showed that hemoglobin acts to merely augment oxygen transport patterns by a spatially constant factor of approximately two [116]. Thus, it does not affect the qualitative distribution of oxygen flux on the arterial wall.

In conclusion, we have studied the near-wall transport of major biochemicals and cells contributing to the initiation and progression of atherosclerosis. The results of this manuscript showed that near-wall localization patterns are dictated by WSS magnitude and vectorial features (WSS LCS). Our results were summarized with prior mechanotransduction studies and we presented a comprehensive theory for the role of WSS in atherosclerosis (Fig. 2.12).

Chapter 3

The longitudinal study of relation between hemodynamics and vulnerable coronary atherosclerotic plaques

3.1 Introduction

Coronary artery disease remains a major cause of death in the US and worldwide. According to the recent AHA update, cardiovascular disease is responsible for one of every three deaths in the US [1]. The pathological studies have suggested that specific atherosclerotic plaques, which do not create a considerable stenosis, show shared features related to acute coronary syndrome (ASC). This type of plaques are called vulnerable plaques. Recently, an effort has been organized to use coronary computed tomography angiography (CCTA) in high risk patients to investigate the presence of vulnerable plaques. The advantage of CCTA is the

possibility of visualizing the volumetric features of coronary artery plaques rather than just focusing on the narrowing of the lumen [127, 128, 129].

Atherosclerosis is a condition in which deposits of fatty material, called plaque, build up inside arterial walls reducing or completely blocking blood flow. Complex interactions between certain cells, biomechanical forces, and biochemical transport influence the progression of atherosclerosis [130]. To date, angiographic categorical definitions based on luminal stenosis have been applied for diagnosing coronary artery disease (CAD) and determining a suitable management strategy [131, 132, 133]. Recent studies show simple luminal assessment of CAD does not provide a complete picture [134]. There are asymptomatic patients with non-obstructive, eccentric coronary plaque that may face an ACS with devastating effects if the clinicians fail the early identification of high risk coronary artery lesions [4, 5, 135, 6]. Thus, the traditional idea of using the degree of luminal stenosis as the sole imaging marker for selection of the best therapeutic approach is challenged by the evidence showing that coronary plaque composition plays a role. This paradigm shift represents an important element for research in primary prevention of ischemia and ischemic stroke and in secondary myocardial infarction (MI) and stroke prevention, because of the potential implications for management. Histologically, plaques associated with ACS demonstrate a necrotic core similar to a ruptured plaque covered by a thin fibrous cap [136]. CCTA-based features and plaque composition associated with high risk for ACS include a large plaque burden (PB), plaque volume (PV), volume of necrotic core (VNC), volume of calcium plaque (VCP), volume of low attenuation plaque (VLAP), perivascular fat index (PFI), stenosis percentage (SP), presence of napkin-ring sign (NRS) and spotty calcification [137]. While there have been studies correlating the hemodynamics to plaque growth [138, 139, 140, 141], the relation to plaque vulnerability features has been mostly overlooked.

Qualitative assessment of atherosclerotic plaques has been used to find the stenosis and estimate the composition of the plaque. The qualitative features in CCTA images that have

been used to identify a vulnerable plaque include presence of low attenuation plaque (LAP), positive remodeling (PR), spotty calcification, severe stenosis, and napkin-ring sign (NRS). According to the literature, the LAP is defined as a region of vessel with Hounsfield unit values < 50 [142] and PR is defined as the ratio of diameter of artery to the diameter of proximal normal section which is ≥ 1.1 [143]. The NPR is defined as a circular CCTA attenuation pattern demonstrating a central area of low attenuation in contact with the lumen and is surrounded by a ring of higher attenuation pixels [144]. A spotty calcification is a small, dense calcified plaque surrounded by non-calcified plaque [136].

The majority of plaque quantification methods in the literature use fixed thresholds on HU images to quantify the composition of atherosclerotic plaques. It has been shown that the pixel intensity of lumen, calcified plaque, and organ over-projection can significantly affect the accuracy of this method [145, 146, 147, 148]. To resolve the problem, a novel method has been introduced which uses adaptive HU thresholds based on the local contrast of the lumen, presence of large, dense calcified plaque, and presence of severe stenosis [148, 149]. However, the effect of organ over-projection has not been investigated.

In this chapter, the association of hemodynamics and biotransport with longitudinal changes in qualitative and quantitative characteristics of vulnerable atherosclerotic plaques is studied. An in-house software is developed for the coronary artery segmentation in both CCTA images as well as the reconstructed 3D coronary artery models, and semi-automatic assessment of qualitative and quantitative features of arterial segments. The developed software uses vesselness enhancement filter to reduce the organ over-projection effect, active contour segmentation and vessel wall membership function to reduce the unwanted areas around the vessel wall, and adaptive threshold method to accurately quantify the vulnerable plaque characteristics. The present chapter is organized as follows: First, the software development process and algorithms used for segmentation and quantification of arterial cross-sections are presented. Then, the results of quantification for both baseline and follow-up are compared

against the hemodynamics and biotransport results to study the correlation between the hemodynamic parameters and the longitudinal changes in the plaque characteristics. At the end, a detailed assessment of the results is provided and limitations of current study are discussed.

3.2 Methods

In this section, the process of developing a semi-automatic plaque quantification software is discussed in detail. Two sets of coronary computed tomography angiography (CCTA) images from human subjects were collected. Contrast scans for the evaluation of coronary artery plaque volume at baseline and 12 months were acquired. The CCTA images belongs to a single-center, randomized, placebo-controlled, double-blind trial conducted at the Lundquist Institute for Biomedical Innovation at Harbor UCLA Medical Center (Clinicaltrials.gov: NCT03931434).

3.2.1 Semi-automatic plaque quantification software

The developed semi-automatic plaque quantification software was developed in Matlab App Designer (R2019a Update 9). The developed software contains three main sections: arterial centerline and image slicing, semi-automatic segmentation of arterial wall, and plaque quantification. Each of these sections are designed in different windows so that the user can share the necessary data between them. In the next subsections, the algorithms used in each section are presented in details.

3.2.2 Centerline and slicing

This section of the software deals with importing, categorizing, sorting, and visualization of a metadata with Digital Imaging and Communications in Medicine (DICOM) format. The centerline and slicing window contains six different panels: Import DICOM metadata, Image navigator, Extract luminal cross-section images, WL/WW brightness and contrast settings, visualization panel, and Centerline/ slicing settings. Figure 3.1 shows the centerline and slicing screen.
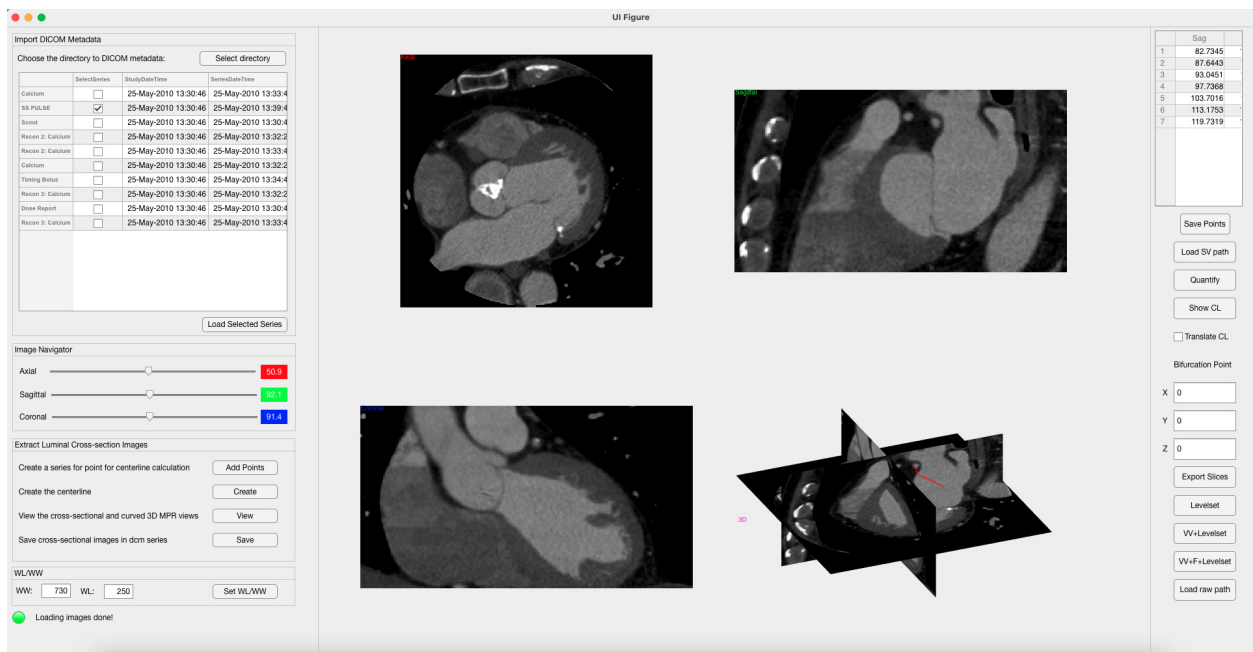
Figure 3.1: Centerline and slicing screen. The screen shows the metadata information about one of the patients as well as axial, coronal, and sagittal views of the CCTA.

<u>Import DICOM metadata</u>. The user can interactively select the directory in which the DICOM metadata is stored. The software will categorize the metadata based on the label of each dataset in the metadata, sort each dataset based on the image ID, and shows an overview of the most important information for each dataset in a table. This information includes: study date/time, series date/time, patient sex, modality, frames, study description, and study instance UID. Based on the information provided, user can choose to visualize the desired dataset by choosing the dataset from the table and pushing the Load Selected

Series.

Image navigator. This panel allows the user to scroll through the axial, sagittal, and coronal slices of the image series. Also, the user is given the ability to use a crosshair on each slice to scroll through the images by focusing on a single slice. For example, when the user moves the crosshair on the axial slice, the coronal and sagittal views will be automatically changed to conform to the selected point in the 3D DICOM images.

Extract luminal cross-section images. This panel provides actions regarding the interactive centerline generation. User can select centerline points on the visualization panel and then by pressing the *Add Points* button, the selected point will be stored in the memory. by selecting multiple points along the center of the lumen and adding the points to the centerline, the user can press *Create* button in this panel to generate the centerline along the selected points using a cubic interpolation method. The *View* button can be used to see the generated cross-sectional view of the each point on the centerline and the *Save* button will store the centerline into the disk in in a format that *Simvascular* software can read.

WL/WW brightness and contrast settings. Since different DICOM datasets have different levels of contrast and brightness, this panel allows the user to set the window level (WL) and window width (WW) for the visualization of the DICOM metadata. WW is the range of HU displayed and WL is the HU in the center of the window width.

Centerline/ slicing settings. This panel contains the settings related to handling the arterial centerline and generating the luminal cross-section segments along the centerline. The software provides two different options to the user to create the arterial centerline: interactively create the centerline by selecting points on the visualization views or import a centerline previously generated in the *Simvascular* software.

To create a centerline interactively, the user need to use the *Extract luminal cross-section images* panel to add points to the centerline. The axial, sagittal, and coronal index of

selected points will be shown in a table inside this panel. One can store these points using *save points* button. When the centerline is created, the user can generate the cross-sectional slices along the centerline and transfer them to the plaque quantification section by pressing *Quantify* button. Also, the user can visualize the centerline by pressing the *Show CL* button and store the cross-sectional slices into the disk in DICOM format by pressing *Export Slices*.

To create the cross-sectional segment of the artery, the software allows the user to choose from four options. The first approach creates the cross-sectional slices at each centerline point with no slice size limit. In other words, the generated segment is a slice of the 3D image with a center equal to the centerline point and a normal vector equal to the tangential vector to the centerline at the specified point. The second approach is a close-up view of the arterial cross-section which is extracted using a levelset method. First, a Sigmoid function is applied to the slice

$$S_I = \frac{1}{1 + e^{-a(I-c)}} \; , \tag{3.1}$$

where I is the image intensity in HU, $a = 0.1$ is the steepness of the S-shape curve, and $c = 50$ is the cut-off value. The sigmoid function de-noises the original image and generates an image with intensities ranging from 0 to 1. Fig. 3.2 shows the original image and the image after applying the Sigmoid function. The Sigmoid image then is fed into a levelset algorithm to find the edges of the arterial cross-section. The levelset algorithm uses region-based active contour segmentation proposed by Chan [150]. Unlike the classical active contour models, the algorithm detects objects whose boundaries are not necessarily defined by gradient but it minimizes an energy function. This is of importance when dealing with segmentation of diseased arterial cross-sections with different intensity values on the edges of the vessel wall. Fig. 3.3 shows input image, the initial seed for segmentation, the levelset boundary, and the final segmented image.

47

Original image · Image with Sigmoid filter
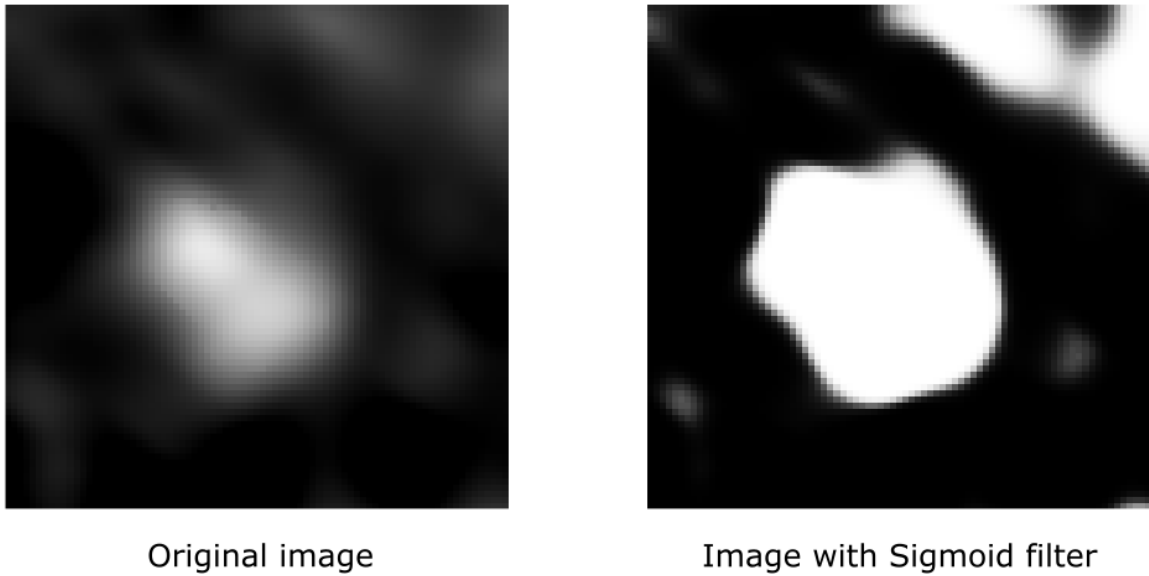
Figure 3.2: The result of applying the Sigmoid function on an arbitrary arterial cross-section.

Original image · Levelset process · Segmented image
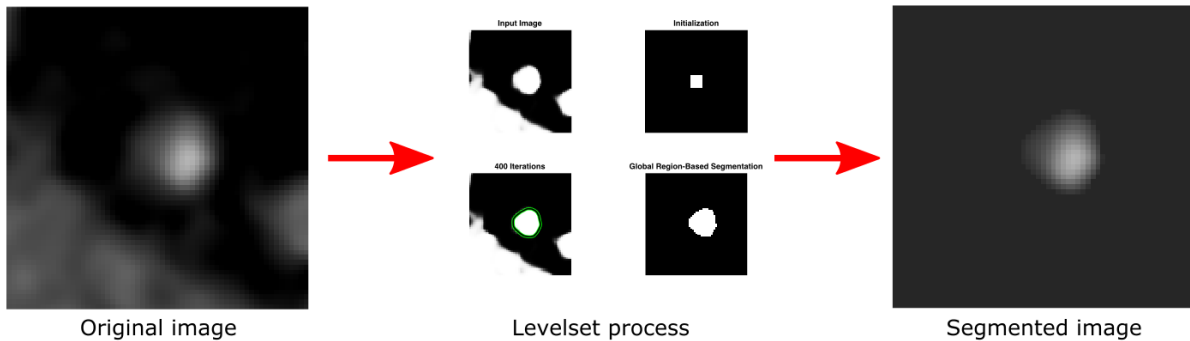
Figure 3.3: The result of applying the region-based active contour segmentation on an arbitrary cross-sectional view of an artery. This figure shows the original image, the initial seed for segmentation, the levelset boundary, and the final segmented image.

The third method available for arterial cross-section segmentation uses a multiscale vessel enhancement filter alongside with the region-based active contour levelset method. This method uses Frangi's artery vesselness enhancement algorithm to enhance vessel structures with the eventual goal of vessel segmentation [151]. The enhancement algorithm improves the accuracy of quantitative measurements of vascular morphology by reducing the organ over projection. This approach uses all the eigenvalues of the Hessian (second order information) to determine the likelihood of presence of a vessel, *i.e.* the algorithm finds tubular geometrical structures having a radius within a specified range.

To examine the local behavior of an image, we can use Taylor expansion in the neighboring areas of a specific point:

$$L(x_0 + \delta x_0, s) \approx L(x_0, s) + \delta x_0^T \Delta_{0,s} + \delta x_0^T \mathcal{H}_{0,s} \delta x_0 \tag{3.2}$$

where L is the image, x_0 specified point, s the measurement scale. $\Delta_{0,s}$ and $\mathcal{H}_{0,s}$ are the gradient vector and Hessian matrix computed at location x_0 and scale of s. Using linear space scale theory, the differentiation can be calculated using a convolution with derivatives of Guassians

$$\frac{\partial}{\partial x} L(x, s) = s^\gamma L(x) \frac{\partial}{\partial x} G(x, s)$$
$$G(x, s) = \frac{1}{\sqrt{2\pi s^2}^D} e^{\frac{-\|x\|^2}{2s^2}} \tag{3.3}$$

where D is the dimension of the DICOM image and γ was introduced by Lindeberg [152] to define a family of normalized derivatives. in the case no scale preference, γ is equal to one. The last term on Eq. 3.2 provides the second order directional derivative

$$\delta x_0^T \mathcal{H}_{0,s} \delta x_0 = \frac{\partial}{\partial \delta x_0} \frac{\partial}{\partial \delta x_0} L(x_0, s) \tag{3.4}$$

The eigenvalues of the Hessian can be used to find the principal directions where the local second order structure of 3D DICOM image can be decomposed. The eigenvalues of the Hessian can be calculated as follows

$$\lambda_{s,k} = \hat{u}_{s,k}^T \mathcal{H}_{0,s} \hat{u}_{s,k} \tag{3.5}$$

where $\lambda_{s,k}$ is the eigenvalue of the k-th eigenvector $\hat{u}_{s,k}$ at the scale of s. The eigenvectors

represent three orthonormal directions and when they are mapped by the Hessian, they are invariant up to a scaling factor. For example, the $\mathcal{H}_0$ maps a sphere with the center of x_0 and radius of 1 onto an ellipsoid with axes along the directions of $\hat{u}_k$ with corresponding semi-axis lengths equal to the λ_k. This ellipsoid represents the local second order structure of the image. In 3D HU image series, a pixel belonging to a vessel will have a small λ_1 while λ_2 and λ_3 are large. The sign of eigenvalues represents the brightness or darkness of the pixel. Since the intensity value along the vessel does not change drasticly from one pixel to another, $\hat{u}_1$ (which is assumed to be corresponding to the smallest eigenvalue λ_1) shows the direction along the vessel and $\hat{u}_2$ and $\hat{u}_3$ form a base for the orthogonal plane.

At this point, we can define a dissimilarity measure based on the calculated second order ellipsoid at each pixel. First, a blob-like structure needs to be identified. To do so, we can define a ratio that accounts for the deviation from such a structure

$$\mathcal{R}_B = \frac{\text{Volume}/4\pi/3}{(\text{Largest Cross-Section Area}/\pi)^{\frac{3}{2}}} = \frac{|\lambda_1|}{\sqrt{|\lambda_2\lambda_3|}} \tag{3.6}$$

For blob-like structure, the $\mathcal{R}_B$ is close to zero. Using this ratio, we are not able to distinguish between a line and a plane. To do so, we need to find the aspect ratio of the two largest second order derivatives, i.e. λ_2 and λ_3:

$$\mathcal{R}_A = \frac{(\text{Largest Cross-Section Area}/\pi)}{(\text{Largest Axis semi-length})^2} = \frac{|\lambda_2|}{|\lambda_3|} \tag{3.7}$$

In the Hounsfield Unit images, the arteries have higher intensity than the background and occupy a small volume of the 3D image series. This will lead to random noises in the vesselness enhancement algorithm. On the other hand, the magnitude of the derivatives for background pixels are mostly small. Thus, the norm of Hessian can be used to quantify these noises since the eigenvalues of this matrix are small. We can use the Frobenius matrix

norm to define a "second-order structureness" measure as follows

$$S = \|\mathcal{H}\|_F = \sqrt{\sum_{j \leq D} \lambda_j^2} \tag{3.8}$$

The value of S will be small for the background structure since the λ_ks are small and it will be larger for high contrast regions. Thus, considering the criteria presented in Eqs. (3.6-3.7), we can define a vesselness function as follows:

$$\mathcal{V}_0(s) = \begin{cases} 0 & \text{if} \lambda_2 > 0 \quad \text{or} \quad \lambda_3 > 0 \\ (1 - exp(-\frac{\mathcal{R}_A^2}{2a^2}))exp(-\frac{\mathcal{R}_B^2}{2b^2}))(1 - exp(-\frac{\mathcal{S}^2}{2c^2})) \end{cases} \tag{3.9}$$

where a, b, and c are coefficients that control the sensitivity of the filter to the $\mathcal{R}_A$, $\mathcal{R}_B$, and $\mathcal{S}$, respectively. The proposed values for a, b, and c in the literature are 0.5, 0.5, and half of the Hessian norm, respectively. The combination of all three criteria using their product is to ensure the response of filter is maximum if all the criteria are met.

To filter all the structures within a specific size range, i.e. from a scale s_{min}, to s_{max}, we can integrate the vesselness measure at different scales:

$$\mathcal{V}_0(\gamma) = \max_{s_{min} \leq s \leq s_{max}} \mathcal{V}_0(s, \gamma) \tag{3.10}$$

Figure 3.4 shows the 3D view of the original CCTA and the 3D view of filtered CCTA.

The fourth and the last method available for arterial cross-section segmentation is a combination of vesselness enhancement algorithm and an outer wall and plaque membership functions. The Frangi's vesselness enhancement algorithm is used to find the tubular structures in the 3D DICOM image series and reduce the background noise around the arteries.

51
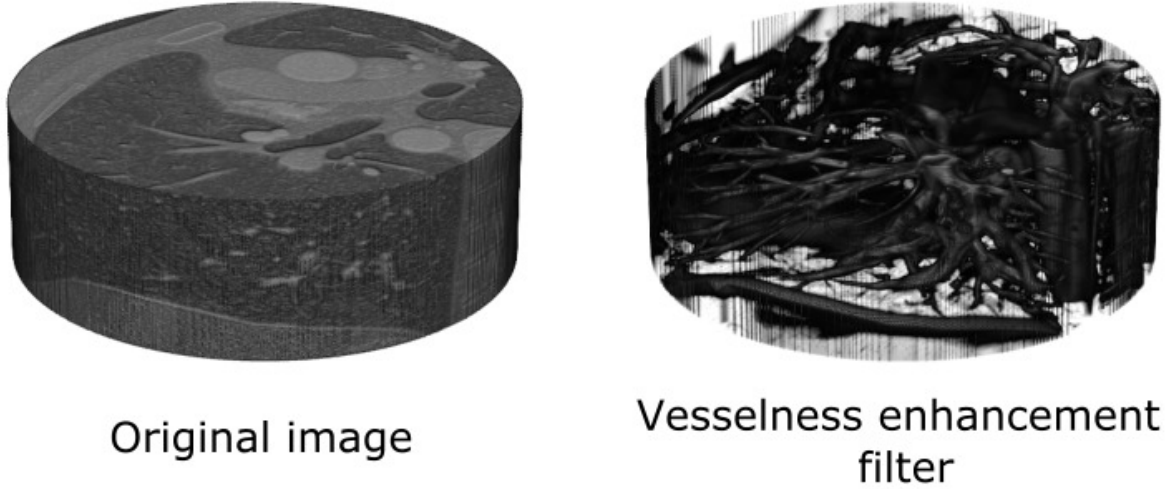
Figure 3.4: The 3D visualization of CCTA image series. Left panel shows the HU volumetric image and the right panel shows the same volumetric image after applying the Frangi's vessel enhancement filter.

Although this filter works well to extract the luminal region, it might neglect arterial wall and the diseased areas due to drastic changes in the contrast of the image. To resolve this issue, we can define outer-wall and plaque membership functions to include the vessel wall in the segmentation process as well.

To do so, first the Frangi's vesselness enhancement filter is applied on the DICOM image series. Then, the average lumen intensity $\bar{I}_{lumen}$ is calculated based on the intensity of the centerline points. Based on Kigka *et al.* work [153], a membership function for the outer wall can be defined as follows:

$$f_{outer/plaque} = (1 - \epsilon).g_{sigm}(x; a_{outer/plaque}, b_{outer/plaque}) + \epsilon$$

$$g_{sigm}(x; a, b) = \frac{1}{1 + exp(-a(x - b))}$$

(3.11)

where $a_{outer} = 0.02$, $a_{plaque} = 0.05$, $b_{outer} = \min\left(200, \max\left(\bar{I}_{lumen} - l_{thres} - ncp_{thres}, 100\right)\right)$, and $b_{plaque} = \bar{I}_{lumen} + cp_{thres}$. The parameter $\epsilon = 0.05$ is the weight of the membership function. $l_{thres} = 80HU$ is the threshold value for the lumen, $cp_{thres} = 400HU$ is the calcified plaque threshold, and $ncp_{thres} = 50HU$ is the non-calcified plaque threshold [154, 155].

By combining the regions obtained by Eqs. 3.11 and 3.10, we can generate the cross-sectional segments of the artery with minimal organ layover, reduced background noise, and accurate vessel wall intensities.

3.2.3   Segmentation of arterial wall and plaque quantification

This section of the software was developed with the purpose of quantitative and qualitative assessment of arterial cross-sections. Fig. 3.5 shows the *plaque quantification* section. User can import a single DICOM image or a series of DICOM images for quantification process using the *import .dcm* panel on the top left of the screen. The *Plaque Quantification Parameters* panel gives the user the three options: Manual quantification of plaques by specifying the HU ranges for the lumen, and low attenuation, fibrous, and calcified plaques; adaptive threshold method (semi-automatic segmentation); and automatic segmentation. Also, the user can set the window width and window level to better visualize the arterial cross-section. The *ROI Manager* panel contains different algorithms for plaque assessment. If only one image is selected for quantification, the *draw ROI* button will be available to user. This button gives the user the ability to manually select the region of interest using a free-hand tool. If a DICOM image series is selected, the *propagate ROI* will become available to user. Depending on the selection of automatic or semi-automatic segmentation, this button redirects the user to different screens.

Manual quantification of plaques. This option requires four input from the user: HU threshold for lumen, and low attenuation, fibrous, and calcified plaques. The software is designed in a way that read the DICOM image and store it in the form of a matrix whose dimensions are equal to the number of pixel in each row and column of the image. The element values in this matrix is the HU values of the image. Thus, it is possible to segment the image by finding the elements of the matrix having an HU value in the prescribed threshold. To obtain
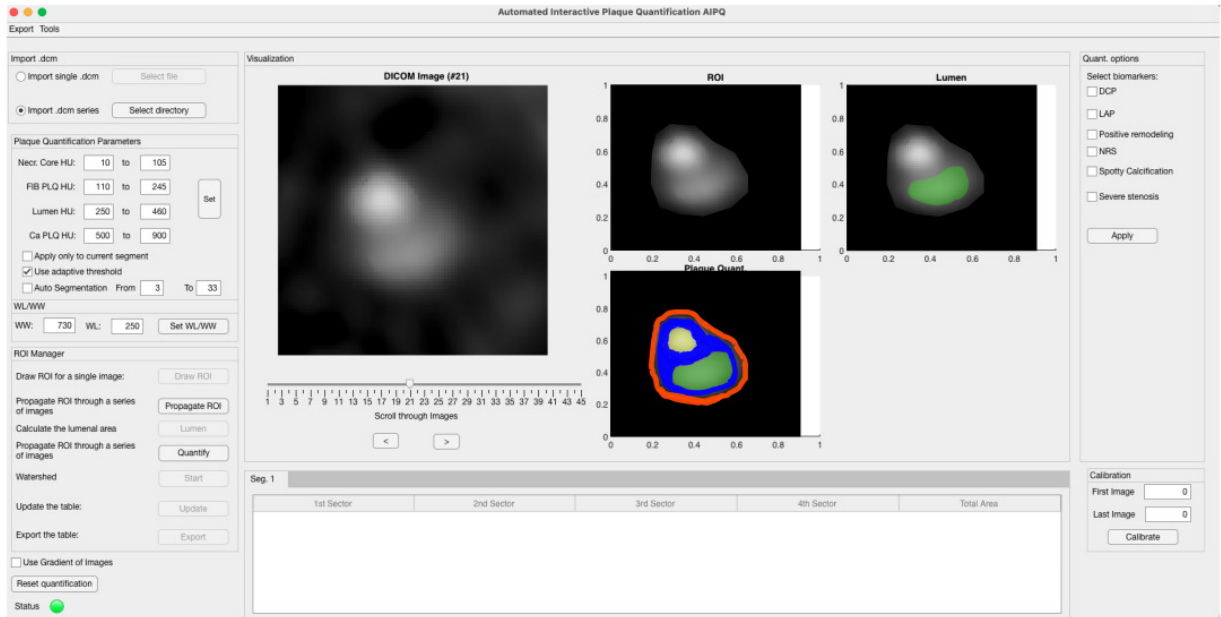
Figure 3.5: The quantification screen. This figure also shows the overlayering of different plaque characteristics on top of the segmented image.

the area of each calculated segment, one can use the DICOM header metadata and find the physical resolution of each pixel and multiply them to get the pixel area and then multiply it with the number pixel in the prescribed HU interval. The software will automatically create patches on each DICOM image for different plaque composition as well as the arterial lumen. If only one image is selected, the user can enter the HU threshold for different plaque composition in panel *Plaque Quantification Parameters* and then select *Draw ROI* from the *ROI Manager* panel and select the region of interest using the free-hand tool provided in the software. Then, the user can quantify different areas by pressing *Quantify* button which shows the results in a table at the bottom of the screen.

If a series of DICOM images is selected, two options are given to the user for quantifying the plaque composition. The first option is automatic generation of ROIs throughout the series and then using the prescribed HU threshold in panel *Plaque Quantification Parameters* to quantify the lumen and different type of plaques. To start this process, the *Auto Segmentation* checkbox should be selected and the slice number related to the desired first

54

and last image should be entered. Then user can press *propagate ROI* which redirects the user into the cross-section segmentation screen, see Fig. 3.6. In the *propagate ROI* screen, there are three sections: the first image is shown on the top left of the screen, the last image is located on the top right, and the image with ROI as an overlayer is shown at the bottom of the screen. This screen gives the user to draw the first and last ROIs on the images using a free-hand tool and by pressing the *Propagate ROI* bottom, the ROIs in all the selected images will be calculated based on the ROIs drawn by the user. The user has the ability to scroll through ROIs and modify them. By pressing the *Accept all ROIs*, the ROIs are transferred to the previous screen for plaque quantification procedure. The use can press *Quantify* button to get the lumen area as well as areas of different types of plaque.

One of the problems with fixed threshold quantification is the presence of an artificial lumen around a calcified plaque. Since the intensity of calcified plaques is higher than the lumen, using the fixed threshold method will result in a ring around the calcified plaque and consider it as the lumen. To resolve this problem, a watershed algorithm is implemented in the software to split the lumen area based on catchment basins and watershed ridge lines. Figure 3.7 shows the divided lumen using the watershed algorithm. This algorithm treats the lumen as a surface where light pixels represent high elevations and dark pixels represent low elevations and transforms a continuous segment into distinct areas.

The second option for quantifying the plaque composition is the semi-automatic quantification of the arterial cross-section. This option uses an adaptive method to calculate the HU threshold for each type of plaque. The fixed thresholds has been widely used in the literature for quantifying the plaque composition in CCTA. However, it has been shown that the intensity of the lumen can affect the plaque tissue characterization [148]. Also, the intensity of the lumen in CTA images decreases along the artery, specially in regions with severe stenosis. To overcome this issue, one can utilize an adaptive HU threshold depending on the regional attenuation of the pixel intensity in the lumen.
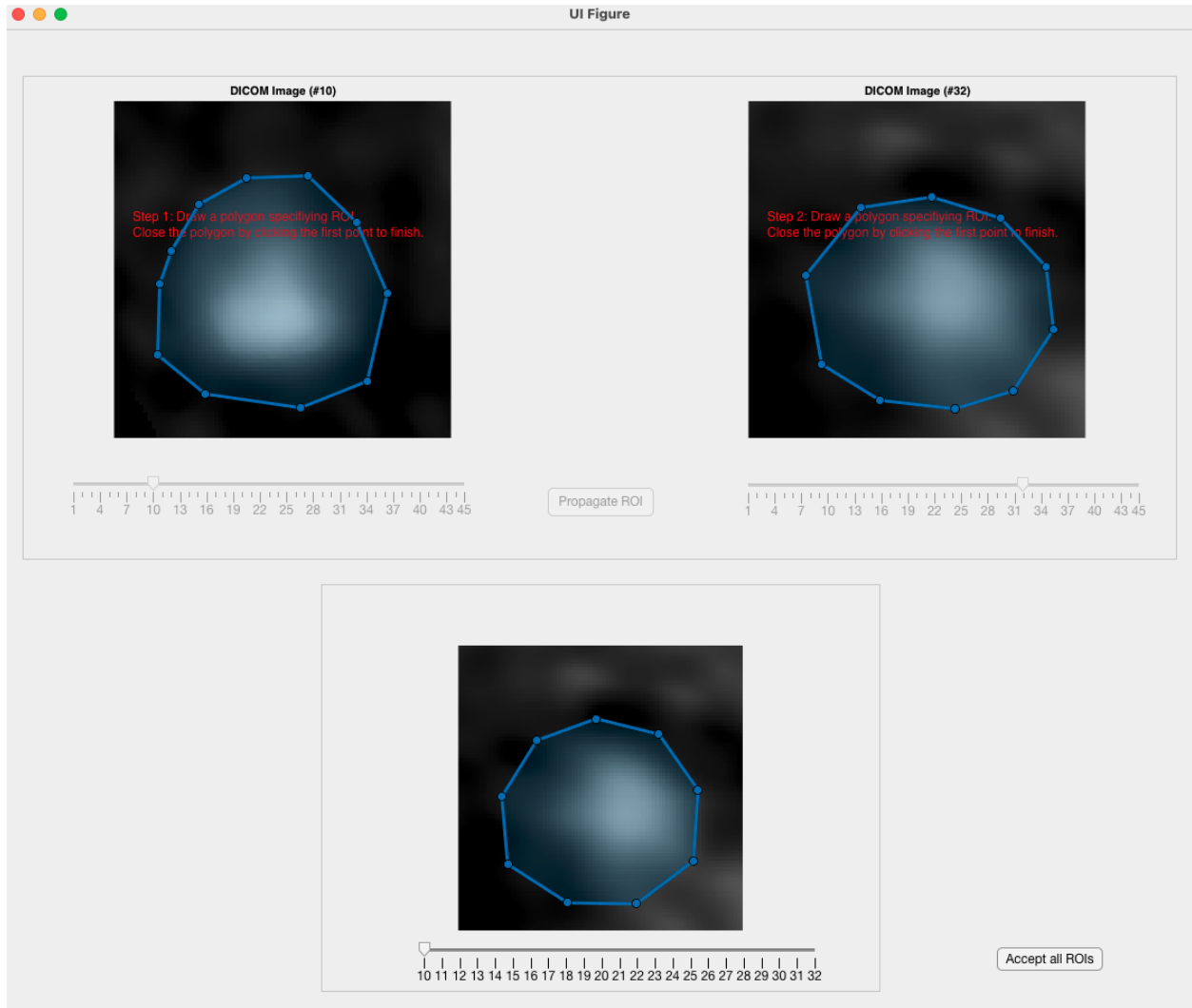
Figure 3.6: The cross-section segmentation screen. User can scroll through images and create regions of interest for the first and last image. The ROIs for other images will be automatically generated.

The first step in adaptive threshold assessment of plaque characteristics is to find the mean lumen intensities from the proximal to the distal part of the artery $(\bar{I})$. Then a trendline can be fitted through mean lumen intensities $(\bar{I}_{fit})$. The upper threshold for non-calcified plaques can be written as

$$NC_{max} = \min\left(\bar{I}_{fit} - 200, 75\right) \tag{3.12}$$

If there is a severe stenosis in a segment, we can modify the NC_{max} to account for the

56

| Original image | Fixed threshold segmentation of lumen | Divided lumen using watershed | Final lumen |
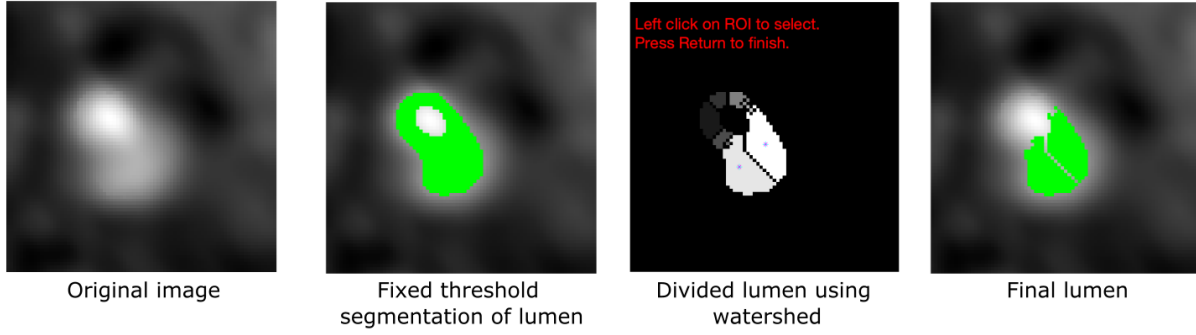
Figure 3.7: The quantification screen. This figure also shows the overlayering of different plaque characteristics on top of the segmented image.

decrease in the intensity of the lumen:

$$NC_{max} = NC_{max} - 1.25(\bar{I}_{fit} - \bar{L}) \quad (3.13)$$

the lower threshold of dense calcified plaque can be calculate as

$$DC_{min} = \max{(\bar{I}_{fit} + 100, 450)} \quad (3.14)$$

If the area of calcified plaque is large, we can modify the DC_{min} as follows:

$$DC_{min} = DC_{min} + 0.25(\bar{I}_{fit} - \bar{L}) \quad (3.15)$$

The lower threshold for fibrous tissue can be calculated as

$$FT_{min} = 0.2(DC_{min} - NC_{max}) \quad (3.16)$$

Thus, this method needs the mean lumen intensities along the vessel to calculate the thresholds corresponding to different plaque composition. In the developed software, the user can

select *Use adaptive threshold* and press the *propagate ROIs* button. The user will be redirected to another screen. see Fig. 3.8. This section of the software has two main panels: ROI propagation and HU trends. In the *Propagation ROIs* panel, four images can be seen, the original image and ROI curve, the gradient magnitude image with ROI overlayer shown with pink color, the gradient magnitude image and the ROI curve, and the final segmented image. The gradient magnitude image shows the boundaries of the structures inside an image in a way that the intensity of pixels on the structure boundary is higher than the surroundings. Based on the gradient magnitude image, the software creates labels for the structures with closed boundaries and finds the biggest structure. Then it fits a polygonal to the boundary of this structure which is the final ROI. It is possible for user to interactively modify the calculated ROI by changing the location of points on the fitted curve on any of the images.
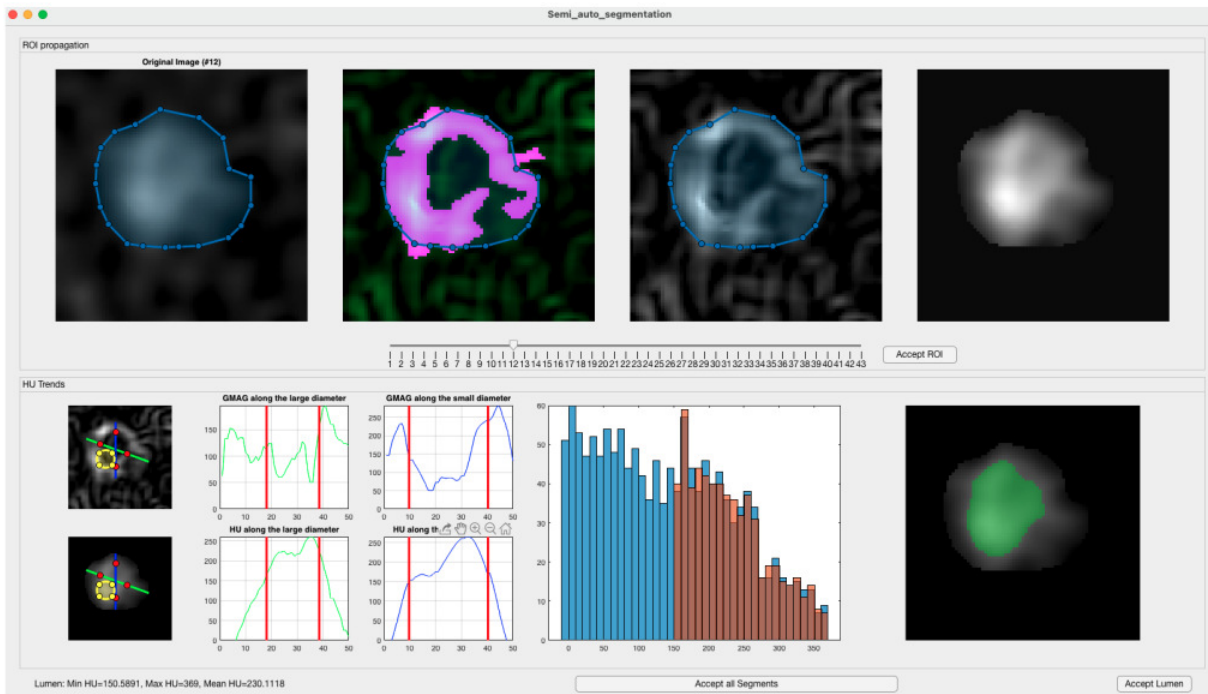
Figure 3.8: The screen for semi-automatic segmentation of the arterial cross-section.

Pressing the *Accept ROI* button will show the the values of HU and gradient magnitude along the smallest and longest axis of the ROI in the *HU trend* panel. The axes are shown

on both gradient magnitude and segmented images. The software provides sliders on these axes to control the lumen threshold. User can drag any of these sliders into a desired position. Also, in case of presence of a calcified plaque, since the maximum intensity on the ROI will belong to the calcium image, a circle is provided on both images that user can drag and find the maximum lumen intensity. The gradient magnitude curves show a the trend of this parameter on the axes. Since the boundaries of the structure has the highest gradient magnitude, there will be two peaks on each curve corresponding to the beginning and end of lumen area. On each plot, two vertical lines are provided to user in order to accurately modify the the lumen threshold. User also can see the histogram of the intensities inside the ROI in this panel. When the lumen threshold changes by user, the color of histogram bars corresponding to the lumen changes to orange. The final segmented lumen cam be seen in the right side of the panel. User can press the *Accept lumen* button to store the segment and the lumen threshold values and move on to the next image. After finishing the segmentation for all the images, user can press *Accept all Segments* to return to the plaque quantification screen.

The next step for user is to use *Quant. options* panel to select the qualitative characteristics of the plaques. These characteristic include dense calcium plaque (DCP), low attenuation plaque (LAP), napkin-ring sign (NRS), spotty calcification (SC), and severe stenosis (SS). Now, by pressing the *Quantify* button, the software will automatically calculates the luminal area as well as the areas of different types of plaque using the adaptive threshold method. The calculated data will be shown in the table at the bottom of the screen. User can press *Export* button to store the quantification results on disk in Microsoft Excel Spreadsheet format.

3.2.4   3D model segmentation

This section explains the procedure in which the 3D model of the arterial wall containing the values of wall shear stress and biotransport data can be segmented in a way that conforms with the CCTA segmentation. The developed code for 3D segmentation is written in python and uses The Visualization Toolkit (VTK) and the Vascular Modeling Toolkit (VMTK) packages. The goal of this software is to match the centerline of a 3D model to the centerline used to do the segmentation in the plaque quantification software and use the same slicing criteria for 3D segmentation. One of the problems with 3D modeling and scaling the 3D model of the arteries is the rotation and translation of the geometry during the numerical simulation due to changes in the reference coordinates. The developed 3D segmentation software will match the transformed geometry with the original one.

The input to the 3D segmentation code is the 3D model of the artery, 3D model of the artery containing the hemodynamics and transport data, the centerline generated in the plaque quantification software, and the coordinates of a bifurcation point.

First, the software reads the 3D model of the artery and asks the user to tag the inlet and outlet surfaces. Then, the software extracts the centerline for this arterial model and splits its branches. see Fig. 3.9. VMTK can recover the topology of the arterial tree from the centerlines and their corresponding inscribed sphere radius. Thus, one can reconstruct the geometry using a tube around the centerline and a local radii equal to the corresponding maximum inscribed sphere. The bifurcation points can be found by finding the intersection of each two tubes. For each bifurcation, six reference points can be identified, i.e. on each centerline the first point is located at the intersection of a centerline with another tube and the second one is located one maximum inscribed sphere upstream.

The developed software finds and visualizes these reference points for each bifurcation on the arterial tree (see Fig. 3.9) and asks the user to select candidates points on the centerline.
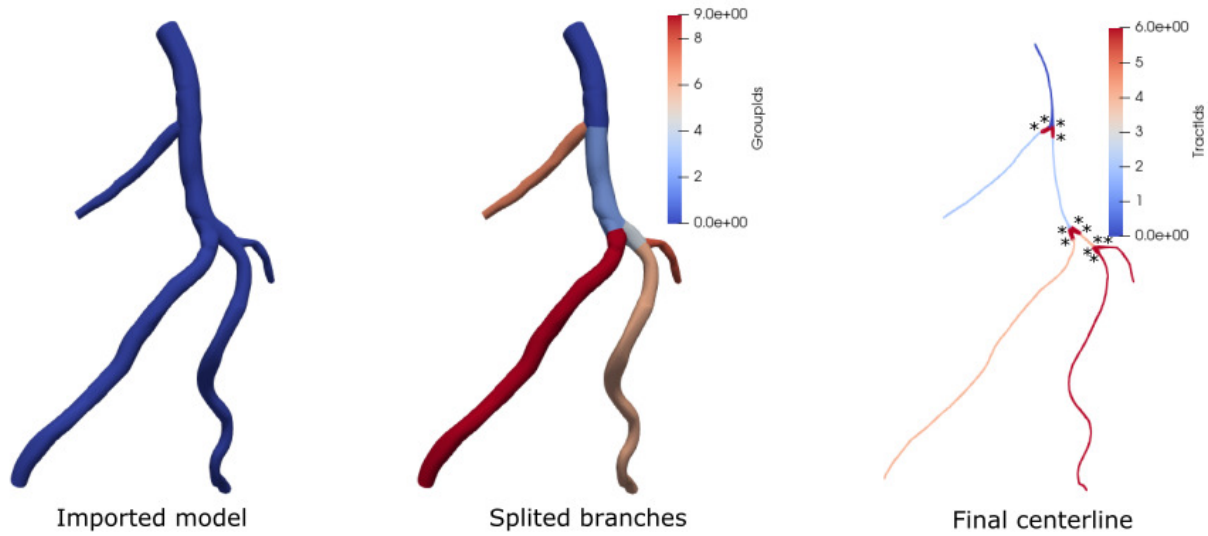
Figure 3.9: The left panel shows the imported 3D model into the 3D model segmentation software. The middle panel shows the model with extracted branches based on the calculated reference points. The right panel shows the extracted centerline in which the end points of each red thick lines at bifurcations are the reference points (marked with asterisk).

User can interactively rotate the centerline, zoom in/out, and select the points by clicking on it. Doing so, the selected point will be shown in red color. To confirm the point, user should press P key on the keyboard and the color of confirmed point changes to green. After selecting all the reference points, user can press *return* and the software will show the 3D model of the artery containing the hemodynamics. The process of creating the centerline is repeated for this model and the user is asked to select the corresponding points on this model as the previous one.

After selecting the matching reference points, the software uses a Kabsch transformation algorithm [156, 157] to transform the 3D model of the artery containing the hemodynamics into a spatial position that its centerline matches the 3D geometry created from the CCTA images.

The software uses the coordinate of the input bifurcation and a segment length to generate a 3D segment matching with the CCTA segmentation results and store each of them in *.vtk* format. Also, the area-weighted average of WSS and biotransport data will be stored in a file for all of the segments.

61

3.2.5 Statistical analysis

Statistical analysis was performed in Matlab (R2019a Update 9). The quantified plaque characteristic including areas of lumen, low attenuation plaque, fibrous plaque, calcified plaque, vessel volume, presence of positive remodeling, and napkin-ring sign as well as the area-weighted average wall shear stress (WSS), WSS divergence, absolute WSS divergence field, low density lipoprotein concentration, and nitric oxide concentration for each segment in baseline and follow-up were imported into the Matlab software. The difference from baseline to follow up for quantitative parameters including lumen, low attenuation plaque, fibrous plaque, calcified plaque, and vessel volume were calculated. The qualitative parameters including presence of positive remodeling, napkin-ring sign, and growth of the vessel wall were only calculated for the follow-up dataset. The dataset was divided into two groups: single patient dataset and a complete dataset. The former dataset contains the data related to each patient and the later contains the data of all the patients together. The Spearman correlations were calculated to find the correlation between quantitative parameters and the area-weighted average wall shear stress (WSS), WSS divergence, absolute WSS divergence field, low density lipoprotein concentration, and nitric oxide concentration. The Point biserial correlation method was used to find the correlation between the qualitative parameters and the hemodynamic/biotransport parameters. For this analysis, the 95 % confidence intervals (95 % CI) were calculated and a p-value ≤ 0.05 was considered statistically significant [158].

3.3 Results

Baseline patient characteristics were shortly discussed in Chapter 2. For this analysis 8 coronary models showing vulnerable atherosclerotic plaques were used. Both the CTA and 3D models were segmented using the in-house developed software. The CTA-derived segments were 1 mm apart while the 3D model segments were generated in a way that their length

along the centerline was 1 mm. Each CTA segment is located in the middle of the corresponding 3D model segment as shown in Fig. 3.10. The total number of segments (CTA and 3D model) used to find correlations was 538.
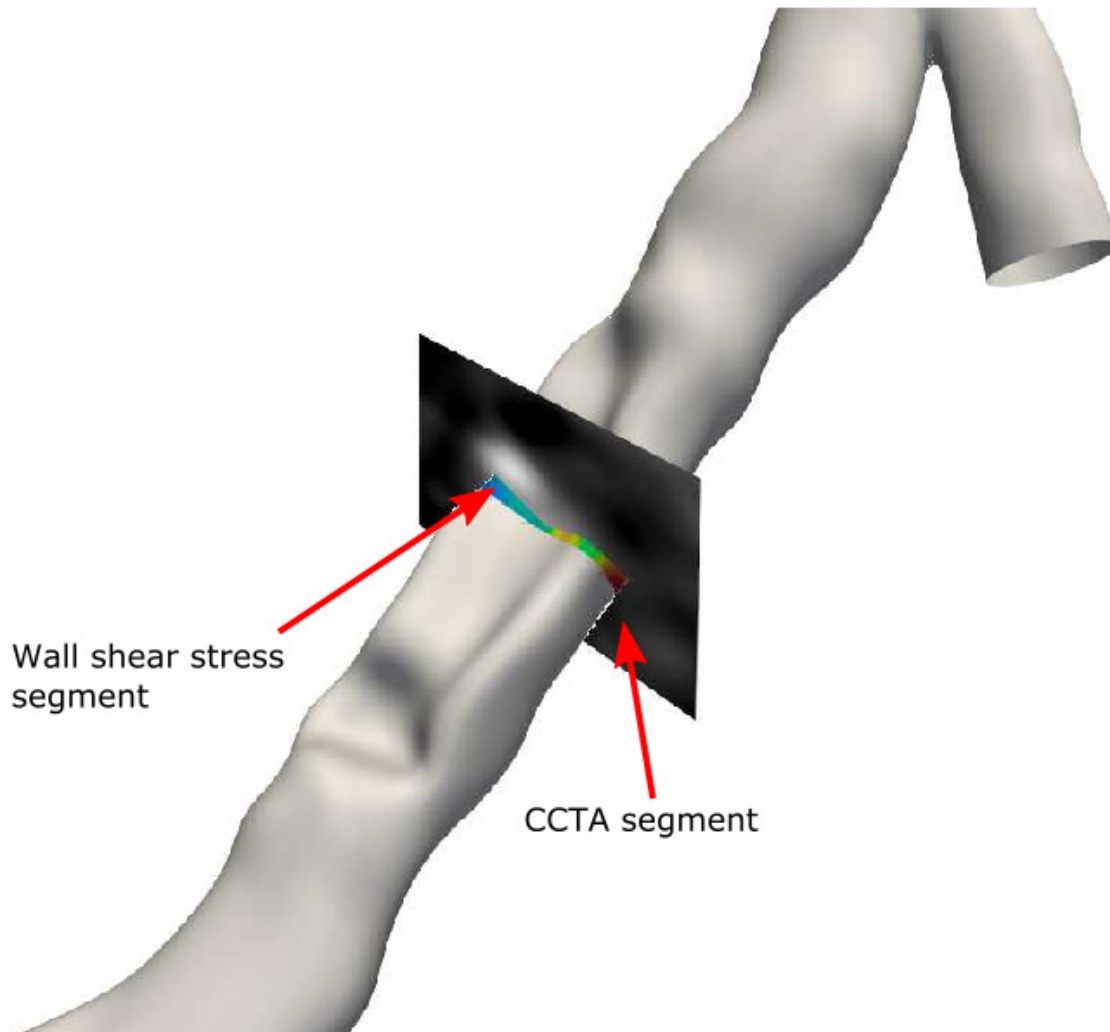
Figure 3.10: A sample of CTA segment on top of the 3D geometry. The 3D segmentation carried out in a way that the CTA segment was located in the middle of the 3D segment.

3.3.1 Single patient study

The results of correlations between changes in the volume of the lumen from baseline to follow-up are shown in Table 3.1. The changes in the lumen area do not show any meaningful

correlation with the hemodynamic and biotransport parameters while analyzing the data patient-by-patient. Tables 3.2 and 3.3 show the results of correlations between changes in the low attenuation plaque (LAP) volume from baseline to follow-up and the percentage of change with respect to baseline case, respectively. The correlation results show that the longitudinal changes in the LAP volume have a moderate correlation with the local WSS at the baseline in patients P1-P3, P6, and P8. Since the volume of plaques and the vessel wall varies between different patients and different segments, the percentage of longitudinal change was considered as a separate parameter to ensure that changes in the quantitative parameters are normalized based on the baseline values.

Table 3.1: The correlations between changes in the lumen volume and various hemodynamic parameters. Values in bold font indicate statistically significant differences ($P < 0.05$).

Hemodynamic Parameter		P1	P2	P3	P4	P5	P6	P7	P8
WSS	R	0.230	−0.203	0.126	−0.163	0.024	0.117	0.454	0.209
	P	0.197	0.329	0.410	0.398	0.870	0.559	**0.014**	0.257
WSS Div.	R	0.037	0.031	0.042	0.160	−0.063	0.145	0.568	−0.102
	P	0.839	0.884	0.783	0.407	0.665	0.468	**0.002**	0.584
|WSS Div.|	R	0.122	−0.172	−0.048	0.132	0.125	−0.037	0.521	−0.006
	P	0.497	0.411	0.752	0.495	0.386	0.854	**0.004**	0.977
Div. of Norm. WSS	R	0.094	0.212	0.247	0.204	−0.184	0.028	0.358	−0.024
	P	0.602	0.307	0.102	0.287	0.200	0.890	0.058	0.899
|Div. of Norm. WSS|	R	0.038	−0.192	0.150	−0.161	0.280	−0.136	0.313	−0.170
	P	0.833	0.355	0.326	0.402	**0.049**	0.499	0.099	0.359
NO	R	0.439	−0.057	−0.089	−0.287	0.072	0.118	0.274	0.736
	P	**0.026**	0.806	0.610	0.155	0.681	0.581	0.149	$\mathbf{5.106 \times 10^{-6}}$
LDL	R	−0.062	0.229	0.006	0.098	−0.071	−0.117	0.197	0.159
	P	0.764	0.317	0.975	0.632	0.685	0.583	0.304	0.392

Table 3.2: The correlations between percentage of change in the LAP volume and various hemodynamic parameters. Values in bold font indicate statistically significant differences ($P < 0.05$).

Hemodynamic Parameter		P1	P2	P3	P4	P5	P6	P7	P8
WSS	R	−0.315	−0.321	−0.409	0.147	−0.161	−0.382	−0.184	−0.327
	P	**0.004**	$\mathbf{3.506 \times 10^{-4}}$	**0.007**	0.122	0.088	$\mathbf{354\,729 \times 10^{-4}}$	0.216	**0.001**
WSS Div.	R	0.070	0.121	0.007	−0.016	0.143	−0.206	−0.484	0.192
	P	0.698	0.564	0.965	0.936	0.320	0.302	**0.008**	0.301
|WSS Div.|	R	0.113	0.031	−0.207	0.016	−0.099	−0.089	−0.460	−0.036
	P	0.529	0.884	0.173	0.934	0.494	0.657	**0.013**	0.846
Div. of Norm. WSS	R	0.152	−0.028	−0.082	0.251	0.105	−0.072	−0.285	0.292
	P	0.396	0.896	0.593	0.189	0.467	0.720	0.134	0.112
|Div. of Norm. WSS|	R	−0.075	0.242	−0.087	0.174	−0.261	−0.318	−0.146	0.173
	P	0.678	0.244	0.571	0.365	0.068	0.106	0.447	0.351
NO	R	−0.499	0.078	−0.007	0.084	0.018	−0.174	−0.215	−0.600
	P	**0.010**	0.737	0.970	0.683	0.916	0.415	0.261	$\mathbf{4.707 \times 10^{-4}}$
LDL	R	−0.137	−0.012	0.300	−0.337	−0.351	0.007	−0.074	0.069
	P	0.503	0.962	0.081	0.093	**0.039**	0.976	0.700	0.712

Tables 3.4 and 3.5 show the correlation results for the changes in fibrous plaque (FP) based on

Table 3.3: The correlations between changes in the LAP volume and various hemodynamic parameters. Values in bold font indicate statistically significant differences ($P < 0.05$).

Hemodynamic Parameter		P1	P2	P3	P4	P5	P6	P7	P8
WSS	R	-0.347	-0.297	-0.411	0.127	-0.172	-0.386	-0.166	-0.279
	P	**0.021**	**4.765×10^{-4}**	0.085	0.196	0.129	**0.001**	0.196	**0.006**
WSS Div.	R	0.079	0.082	0.014	0.040	0.127	-0.306	-0.480	0.124
	P	0.660	0.695	0.927	0.835	0.379	0.120	**0.009**	0.504
|WSS Div.|	R	0.108	0.062	-0.184	-0.004	-0.144	-0.053	-0.453	-0.084
	P	0.547	0.770	0.225	0.983	0.316	0.795	**0.014**	0.653
Div. of Norm. WSS	R	0.156	0.005	-0.029	0.267	0.116	-0.148	-0.282	0.265
	P	0.384	0.984	0.850	0.160	0.422	0.459	0.138	0.150
|Div. of Norm. WSS|	R	-0.103	0.235	-0.081	0.176	-0.279	-0.330	-0.152	0.150
	P	0.567	0.256	0.597	0.359	0.050	0.093	0.430	0.420
NO	R	-0.510	0.036	-0.026	0.047	-0.034	-0.165	-0.275	-0.615
	P	**0.009**	0.877	0.883	0.820	0.847	0.439	0.148	**3.066×10^{-4}**
LDL	R	-0.139	-0.035	0.368	-0.316	-0.319	-0.048	-0.130	0.048
	P	0.496	0.881	**0.030**	0.116	0.062	0.825	0.501	0.797

the hemodynamic and biotransport parameters. As it can be seen, the correlations between changes in fibrous plaque volume and WSS divergence, absolute WSS divergence, divergence of normalized WSS, and LDL are not significant. However, these tables show that the local concentration of NO reveals moderate correlation with the longitudinal changes in fibrous plaque volume.

Table 3.4: The correlations between percentage of change in the FP volume and various hemodynamic parameters. Values in bold font indicate statistically significant differences ($P < 0.05$).

Hemodynamic Parameter		P1	P2	P3	P4	P5	P6	P7	P8
WSS	R	-0.293	0.185	-0.195	0.137	-0.318	0.076	-0.144	-0.499
	P	**0.098**	0.154	**0.002**	0.500	0.074	0.072	**0.015**	**0.005**
WSS Div.	R	0.094	0.225	-0.123	-0.122	0.149	-0.008	-0.277	0.214
	P	0.602	0.279	0.420	0.526	0.300	0.970	0.145	0.247
|WSS Div.|	R	-0.040	-0.302	0.086	0.104	-0.013	0.054	-0.238	-0.211
	P	0.826	0.142	0.575	0.590	0.927	0.790	0.212	0.253
Div. of Norm. WSS	R	0.010	-0.033	-0.266	-0.043	0.039	0.292	-0.070	0.209
	P	0.956	0.876	0.077	0.825	0.789	0.139	0.718	0.258
|Div. of Norm. WSS|	R	-0.072	0.205	-0.346	0.168	-0.118	-0.100	-0.027	0.114
	P	0.692	0.325	**0.021**	0.381	0.414	0.620	0.891	0.540
NO	R	-0.311	0.205	0.204	0.533	-0.208	-0.351	-0.100	-0.682
	P	0.122	0.371	0.238	**0.006**	0.229	0.093	0.603	**3.821×10^{-5}**
LDL	R	0.016	-0.155	-0.004	0.012	-0.295	0.132	-0.105	0.203
	P	0.939	0.502	0.984	0.955	0.086	0.537	0.585	0.272

The changes in calcium plaque (CP) volume and the total vessel wall (VW) volume in the understudy population were not significant. Tables 3.6 and 3.7 shows the correlation between longitudinal changes in the CP and vessel wall (VW) volumes for various hemodynamic parameters. The VW is calculate as the sum of LAP, FP, and CP volumes.

Table 3.5: The correlations between changes in the FP volume and various hemodynamic parameters. Values in bold font indicate statistically significant differences ($P < 0.05$).

Hemodynamic Parameter		P1	P2	P3	P4	P5	P6	P7	P8
WSS	R	−0.300	0.190	−0.170	0.095	−0.310	0.093	−0.140	−0.490
	P	0.060	0.110	**0.001**	0.480	0.100	0.051	**0.033**	**0.001**
WSS Div.	R	0.072	0.180	−0.124	−0.055	0.238	−0.002	−0.275	0.242
	P	0.690	0.388	0.417	0.778	0.095	0.991	0.149	0.190
|WSS Div.|	R	−0.100	−0.273	0.063	0.110	−0.057	0.051	−0.236	−0.213
	P	0.577	0.186	0.679	0.567	0.694	0.802	0.217	0.248
Div. of Norm. WSS	R	0.025	−0.071	−0.281	−0.010	0.093	0.349	−0.080	0.171
	P	0.890	0.736	0.062	0.960	0.519	0.075	0.678	0.355
|Div. of Norm. WSS|	R	−0.096	0.259	−0.346	0.121	−0.157	−0.119	−0.040	0.012
	P	0.594	0.210	**0.020**	0.531	0.277	0.553	0.835	0.951
NO	R	−0.352	0.217	0.165	0.438	−0.305	−0.223	−0.065	−0.723
	P	0.078	0.343	0.343	**0.026**	0.075	0.292	0.737	$\mathbf{8.283 \times 10^{-6}}$
LDL	R	0.017	−0.113	0.026	0.037	−0.189	0.295	−0.079	0.179
	P	0.936	0.625	0.881	0.857	0.275	0.162	0.682	0.333

Table 3.6: The correlations between changes in the CP volume and various hemodynamic parameters. Values in bold font indicate statistically significant differences ($P < 0.05$).

Hemodynamic Parameter		P1	P2	P3	P6	P7	P8
WSS	R	0.067	−0.254	−0.088	0.306	0.498	0.080
	P	0.711	0.221	0.566	0.120	**0.006**	0.671
WSS Div.	R	0.102	−0.039	0.073	0.163	0.470	−0.155
	P	0.572	0.853	0.632	0.418	**0.010**	0.405
|WSS Div.|	R	0.025	−0.002	0.188	0.293	0.470	−0.045
	P	0.888	0.991	0.217	0.138	**0.010**	0.809
Div. of Norm. WSS	R	0.129	0.083	0.055	−0.051	0.447	0.037
	P	0.473	0.694	0.718	0.800	**0.015**	0.844
|Div. of Norm. WSS|	R	−0.151	−0.206	0.074	0.347	0.447	0.022
	P	0.402	0.322	0.628	0.076	**0.015**	0.906
NO	R	0.114	0.307		0.258	0.427	0.513
	P	0.579	0.176		0.223	**0.021**	**0.003**
LDL	R	−0.031	0.315		−0.187	0.276	−0.126
	P	0.879	0.165		0.382	0.147	0.500

The qualitative vulnerable plaque characteristics considered in this study are positive remodeling (PR) and napkin-ring sign (NRS). The presence of these qualitative parameters in the follow-up images is compared with the hemodynamics and biotransport results in baseline models. The patient-by-patient correlations between for these plaque characteristics and the hemodynamic parameters are provided in Tables 3.8 and 3.9. It should be noted that patients P2, P4, P7, and P8 did not show any positive remodeling at the follow-up. Also,

Table 3.7: The correlations between changes in the vessel wall volume and various hemodynamic parameters. Values in bold font indicate statistically significant differences ($P < 0.05$).

Hemodynamic Parameter		P1	P2	P3	P4	P5	P6	P7	P8
WSS	R	−0.283	−0.121	−0.025	0.382	0.096	−0.059	−0.191	−0.413
	P	0.110	0.564	0.871	**0.042**	0.508	0.771	0.320	**0.022**
WSS Div.	R	0.178	0.138	0.061	0.052	0.157	−0.198	−0.408	0.147
	P	0.321	0.508	0.690	0.789	0.274	0.320	0.029	0.428
|WSS Div.|	R	−0.020	−0.079	−0.175	0.080	−0.081	0.001	−0.369	−0.201
	P	0.912	0.706	0.248	0.680	0.573	0.999	**0.050**	0.277
Div. of Norm. WSS	R	0.179	−0.160	−0.127	0.192	0.035	0.057	−0.137	0.246
	P	0.318	0.443	0.403	0.318	0.807	0.778	0.477	0.181
|Div. of Norm. WSS|	R	−0.078	0.351	−0.181	0.241	−0.279	−0.259	−0.039	0.070
	P	0.664	**0.086**	0.233	0.206	**0.050**	0.192	0.839	0.707
NO	R	−0.362	0.339	0.057	0.208	−0.075	−0.267	−0.200	−0.620
	P	**0.070**	0.133	0.745	0.306	0.667	0.207	0.298	$\mathbf{2.676 \times 10^{-4}}$
LDL	R	−0.083	0.117	0.298	−0.262	−0.380	0.084	−0.103	0.047
	P	0.686	0.613	0.083	0.195	**0.025**	0.694	0.592	0.801

NRS was not present in any of patients P2, P4, and P8.

Table 3.8: The correlations between presence of positive remodeling (PR) in the follow-up images and various hemodynamic parameters. Values in bold font indicate statistically significant differences ($P < 0.05$).

Hemodynamic Parameter		P1	P3	P5	P6
WSS	R	0.703	0.277	−0.222	0.043
	P	$\mathbf{3.067 \times 10^{-6}}$	0.062	0.117	0.829
WSS Div.	R	−0.148	0.511	0.021	0.018
	P	0.403	$\mathbf{2.814 \times 10^{-4}}$	0.884	0.929
|WSS Div.|	R	0.330	0.472	−0.043	−0.059
	P	0.057	**0.001**	0.762	0.767
Div. of Norm. WSS	R	−0.212	0.302	0.001	−0.086
	P	0.229	**0.041**	0.996	0.664
|Div. of Norm. WSS|	R	−0.275	0.198	0.192	−0.296
	P	0.115	0.187	0.178	0.126
NO	R	−0.040	0.710	−0.510	0.357
	P	0.844	$\mathbf{1.080 \times 10^{-6}}$	**0.001**	0.079
LDL	R	0.081	−0.137	0.416	0.210
	P	0.687	0.425	**0.012**	0.315

3.3.2 All patients study

In this section, the statistical analysis for all the patients as one unified dataset is presented. The calculated correlation in the previous section cannot be extended to a population. Thus,

Table 3.9: The correlations between presence of napkin-ring sign (NRS) in the follow-up images and various hemodynamic parameters. Values in bold font indicate statistically significant differences ($P < 0.05$).

Hemodynamic Parameter		P1	P3	P5	P6	P7
WSS	R	0.621	−0.089	−0.200	0.008	0.526
	P	**8.226×10^{-5}**	0.559	0.159	0.969	**0.003**
WSS Div.	R	−0.344	0.582	0.119	0.118	0.406
	P	0.198	0.823	0.423	0.053	0.432
|WSS Div.|	R	0.240	0.602	−0.108	−0.087	0.413
	P	0.434	0.612	0.681	0.616	0.543
Div. of Norm. WSS	R	−0.209	0.368	0.140	−0.096	0.337
	P	0.492	0.092	0.785	0.546	0.607
|Div. of Norm. WSS|	R	−0.114	0.378	0.135	−0.144	0.318
	P	0.705	0.137	0.329	0.264	0.482
NO	R	−0.145	0.490	−0.403	0.205	0.212
	P	0.613	0.780	0.587	0.386	0.847
LDL	R	0.197	−0.053	0.554	0.393	-2.414×10^{-4}
	P	0.904	0.136	0.141	0.749	0.539

the qualitative and quantitative data for all the patients are compared against the corresponding hemodynamic and biotransport data points.

Table 3.10 shows the correlations between qualitative parameters and the hemodynamic/biotransport data. The statistical analysis shows a moderate correlation between positive remodeling and local WSS ($P = 3.5 \times 10^{-9}$ and correlation coefficient of 0.349) and a moderate correlation between positive remodeling and local concentration of NO ($P = 6.6 \times 10^{-11}$ and correlation coefficient of 0.415).

Since the HU values in DICOM series varies between baseline and follow-up images, the calculated volumes for different plaque characteristics varies between these two dataset. To account for this error, a threshold is assumed for all the quantitative parameters. We assumed if the change in a quantity is in the interval of $[-2\%, 2\%]$, the data point can be dismissed. With this assumption, the statistical analysis was performed for the whole dataset for positive and negative changes in the quantitative parameters, Tables 3.12 and 3.11 respectively. It should be noted that for the case of negative changes in Table 3.11, the absolute value of change was considered to analyze the data. According to Table 3.12, the

68

local WSS in the baseline shows negative correlation with percentages of change ($\geq 2\%$) in LAP, FP, and VW while a positive correlation can be seen for the absolute value of change ($\leq -2\%$) in the LAP, FP, and vessel wall volumes.

Table 3.10: The correlations between the changes in qualitative/quantitative plaque characteristics among all the patients (P1-P8) and various hemodynamic parameters. Values in bold font indicate statistically significant differences ($P < 0.05$). † shows the p-value is $< 10^{-16}$.

Hemodynamic Parameter		Lumen	LAP	FP	CP	Vessel wall	PR	NRS	Vessel wall growth
WSS	R	0.089	−0.073	−0.044	0.052	−0.068	0.350	0.115	−0.158
	P	0.147	0.234	0.468	0.398	0.267	**3.504×10^{-9}**	0.059	**0.009**
WSS Div.	R	0.054	0.041	−0.015	0.007	0.056	0.053	−0.014	0.093
	P	0.373	0.505	0.804	0.904	0.363	0.390	0.129	$0^{\dagger}$
|WSS Div.|	R	0.070	−0.151	−0.030	0.074	−0.142	0.119	0.037	−0.097
	P	0.253	**0.014**	0.624	0.227	**0.020**	0.051	0.113	$0^{\dagger}$
Div. of Norm. WSS	R	0.117	0.021	−0.025	0.071	−0.030	0.022	0.087	−0.024
	P	0.055	0.727	0.687	0.246	0.626	0.723	0.697	$0^{\dagger}$
|Div. of Norm. WSS|	R	0.055	0.727	0.687	0.246	0.626	0.723	0.697	0.000
	P	0.657	0.543	0.402	0.780	0.392	0.776	0.547	$0^{\dagger}$
NO	R	0.066	−0.104	−0.009	0.212	−0.031	0.415	0.188	−0.061
	P	0.322	0.119	0.888	**0.001**	0.647	**6.658×10^{-11}**	0.360	$0^{\dagger}$
LDL	R	0.093	−0.048	−0.013	−0.050	−0.003	−0.070	0.001	0.079
	P	0.162	0.475	0.843	0.453	0.968	0.294	0.237	$0^{\dagger}$

Table 3.11: The correlations between the percentage of change ($\leq -2\%$) in quantitative plaque characteristics among all the patients (P1-P8) and various hemodynamic parameters. Values in bold font indicate statistically significant differences ($P < 0.05$).

Hemodynamic Parameter		Lumen	LAP	FP	Vessel wall
WSS	R	0.191	0.478	0.578	0.371
	P	**0.013**	**7.860×10^{-7}**	**9.653×10^{-10}**	**1.204×10^{-4}**
WSS Div.	R	−0.058	−0.198	−0.199	−0.211
	P	0.448	**0.050**	**0.044**	**0.032**
|WSS Div.|	R	0.081	0.364	0.456	0.326
	P	0.293	**2.372×10^{-4}**	**1.703×10^{-6}**	**7.902×10^{-4}**
Div. of Norm. WSS	R	−0.010	0.044	0.038	0.069
	P	0.898	0.664	0.700	0.488
|Div. of Norm. WSS|	R	0.032	0.088	0.103	0.005
	P	0.681	0.386	0.300	0.957
NO	R	−0.032	−0.172	0.016	−0.231
	P	0.698	0.132	0.888	**0.036**
LDL	R	−0.107	−0.029	0.190	0.079
	P	0.195	0.802	0.085	0.478

Table 3.12: The correlations between the percentage of change ($\geq 2\%$) in quantitative plaque characteristics among all the patients (P1-P8) and various hemodynamic parameters. Values in bold font indicate statistically significant differences ($P < 0.05$).

Hemodynamic Parameter		Lumen	LAP	FP	Vessel wall
WSS	R	-0.469	-0.183	-0.294	-0.290
	P	$\mathbf{1.673 \times 10^{-6}}$	**0.018**	$\mathbf{1.677 \times 10^{-4}}$	$\mathbf{1.681 \times 10^{-4}}$
WSS Div.	R	-0.226	-0.182	-0.198	-0.060
	P	**0.026**	**0.019**	**0.012**	0.447
|WSS Div.|	R	0.307	0.102	0.231	0.196
	P	**0.002**	0.191	**0.003**	**0.012**
Div. of Norm. WSS	R	0.081	0.042	-0.034	0.022
	P	0.429	0.589	0.670	0.780
|Div. of Norm. WSS|	R	0.132	0.020	0.063	0.123
	P	0.197	0.796	0.428	0.117
NO	R	-0.141	-0.068	-0.072	-0.014
	P	0.221	0.416	0.402	0.871
LDL	R	0.001	-0.170	0.014	-0.086
	P	0.990	**0.041**	0.873	0.303

3.4   Discussion

We investigated the relation between longitudinal changes in multiple quantitative and qualitative vulnerable plaque characteristics and the hemodynamics and biotransport features at the baseline. An in-house software was developed to accurately quantify the plaque characteristics and register them with the 3D hemodynamic and biotransport results. The developed software uses various algorithms to ensure high accuracy of plaque quantification such as active contour segmentation, vessel enhancement filter, and adaptive threshold quantification. The use of vessel enhancement filter ensures reduction in the organ over-projection and thus improves the accuracy of the quantitative measurement of arterial morphology. The main innovations of present study are consideration of computational biotransport data and the simultaneous utilization of vessel enhancement filter, active contour levelset algorithm, and adaptive threshold quantification.

The association between low WSS magnitude and increased inflammation has been previously reported in the literature [159, 160, 161, 162, 163, 164, 165, 166, 167]. These studies

support the hypothesis that hemodynamic parameters might play an important role in the atherosclerotic plaque growth. Among all the hemodynamic parameters considered in this study, the WSS, absolute WSS divergence, and local concentration of NO showed the best correlations with different vulnerable plaque characteristics. Despite the small number of patients considered in this study, the segment-specific assessment design provided association between local hemodynamics and biotransport data and the CTA-derived vulnerable plaque features.

The patient-by-patient study of the relation between hemodynamics and longitudinal changes in the plaque content shows interesting results. For example in the case of longitudinal changes in LAP volume, 5 out of 8 patients showed a significantly meaningful association between magnitude of WSS in the baseline and the changes in the LAP volume. According to Table 3.3, a maximum Spearman's rank correlation coefficient of -0.408 was obtained. However, if the longitudinal changes in LAP was compared against the baseline WSS magnitude for all the patients collectively, our results do not show any significant association between longitudinal changes in LAP and the hemodynamic parameters. Figure 3.11 shows the corresponding scatter plot for both longitudinal changes and percentage of change in LAP versus the considered hemodynamic parameters. As it can be seen in this figure, the percentage of changes in LAP volume versus hemodynamic and biotransport data are concentrated around 0.0%. The image registration for baseline and follow-up and the difference between the HU values in baseline and follow-up images might cause these small changes in the plaque content volumes. If we only consider the longitudinal changes greater than 2% in our dataset to filter out the inaccuracies mentioned above, the association between LAP volume changes and WSS becomes more significant (p-value < 0.05). On the other hand if we consider only the negative changes in the LAP volume, i.e. the LAP volume shrinks more than 2% from baseline to follow-up, a positive correlation coefficient of 0.478 is obtained. This shows the LAP volume decreases with the increase in the baseline WSS magnitude. The high WSS magnitude has been hypothesized to induce an atheroprotective response in the

71

endothelial cells (ECs). Physiological and high WSS values stimulate endothelial nitric oxide synthase (eNOS) phosphorylation and shear stress dependent Ca^{2+} channels [82]. This leads to subsequent NO production and flow-induced vasodilation, which protect against atherosclerosis.

The WSS divergence can be used as an indicator of local endothelium contraction and expansion. Positive values of WSS divergence show expansion while negative values show contraction of ECs. Except in one patient (P7), no significant association between quantitative atherosclerotic plaque markers and the derivatives of WSS divergence including absolute value of WSS divergence, divergence of normalized WSS, and absolute value of divergence of normalized WSS was found. The segment-specific assessment of P7 reveals moderate-to-strong correlation between WSS divergence/absolute WSS divergence and the longitudinal changes in LAP volume and CP volume. The |WSS Div.| showed a moderate positive correlation with the reduction of LAP volume from baseline to follow-up when analyzing all the patients, collectively. The scatter plots for longitudinal changes and percentage of change in FP volume versus various hemodynamic parameters are shown in Fig. 3.12.

Previous studies have demonstrated an increased risk of acute coronary syndrome (ACS) in patients with a larger volume of non-calcified and low-attenuation plaque. The fibrous plaques (FP) fall into the category of non-calcified plaques. The patient-by-patient study showed a moderate correlation between the growth of FP and WSS magnitude in patients P1, P3, P7, and P8. However, considering a longitudinal decrease in FP volume greater than 2% shows a moderate-to-strong correlation with the WSS magnitude. That is, the increase in WSS magnitude in baseline resulted in a decrease in the volume of FP plaque in the follow-up. Also, our statistical assessment showed a meaningful association between the absolute value of WSS divergence and the decrease in the FP volume (Table 3.11). On the other hand, Table 3.12 shows a moderate negative correlation between the longitudinal changes in FP volume and the WSS magnitude.

72

Figure 3.11: The scatter plots for longitudinal changes in the LAP volume *vs.* various hemodynamic parameters. The square marker shows the percentage of change while the asterisks show the longitudinal changes in the volume of LAP.
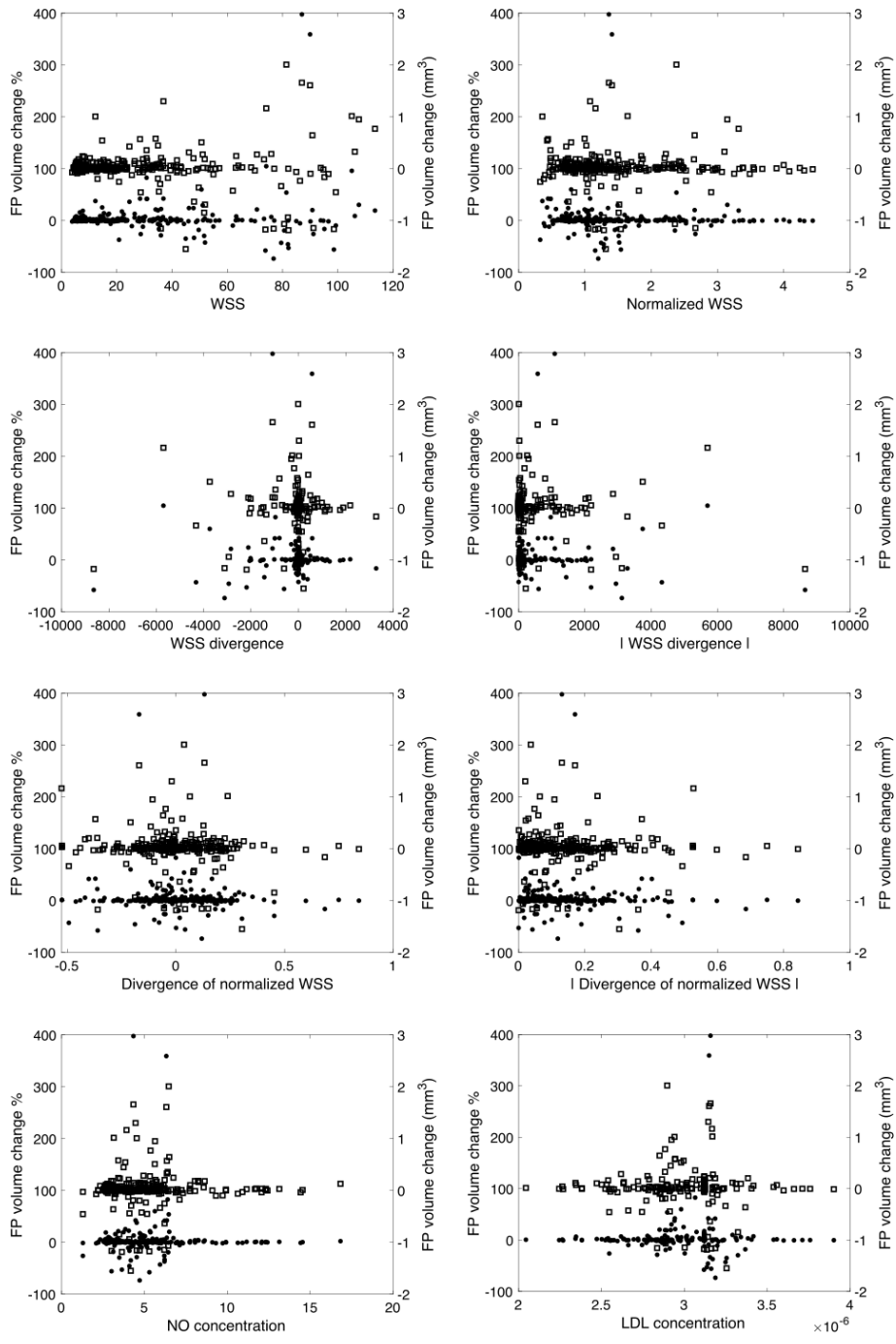
Figure 3.12: The scatter plots for longitudinal changes in the fibrous plaque volume *vs.* various hemodynamic parameters. The square marker shows the percentage of change while the asterisks show the longitudinal changes in the volume of FP.

If we consider the longitudinal changes in the vessel wall, a weak negative association between WSS magnitude and the changes in vessel wall can be seen. However, according to Table 3.12, the longitudinal changes in the vessel wall is moderately correlated with the WSS magnitude. This association has a negative correlation coefficient which indicates that low WSS magnitude in baseline results in an increase in the vessel wall volume at the follow-up. On the other hand, our statistical analysis showed that the decrease in the vessel wall volume has a positive correlation with the WSS magnitude, which emphasizes the atheroprotective role of high wall shear stress in atherosclerosis. Figure 3.13 shows the scatter plot of longitudinal changes and percentage of change in vessel wall volume versus various hemodynamic parameters.

As mentioned in section 3.1, positive remodeling and presence of napkin-ring sign are markers of vulnerable plaques. In this study the positive remodeling and NRS were assessed using a binary approach. Only four out of 8 patients showed positive remodeling in their left anterior descending and left circumflex arteries. The segment-specific study showed a moderate positive correlation between presence of positive remodeling in follow-up and the WSS magnitude and the local concentration of NO. The presence of NRS in the follow-up did not show any meaningful correlation with the considered hemodynamic and biotransport parameters at baseline.

Our results show the role of hemodynamics in progression and prevention of atherosclerotic plaques. Specifically, the segment-specific assessment of the data shows that WSS magnitude can be considered as a local indicator for the growth/shrink of different atherosclerosis plaque components as well as the vessel wall in general. In Chapter 2, we showed that the both atherogenic and atheroprotective biochemicals localize in regions downstream to a plaque where WSS magnitude is low and we stated that it is not clear how the combination of these competing effects play out in the process of atherosclerosis. The statistical analysis shows that in all patients, collectively, there is no meaningful association between the local
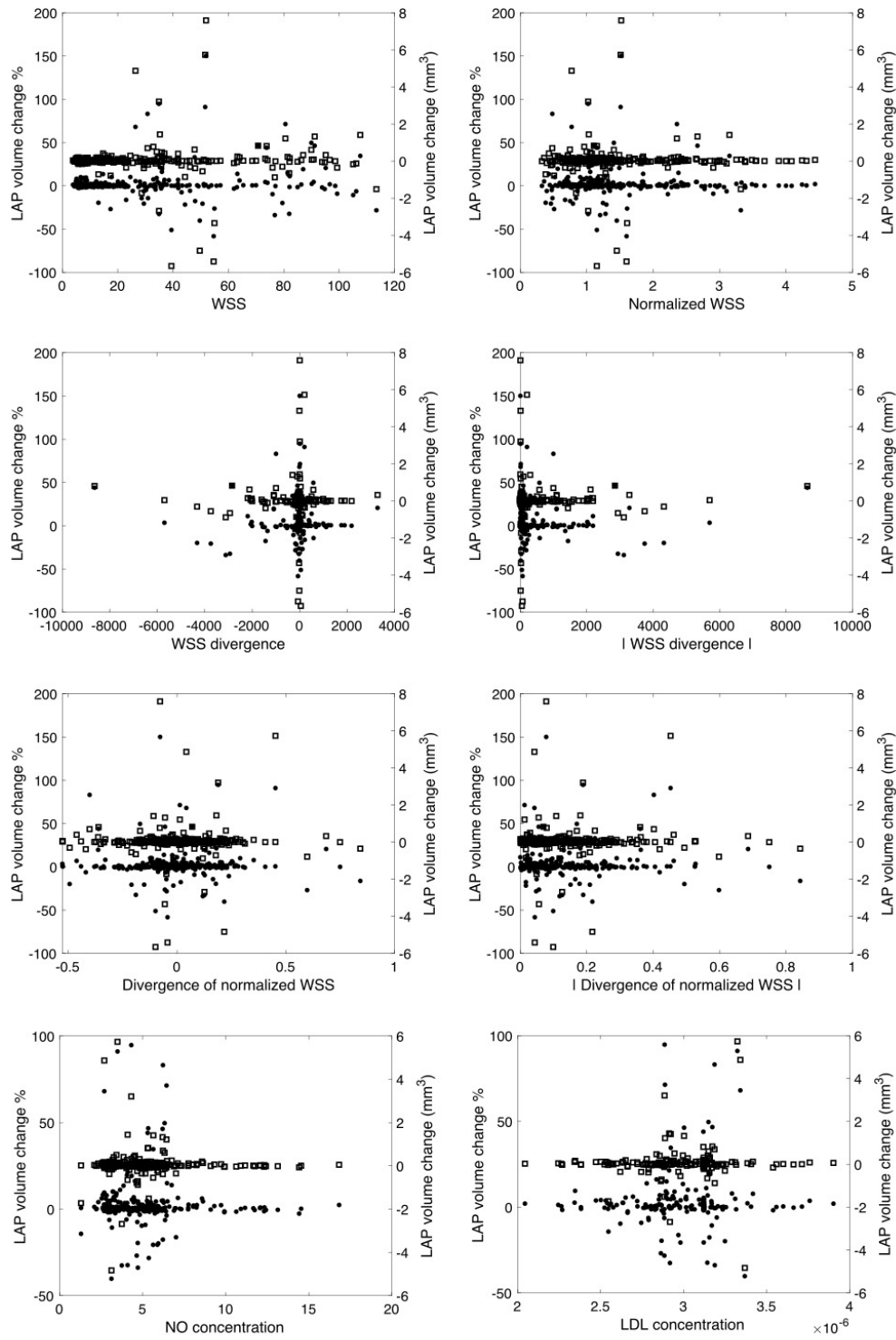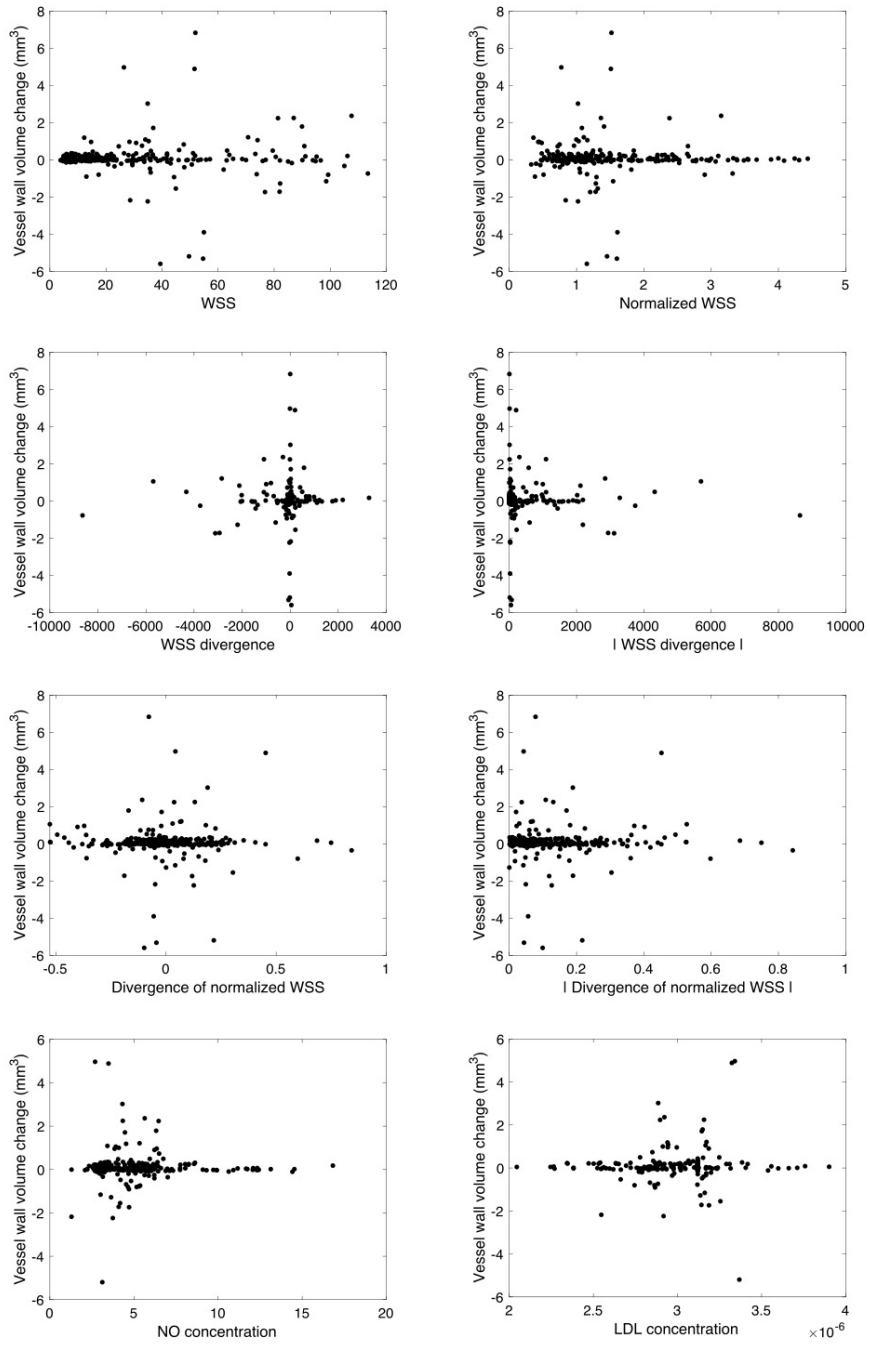
Figure 3.13: The scatter plots for longitudinal changes in the vessel wall volume *vs.* various hemodynamic parameters. The square marker shows the percentage of change while the asterisks show the longitudinal changes in the volume of the arterial wall.

concentration of NO and LDL and the longitudinal changes in the atherosclerotic plaque features. However, the WSS magnitude and weakly the WSS divergence show meaningful correlation with the changes in the LAP, FP and vessel wall volumes.

There are some potential limitations that can affect the accuracy of our results. First, the small sample size and short-term follow-up study did not have enough power to demonstrate the significant differences in the calcified plaque, positive remodeling, and presence of napkin-ring sign. Second, the derived hemodynamic and biotransport parameters were obtained under the assumption that the inflow boundary conditions was based on the general coronary artery waveforms with parabolic profiles. Third, the generated segments for baseline and follow-up images might not match perfectly and also the HU ranges for different plaque composition in these two dataset are different. This can lead to minor inaccuracies when analyzing the data. Fourth, obtaining a p-value < 0.05 does not indicate a significant association in reality. p-value is considered as a rough guide of the strength of evidence against the null hypothesis. In other words, the meaning of p-value < 0.05 is merely that one should repeat the experiment. If subsequent studies also yield significant p-values, one could conclude that the observed effects were unlikely to be solely the result of chance. Thus, independent tests are needed to ensure that the observed associations in this study are not based on the chance alone [158].

Chapter 4

Implementing a coupled 3D-1D blood flow solver in Simvascular

4.1 Introduction

Computational fluid dynamics (CFD) has been shown to be a powerful and effective tool to model the blood flow and study the hemodynamic in arterial network. The cardiovascular system can be considered as a multiscale system which each scale has different physiological and functional behavior. The interaction between blood and the vessel wall propagates pressure waves from the heart to the distal arteries. These waves play an important role in regulating the blood pressure in the cardiovascular system. CFD can be used to simulate the blood dynamics by solving the Navier-Stokes equations inside this multiscale system. However, the 3D simulation of this system is computationally expensive. To resolve this issue, 1D models can be used to model the dense arterial network with much lower computational cost. Recently, the approach of 1D-3D coupled models of cardiovascular system has gained popularity since they can simulate an accurate pressure wave in smaller arteries while show

the blood flow structures in the larger vessels.

The 1D models, originally introduced by Euler [168], are a valid alternative to describe the arterial network [169, 170]. Assuming a cylindrical geometry for arteries, one can reduce the space-dependence to the axial direction of the cylinder and create a 1D model. The 1D models allow to obtain the large scale characteristics including the pressure drop, pressure waves, and flow rates at different part of the arterial tree. The elasticity of the vessel wall and peripheral resistance and capacitance are also can be included in 1D models [20, 22, 23, 21]. Several studies confirmed the successful simulation of large-scale features such as pressure and flow waves in various arteries using nonlinear 1D models [171, 172, 173, 174]. However, there are major challenges with specifying the input parameters of the 1D model from clinical data [175]. Recently, the number of 1D arterial segments used in modeling the arterial network has increased to over 4 million [176, 177, 21, 178].

On the other hand, the patient-specific 3D high-resolution models are well suited for studying the effects of geometry on the blood flow [18, 19, 179, 180] as well as the local impact of blood flow structures on the transport of various biochemicals and cells [181]. However, the use of high resolution 3D models for simulation of blood flow inside an arterial network with large number of arteries is impractical. The high computational cost restricts their application to only arterial trees with limited number of bifurcations [182, 183, 184, 185].

The geometrical multiscale approach of coupled 1D-3D models can address the aforementioned limitations when simulating a large network of arteries [23, 20]. This approach significantly decreases the computational cost while using a high resolution 3D model for a specific arterial district [186]. In other words, the main advantage of 1D-3D approach is to provide detailed hemodynamic features locally while accounting for the global circulation. Previous studies have explored the 1D-3D approach to simulate the carotid arteries [187], cerebral aneurysms [188], and abdominal aorta [189]. Considering the potentials of hybrid 1D-3D models, no open-source software provides such a tool for the researchers. One of the

most used open-source software to simulate the patient-specific blood flow in cardiovascular system is *Simvascular* [190]. This software also offers a stand-alone 1D solver. However, the coupling between 1D and 3D solvers is not provided by the software. Here, we propose a framework to couple these two stand-alone solvers and provide a computationally feasible alternative for modeling a large network of arteries. In this chapter we focus on the mathematical formulation of a 3D-1D solver and present the validation results.

4.2 Methods

In this section, the governing equations for the flow of a Newtonian, incompressible fluid inside a deformable one-dimensional vessel are presented. Then, the algorithm to couple the 1D and 3D solvers in *simvascular* is discussed.

4.2.1 Governing equations

In 1D formulation, each segment is treated as a deformable cylindrical vessel with a specific length, initial and final cross-sectional diameters. It is assumed that the properties of the vessel can be described by a single axis, i.e. the centerline. Such a geometry can be obtained from a patient-specific 3D model by extracting the centerline and storing the coordinates of each end of a segment, corresponding segment length, and the initial and final diameters of the corresponding segment.

The governing equations for the 1D flow inside a deformable vessel include continuity, momentum, and constitutive equations. It should be noted that these equations are along a single axis z. The continuity and momentum equations can be written as

$$\frac{\partial S}{\partial t} + \frac{\partial Q}{\partial z} = 0 \ , \tag{4.1a}$$

$$\frac{\partial Q}{\partial t} + \frac{\partial}{\partial z}\left[(1+\delta)\frac{Q^2}{S}\right] + \frac{S}{\rho}\frac{\partial p}{\partial z} = N\frac{Q}{S} + \nu\frac{\partial^2 Q}{\partial z^2} \ , \tag{4.1b}$$

where $S(t,z)$ is the cross-sectional area, $Q(t,z)$ flow rate, $p(t,z)$ pressure, ρ density, and ν is the kinematic viscosity. Assuming a parabolic velocity profile, the N and δ can be defined as

$$\delta = \frac{1}{3} \ , \quad N = -8\pi\nu \ , \tag{4.2a}$$

Since an elastic model is utilized, the constitutive equation has the following form

$$\tilde{p}(S,z) = p^0(z) + \frac{4}{3}\frac{E\,h}{r^0(z)}\left(1 - \sqrt{\frac{S^0(z)}{S(z,t)}}\right) \ , \tag{4.3}$$

where E is the Young's modulus and h is the wall thickness. $r^0(z)$ is the initial radius of the segment along the axis, $p^0(z)$ is the initial pressure, and $S^0(z)$ is the prescribed initial area. We can define the $\frac{E\,h}{r^0(z)}$ to consider a linear or nonlinear material as

$$\frac{E\,h}{r^0(z)} = k_1\,\exp k_2\,r^0(z) + k_3 \ , \tag{4.4}$$

where k_1, k_2, and k_3 are empirical parameters. One can rewrite Eqs. 4.6 and 4.3 in a quasi-conservative form:

$$\frac{\partial \mathbf{U}}{\partial t} + \frac{\partial \mathbf{F}}{\partial z} - \mathbf{K}\frac{\partial^2 \mathbf{U}}{\partial z^2} = G, \text{ or } \quad \frac{\partial \mathbf{U}}{\partial t} + \frac{\partial \mathbf{F}}{\partial z} - \mathbf{K}\frac{\partial^2 \mathbf{U}}{\partial z^2} = \mathbf{C}_F\,\mathbf{U} \ , \tag{4.5}$$

81

where

$$\mathbf{U} = \begin{bmatrix} U_1 \\ U_2 \end{bmatrix} = \begin{bmatrix} S \\ Q \end{bmatrix} , \tag{4.6a}$$

$$\mathbf{F} = \begin{bmatrix} U_2 \\ (1+\delta)\frac{U_2^2}{U_1} + \frac{1}{\rho} \int_{p0}^{p(z,t)} \tilde{S}(p,z,t)\,dp \end{bmatrix} , \quad \mathbf{K} = \begin{bmatrix} 0 & 0 \\ 0 & \nu \end{bmatrix} , \tag{4.6b}$$

$$\mathbf{G} = \begin{bmatrix} 0 \\ N\frac{U_2}{U_1} + \int_{p0}^{p} \frac{1}{\rho} \frac{\partial \tilde{S}(p,z,t)}{\partial z}\,dp \end{bmatrix} , \quad , \tag{4.6c}$$

$$\mathbf{C}_F = \begin{bmatrix} 0 & 0 \\ \frac{1}{U_1} \int_{p0}^{p} \frac{1}{\rho} \frac{\partial \tilde{S}(p,z,t)}{\partial z}\,dp & \frac{N}{U_1} \end{bmatrix} , \tag{4.6d}$$

Now, the weak form can be written as follows

$$\int_0^t \int_\Omega \left(-\mathbf{W}_{,t}^T\,\mathbf{U} - \mathbf{W}_{,z}^T\,\mathbf{F} + \mathbf{W}_{,z}^T\,\mathbf{K}\,\mathbf{U}_{,z} - \mathbf{W}^T\,\mathbf{G} \right)\,d\Omega\,dt + \int_0^T \left[\mathbf{W}^T \left(\mathbf{F} - \mathbf{K}\mathbf{U}_{,z} \right) \right]_0^L\,dt +$$

$$\int_\Omega \mathbf{W}^T(z,T)\mathbf{U}(z,T)\,d\Omega -$$

$$\int_\Omega \mathbf{W}^T(z,0)\,\mathbf{U}^0(z)\,d\Omega = 0 \tag{4.7a}$$

where $\Omega = [0,L]$ is the test function space and $\mathbf{W} = [W_1\,W_2]^T$ is the trial function space. $\mathbf{U}^0(z) = [S^0(z), Q^0(z)]^T$ is the initial condition. To specify the boundary conditions, one can use a disjoint decomposition and Dirichlet-to-Neumann methods to incorporate the boundary conditions into the weak form. For the detailed formulation on applying various types of boundary conditions see [191, 192].

4.2.2 1D-3D coupling algorithm

The 1D and 3D solvers in *Simvascular* are stand-alone packages. Thus, one cannot use the software to simulate the blood flow in a hybrid 1D-3D model. However, if we consider the 1D solver as a boundary condition in which there exists a continuity of mass and normal total pressure at the coupling interface, we can implement the coupled 1D-3D solver in *Simvascular*. The continuity of mass and normal total pressure can be written as:

$$\sigma^{tot}(\mathbf{u}_{3D}, p_{3D}) \cdot \mathbf{n} = p_{1D} \, \mathbf{n} \, , \tag{4.8a}$$

$$Q_{3D} = Q_{1D} \, , \tag{4.8b}$$

For a rigid 3D model, we can simplify Eqs. 4.8 as

$$p_{1D} = \frac{1}{|\Gamma|} \int_{\Gamma} p_{3D} d\gamma \, , \tag{4.9a}$$

$$Q_{1D} = -\rho \int_{\Gamma} \mathbf{u}_{3D} \cdot \mathbf{n} d\gamma \, , \tag{4.9b}$$

where $|\Gamma|$ is the area of the interface Γ. The negative sign in the continuity of mass equation of 4.8 indicates that Q_{1D} and $\mathbf{u}_{3D} \cdot \mathbf{n}$ are pointing inwards and outwards from the 1D and 3D domains, respectively.

To ensure the interface boundary holds the continuity conditions in Eq. 4.8 between times t^n and t^{n+1}, the numerical solution should be split into an iterative sequence of dimensionally homogeneous problems, that is 1D and 3D solution. The interface boundary in the 3D model can be treated as Neumann boundary condition while the interface node on the 1D model can be specified as a Dirichlet boundary condition. At each time-step, an inner iterative algorithm can be used to obtain the continuity conditions at the coupling interface. The steps in the iterative algorithm are as follows:

Initialization:

- Apply the initial conditions to both 3D and 1D models;

- Set $k = 0$;

- $\mathbf{u}_{3D,0}^{n+1} = \mathbf{u}_{3D,0}^{n}, \quad p_{3D,0}^{n+1} = p_{3D,0}^{n}, \quad p_{1D,0}^{n+1} = p_{1D,0}^{n}, \quad Q_{1D,0}^{n+1} = Q_{1D,0}^{n}$

Loop over k:

- Solve 3D model with the following boundary condition on the coupling interface:

  $p_{3D,k+1}^{n+1} = \alpha p_{1D,k}^{n+1} + (1 - \alpha) p_{3D,k}^{n+1}$; where α is a relaxation factor

- Solve 1D model with the following boundary condition at the coupling node:

  $Q_{1D,k+1}^{n+1} = Q_{3D,k+1}^{n+1}$;

- $k = k + 1$;

- Set a convergence criteria for the continuity on the interface: $|p_{3D,k+1}^{n+1} - p_{1D,k+1}^{n+1}| < \varepsilon$

  where ε is the convergence tolerance.

4.2.3   Simvascular 1D-3D coupling implementation

As mentioned before, the 1D and 3D solvers in *Simvascular* are stand-alone packages. However, treating the 1D solver as a boundary condition for 3D solver is a way to couple these packages. To do so, we used the General Boundary Condition (GenBC) in *Simvascular*. GenBC provides a framework to define custom inflow or outlet boundary conditions. The main application of GenBC is to create an arbitrary lumped parameter network (LPN) layout. The GenBC framework is implemented as a Fortran program called by the *SimVascular* flow solver 'svSolver'. Users can define an arbitrary set of differential equations for their application and implement them in Fortran inside the GenBC program. The Fortan program is then compiled to produce a GenBC executable program. This executable is called by

svSolver during execution to provide values for custom boundary conditions. To setup the GenBC in *Simvascular*, one can refer to [193].

The 1D solver in *Simvascular* software is written in C++ language. This package reads an input file containing the coordinates of nodes, information about the joints, segment information, material parameters, and solver parameters. The 1D solver package can return the element-based results of the whole geometry in the text format or .VTK format. Also, this package only considers an all-zero initial condition for the flow rate and pressure inside the 1D domain. The all-zero initialization of the domain makes it impossible to couple the 1D solver with the 3D solver. On the other hand, because the GenBC program and 1D solver are written in different programing languages, a link should be created between these two packages. Another limitation of using GenBC is that the user cannot use discrete data as the inflow boundary condition to the 3D geometry. In the rest of this section, we present how one can implement a hybrid 1D-3D solver in the *Simvascular* software with embedded arbitrary inflow boundary condition.

Implementing GenBC program. As it was mentioned previously, GenBC provides a programing framework to define custom boundary conditions in *Simvascular* in Fortran language. Using GenBC, users do not have access to change the global parameters in the 3D solver. The coupling algorithm needs each 3D time-step to be repeated until the convergence criteria for coupled interface is met (Eq. 4.9). However, according to the *Simvascular*'s source code, the GenBC can read the stage in which the 3D solver is performing the computations. There are 4 different stages in each 3D time-step: initialization with flag 'I', calculating the derivatives 'D', Navier-Stokes solver stage 'T', final stage of computation 'L'. Among all these stages, the user can control the number of iterations in stage 'T' by changing the *Step Construction* in the software. We used this flag in the GenBC program to implement the hybrid 1D-3D solver and iteratively correct the interface boundary condition.

To be able to transfer data between the GenBC and the 1D solver, we created six different

Table 4.1: The name and description of generated files for transferring information between GenBC and the 1D solver.

File name	Description
OutletID.dat	In case the 3D geometry is consisted of multiple outlet surfaces, this file stores the ID of an outlet and pass it on to the 1D solver. 1D solver reads this file and executes the corresponding 1D simulation.
OneDinit.dat	This file stores a boolean variable indicating the need to store the data in the 1D model in a format that it can be read as initial condition for the next 1D simulation. When the iterative algorithm on the interface converges, the 1D data will be store.
OneDinletQ_xxxxx.dat	This file stores the flow rate value at each outlet in the 3D geometry. 'x' shows the outlet ID. 1D solver reads this file and applies the inflow accordingly.
OneDinletP_xxxxx.dat	This file stores the inlet pressure of the 1D model. GenBC reads this value in the iterative algorithm to ensure the continuity at the interface.
interfaceConv	This file stores the data related to the convergence of the iterative method at each 1D-3D interface. If all the interfaces met the continuity criteria, the stored value in this file will be '0'.
PreviousSolution.dat	This file contains the 1D solution data in a format that can be used as initial condition for the 1D solver.

files to store various information. The information related to these files are presented in Table 4.1. Since the 1D solver is in a different programing language than the GenBC program, The 1D solver is modified in a way that can be called directly from the Fortran code. The Fortran code snippet related to calling the 1D solver is shown in Code 4.1. In this code snippet, nNeumannSrfs is the total number of 3D outlets and line 13 calls the executable 1D solver.

Code 4.1: Code snippet for calling the executable 1D solver from GenBC.

```
1   c  Calculate  boundary  conditions
2          fmt  =  '(I5.5)'
3         DO  i=1,  nNeumannSrfs
4            WRITE(fileCounter,fmt)  i
5            INQUIRE  (FILE='OneDinletP_'//TRIM(fileCounter)//'.dat',
6        2      EXIST=ierr)
7
```

```
 8 |            OPEN(1, FILE='OutletID.dat', STATUS='UNKNOWN')
 9 |            WRITE(1, '(I5)') i
10 |            CLOSE(1)
11 |
12 |            IF (t .GE. tFinal .AND. flag .EQ. 'T') THEN
13 |                CALL system('./OneDSolver ./'//'OneDinpotFile_'
14 |      2      //TRIM(fileCounter)//'.in'//' > OneDOutput.dat')
15 |
16 |                OPEN (1, FILE = 'OneDinletP_'//TRIM(fileCounter)//'.dat',
17 |      2        STATUS='OLD')
18 |                READ (1, *) R(i)
19 |                CLOSE(1)
20 |            ELSEIF (t .LT. tFinal) THEN
21 |                R(i) = 0D0
22 |            ELSEIF (ierr) THEN
23 |                OPEN (1, FILE = 'OneDinletP_'//TRIM(fileCounter)//'.dat',
24 |      2        STATUS='OLD')
25 |                READ (1, *) R(i)
26 |                CLOSE(1)
27 |            ELSE
28 |                PRINT *, "SMT WRONG WITH ONEDinletP.dat"
29 |                STOP
30 |            END IF
31 |          END DO
```

Modifying the 1D solver. The *Simvascular*'s 1D solver is written in C++ language. The software reads an input file containing the necessary geometrical information, boundary conditions, material properties, and solver parameters. The original solver can read one or multiple input files and solve the Newtonian, incompressible blood flow in deformable 1D vessels. As mentioned earlier, the GenBC in the 3D solver was used as a gateway to transfer information between the 3D and 1D solvers. The modified 1D solver has the ability to read

the generated files in GenBC (Table 4.1), modify the input data, and return the desired pressure values. Since the 1D solver is executed multiple times in each 3D time-step, we added the arbitrary initial condition to the solver. The original package considers an all-zero initial condition for all variable inside the domain.

4.3   Results and validation

In this section, the results of developed 1D-3D solver are presented and validated against data extracted from the literature. The first step in developing the 1D-3D solver was to modify the *Simvascular*'s 1D solver and add arbitrary initial condition to the solver. This was done by extracting the 1D variables and storing them in a way that can be read by the 1D solver. The test case used for validation of this step was the 1D abdominal aorta model with iliac bifurcation [194]. Figure 4.1 shows the flow rate waveform and changes in the area of the mid-aorta. To verify the developed initialization algorithm, the inflow waveform was divided into 10 parts, each $0.1\,s$. The first simulation was carried out for $0.1\,s$ with zero initial values for the flow rate and reference pressure of $10\,kPa$. The final time-step of this simulation was used to simulate the next part. In total, ten simulations were performed and the final results were compared against the simulation of the whole inflow waveform at once. As it can be seen in Fig. 4.1, the 1D solver initialization algorithm generated accurate results.

The next step in verification of the developed hybrid 1D-3D solver is to look at the interface between 1D and 3D geometries and ensure the continuity of the flow and pressure at this boundary. Figure 4.2 shows the patient-specific 3D geometry, 1D model, and the hybrid 1D-3D geometry. A flow waveform in the shape of sine function was prescribed at the inlet of the geometry. Figure 4.3 shows the flow and pressure waveforms at the hybrid interface of 1D-3D geometry. As it can be seen, the continuity of flow and pressure at the interface can
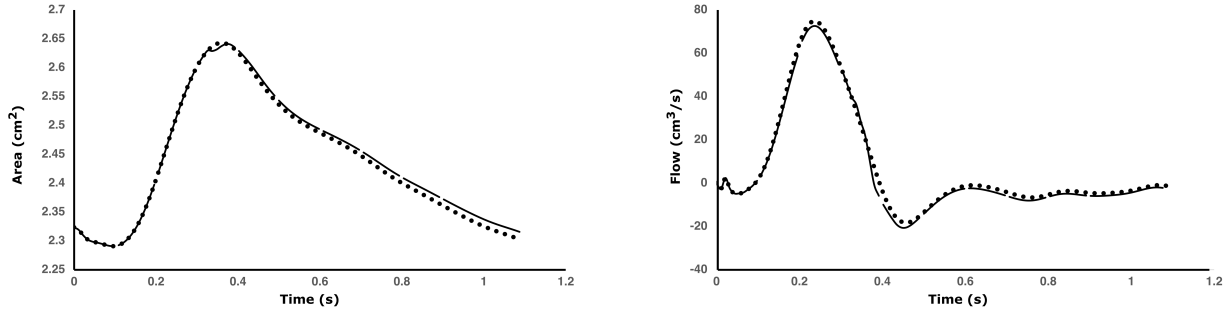
Figure 4.1: Flow wave form and the changes in the area in the 1D model of abdominal aorta. The dotted curve show the simulation results carried out for the total inflow waveform time. The sold line shows the same results while the inflow waveform was divided into 10 sections.

be verified. Since the flow at the 3D interface is outwards and the flow at the 1D interface is inward, the absolute values of flow rate is reported in Fig. 4.3.
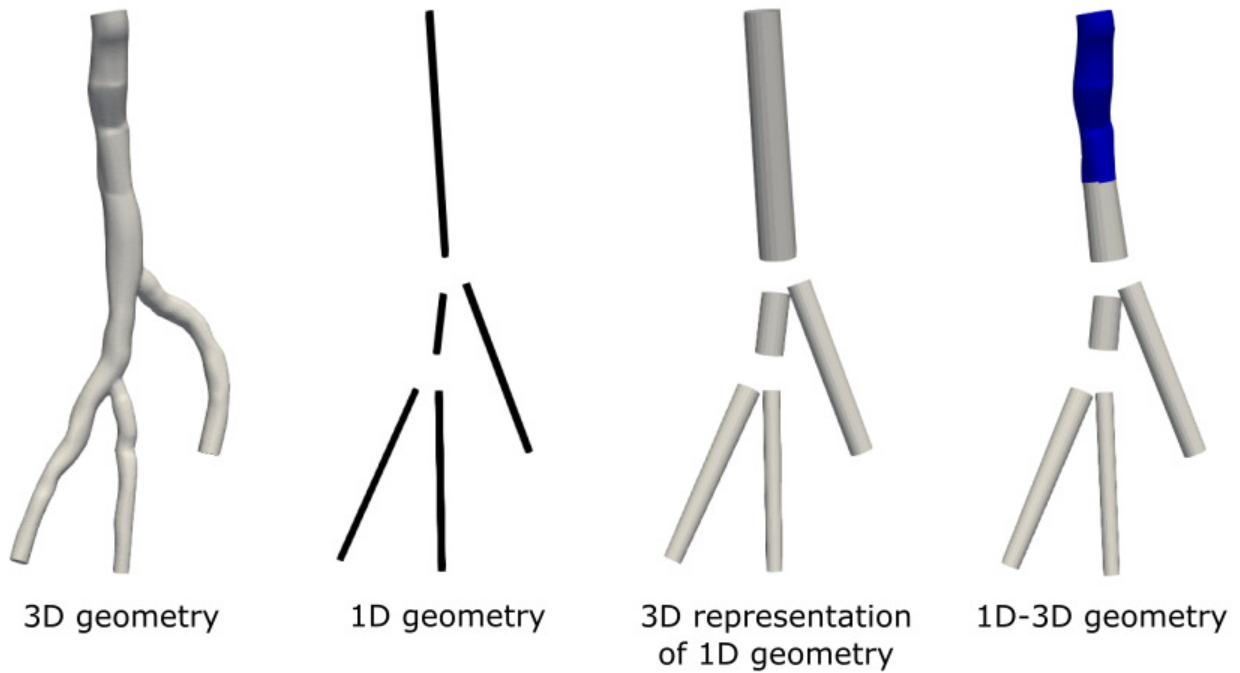
Figure 4.2: The geometries used in verification of continuity condition at the interface of 1D and 3D models.

The next step in verification of the developed 1D-3D solver is to compare the results of current solver with the presented data in the literature. Figure 4.4 shows the resulted pressure waveforms from a 3D simulation with deformable wall [194], the corresponding 1D model, and the pressure waveform obtained from the developed 1D-3D solver. The results are presented for the abdominal aorta inlet and a mid-point in the iliac artery. As it can be
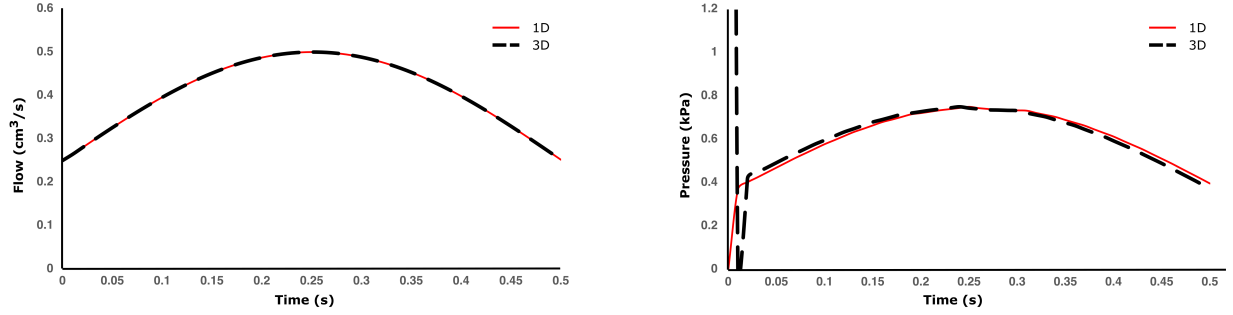
Figure 4.3: The pressure and flow waveforms at the interface of 1D and 3D model. This figures verifies that continuity of the results at the interface for a transient simulation.

seen there is a good agreement between the 1D-3D model and the 3D model with deformable wall.
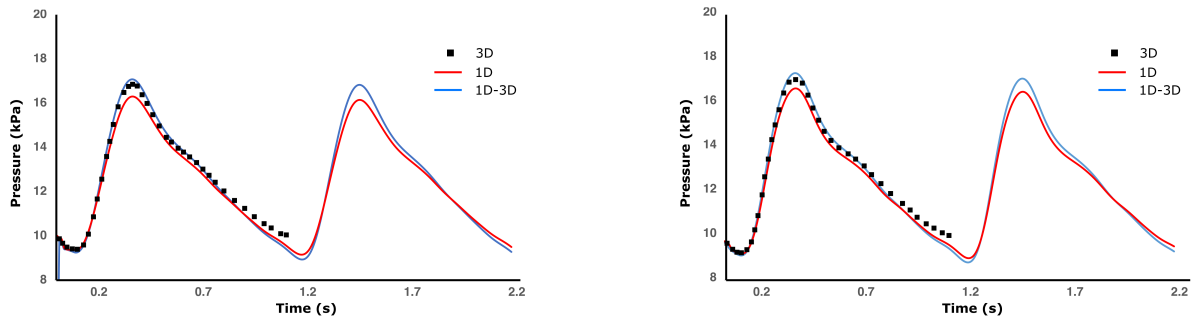
Figure 4.4: Comparison of the resulted pressure waveforms obtained from 3D model with deformable wall, 1D solver, and the developed 1D-3D solver. The figure on the left panel shows the pressure waveforms at the inlet of geometry. The fight panel shows the pressure waveforms in the mid-section of the iliac artery.

The geometries considered for validation of developed hybrid 1D-3D solver were limited to ones with only one hybrid interface. The developed 1D-3D solver also is able to solve multiple hybrid interfaces in one geometry. However, the computational cost increases with having multiple hybrid interfaces since for each interface, the continuity of flow and pressure should be obtained and the changes in the 3D boundary condition may lead do back flow rate in one of the outlets. One of the solutions to resolve the back flow at the interface boundaries is to extend the outlets to ensure the flow can reach a unidirectional state. For this reason, the majority of the 1D-3D simulations in the literature only consider one hybrid outlet [194, 188, 189, 186].

Chapter 5

Automatic generation of vascular network based on perfusion maps: A theoretical study

5.1 introduction

Vascular networks carry on the important task of efficiently distributing the blood to various segments of a tissue. Computational models have been developed to study the blood flow inside an arterial network and understand the connection between vascular structure and the blood supply in biological tissues [195, 196, 197]. Detailed anatomical models of vascular trees can serve as models enabling quantitative analysis of blood flow distribution [198, 199]. Vascular models should match physiological and anatomical structure of organs. In the past decade, advances in the medical imaging techniques provided a great opportunity to reconstruct the larger arteries [200, 181]. However, The resolution of such images does not allow for a detailed reconstruction of the entire vascular network. Thus, developing an

algorithm to automatically generate the arterial network based on physiological principles is needed to better understand the effect of vascular network structure on the supply of blood to various tissues.

Most of the vascular tree network generation algorithms are derived from anatomical data. Kassab *et al.* developed an algorithm based on ordering and connectivity matrix to generate the vascular network in porcine hearts [201]. Based on their work, others enhanced the algorithm by adding functional principles to the model [202, 203]. One common assumption in the early work was the consideration of an evenly distributed blood flow in terminal arteries. More advanced models were introduced by considering a random generation of network based on the perfusion maps [204, 205, 206, 207]. In these methods, the arterial network volume is optimized iteratively until all the terminal segments are added. Also, there are approaches based on the Monte Carlo recursive algorithm that put constraints on the bifurcation angles and the length of the arteries [203].

Recently, the Constraint Constructive Optimization (CCO) method gained popularity for generation of an arterial network [24, 25, 208]. This algorithm is based on the physiological and hemodynamics principles. One advantage of this method is its conforming capabilities to various surfaces. This algorithm includes genesis of a single arterial network which has an optimal volume [209, 210].

In this chapter, we describe details of the physics-based vascular network generation model. We describe the vasculature generation algorithm based on CCO which is initialized with a user-defined perfusion map. We then describe the iterative construction algorithm of a network for random terminal nodes, optimizing the location of bifurcations, calculating branch radii and flow, and the underlying physiological constraints.

5.2 Methods

In this section, we discuss the physics-based mathematical framework to automatically generate a vascular network. In details, the steps to generate an optimal arterial network using the constraints such as the perfusion flow, radius of each vessel, position of each bifurcation, pressure drop and resistances inside the arterial network are presented.

Here, we assume the perfusion point (the starting node of the root segment) is known and fixed in space. Then, the arterial network generation begins with adding the first random terminal node and creating the root segment. Next, the iterative generation of new terminal nodes can be started. After adding each terminal node, an optimized bifurcation will be calculated based on the physiological and geometrical constraints. It is assumed that each new segment initially connects the newly added node to the middle of a candidate segment.

5.2.1 Fundamentals of arterial network generation

The first and most important physical law in an arterial network is the conservation of mass at each bifurcation. In other words, assuming an incompressible blood flow, the volumetric flow rate in the parent artery should be equal to the sum volumetric flow rates in the daughter branches, Q_{d1} and Q_{d2}:

$$Q_{parent} = Q_{d1} + Q_{d2} \, , \tag{5.1}$$

Assuming all the terminal vessels have the same volumetric flow, we can extend Eq. 5.1 to the whole arterial network and show that the sum of all the terminal flows needs to be equal to the perfusion flow, Q_{perf}

$$Q_{term} = \frac{Q_{perf}}{N} \,, \tag{5.2}$$

where Q_{term} is the flow in each terminal artery and N is the number of terminal arteries. Using physiological scaling laws, one can write the following relation between each daughter radius (r_{d1} and r_{d2}) and the radius of the parent artery:

$$r_{parent}^{\gamma} = r_{d1}^{\gamma} + r_{d2}^{\gamma} \,, \tag{5.3}$$

where γ is a parameter between 2.55 and 3 depending on the network [210]. Assuming a Newtonian, laminar flow, the hydrodynamic resistance R_i for the arterial segment i can be expressed using Poiseuille's law

$$R_i = \frac{8\mu L_i}{\pi r_i^4} \,, \tag{5.4}$$

where μ denotes the viscosity of the blood which is assumed constant with $\mu = 3.6cP$. Hence, the pressure drop along a segment can be obtained as

$$\Delta P_i = R_i Q_i \,, \tag{5.5}$$

Adding a new terminal artery to the network will change the flow distribution and the resistances in the whole arterial network. We can define a reduced resistance by factoring the radius out of Eq. 5.4 for a terminal artery

$$R_{term}^* = \frac{8\mu L_t}{\pi} \,, \tag{5.6}$$

However, adding a branch to a specific segment of the network will create a subtree. The reduced resistance of the modified non-terminal artery can be calculated as [210]

$$R_{i,mod}^* = \frac{8\mu L_i}{\pi} + \left[\frac{(r_{d1}/r_i)^4}{R_{d1}^*} + \frac{(r_{d2}/r_i)^4}{R_{d2}^*}\right]^{-1} , \tag{5.7}$$

According to Eq. 5.7, the reduced resistance of a modified branch is associated with the radii of the daughter arteries. Thus, its $R_{i,mod}^*$ needs to be calculated by recursively traversing the subtrees of the modified segment in postorder mode via traversing the left subtree, then the right subtree (see [210]). Assuming a constant pressure at all the terminal arteries, the flow ratio at each new bifurcation can be calculated as

$$\frac{Q_{i,mod}}{Q_{i,new}} = \frac{R_{i,new}}{R_{i,mod}} = \frac{R_{i,new}^*/r_{i,new}^4}{R_{i,mod}^*/r_{i,mod}^4} , \tag{5.8}$$

where $R_{i,mod}$ is the hydrodynamic resistance of the modified segment which includes the total resistance in the following subtree of this segment and $R_{i,new}$ is the resistance of the newly added terminal segment. Using Eq. 5.12 we can calculate the radius ratio of two daughter arteries as follows

$$\frac{r_{i,mod}}{r_{i,new}} = \left[\frac{Q_{i,mod}R_{i,mod}^*}{Q_{i,new}R_{i,new}^*}\right]^{1/4} , \tag{5.9}$$

Using Eq. 5.3, we can calculate the bifurcation ratios for the parent artery of i, mod and i, new segments

$$\beta_{parent-i,new} = \left[1 + \left(\frac{r_{i,mod}}{r_{i,new}}\right)^{-\gamma}\right]^{-1/\gamma} , \tag{5.10a}$$

$$\beta_{parent-i,mod} = \left[1 + \left(\frac{r_{i,mod}}{r_{i,new}}\right)^{\gamma}\right]^{-1/\gamma} , \tag{5.10b}$$

The bifurcation ratios $\beta_{parent-i,mod}$ and $\beta_{parent-i,new}$ are based on geometrical constraints and flow distribution inside the arterial network. Adding a new terminal segment also changes the flow in the upstream network. We can use the same concept and equations to correct the flows and resistances up to the root segment. The corrected radius of the root artery can be calculated as follows

$$r_{root} = \left(\frac{R_{root,mod}}{R^*_{root,mod}} \right)^{1/4} \, , \tag{5.11}$$

where $R_{root,mod}$ is the total resistance of the network.

5.2.2 Vascular network generation

With the use of physics-based mathematical framework presented in the previous section, we can iteratively add arterial segments to the network while meeting the aforementioned constraints. However, it has been shown that growth of vascular networks is not random but they are structured in a way that the blood is supplied to tissues with an optimal cost [210]. This makes the generation of arterial networks a constrained optimization problem. Here, we define the objective function as follows

$$\sum_j L_j^\eta r_j^\lambda \, , \tag{5.12}$$

where η and λ are dimensionality constants. Here we choose $\eta = 1$ and $\lambda = 2$ which correspond to the volume of each vessel. We assume that every added terminal node to the network may be connected to one of the first 10 closest arterial segments. Thus, there are two aspects into the optimization, i.e. geometrical and structural. When a new terminal node is connected to the first candidate segment (closest segment), the location of bifurcation needs to be optimized in a way that the objective function is minimized. This process

involves the correction of flows and resistances in the entire network of arteries at every optimization step. Then, the new network can be stored, the old network will be used again to find the second closest candidate segment and the optimization process will be performed again for this new network. All the 10 closest candidate segments will be examined and the network with the smallest cost function will be selected. Here, we define the cost function as the volume of the entire network. Also, more constraints including a minimum length for each segment, no intersection between segments, the bifurcation angle constraints, and the distance of new terminal nodes from other established nodes are applied. Figure 5.1 shows the steps implemented in the automatic arterial network generation.

In this study, we used an open-source nonlinear optimization package called Nlopt [211] to perform optimization of the location of each bifurcation based on geometrical and physiological constraints. Specifically, a local derivative-free optimization algorithm called Constrained Optimization BY Linear Approximations (COBYLA) was utilized [212]. This algorithm allows the application of nonlinear constraints in the optimization process.

The developed software has the ability to generate an input file executable in *Simvascular*'s 1D solver. The generated input file contains the information about the coordinates of the nodes, connectivity between segments, segment data including the finite element mesh size, boundary conditions, material properties, and the perfusion map information.

One of the assumption in the CCO algorithm is to consider a rigid wall for the arteries. In reality, the vascular networks show deformable walls. If we consider a deformable arterial wall and use *Simvascular*'s 1D solver, the flows at each terminal segment will not follow the perfusion map. To resolve this issue, an iterative diameter tuning algorithm was added to the *Simvascular*'s 1D solver. The purpose of this algorithm is to find new diameters for each segment in the entire network that result in a terminal flow distribution matching the perfusion map. The algorithm solves the entire network for a constant inflow rate for a period of 1 s. Then, it stores the values of flow rate and diameter for each segment of the
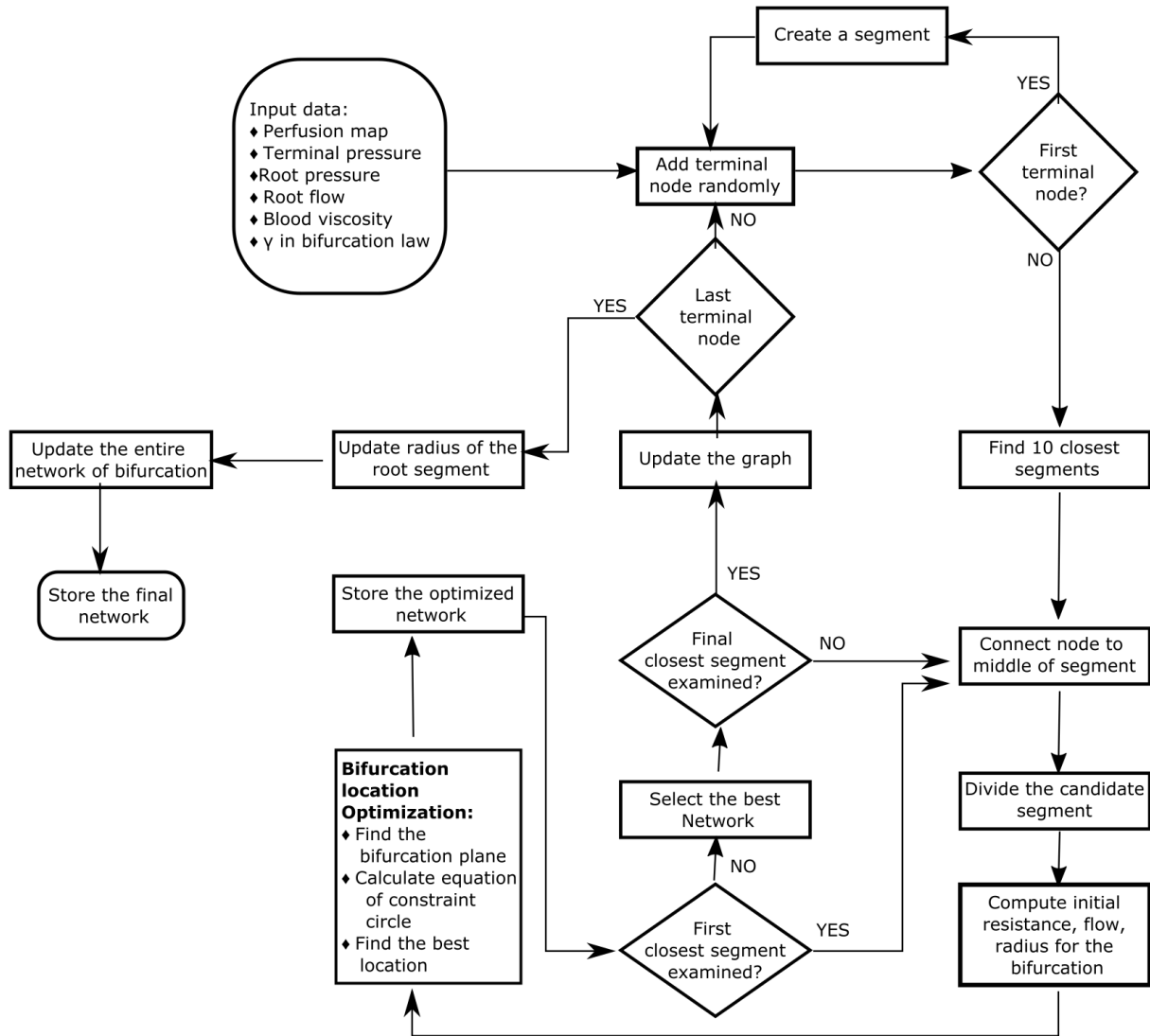
Figure 5.1: Summary of the steps taken in developing the automatic generation of arterial network.

network and compare the terminal flow distribution to the perfusion map data. Based on the terminal flow distribution, the diameter of each segment will be updated and the blood flow will be solved in the entire network. This iterative process continues until the mean squared error (MSE) between the perfusion map and the calculated terminal flow distribution become less than 10^{-7}.

5.3 Results

The 1D CCO algorithm was used to simulate the generation of arterial network using various theoretical perfusion maps. In this section, the generated arterial networks confined in a cube considering one compartment perfusion map, 6 compartments, and 9 layered compartments, and a network inside a spherical domain with 6 perfusion compartments are presented.

Figure 5.2 shows the different stages in generation of an arterial network. These stages include 2, 3, 4, 5, 10, and 28 terminal nodes. The changes in the location of bifurcations are visible in this figure. The arterial network in this figure corresponds to one compartment perfusion map. The input data to generate these networks were as follows: $Q_{perf} = 0.05 ml/s$, $p_{term} = 83 mm\,Hg$, and $p_{perf} = 133 mm\,Hg$.
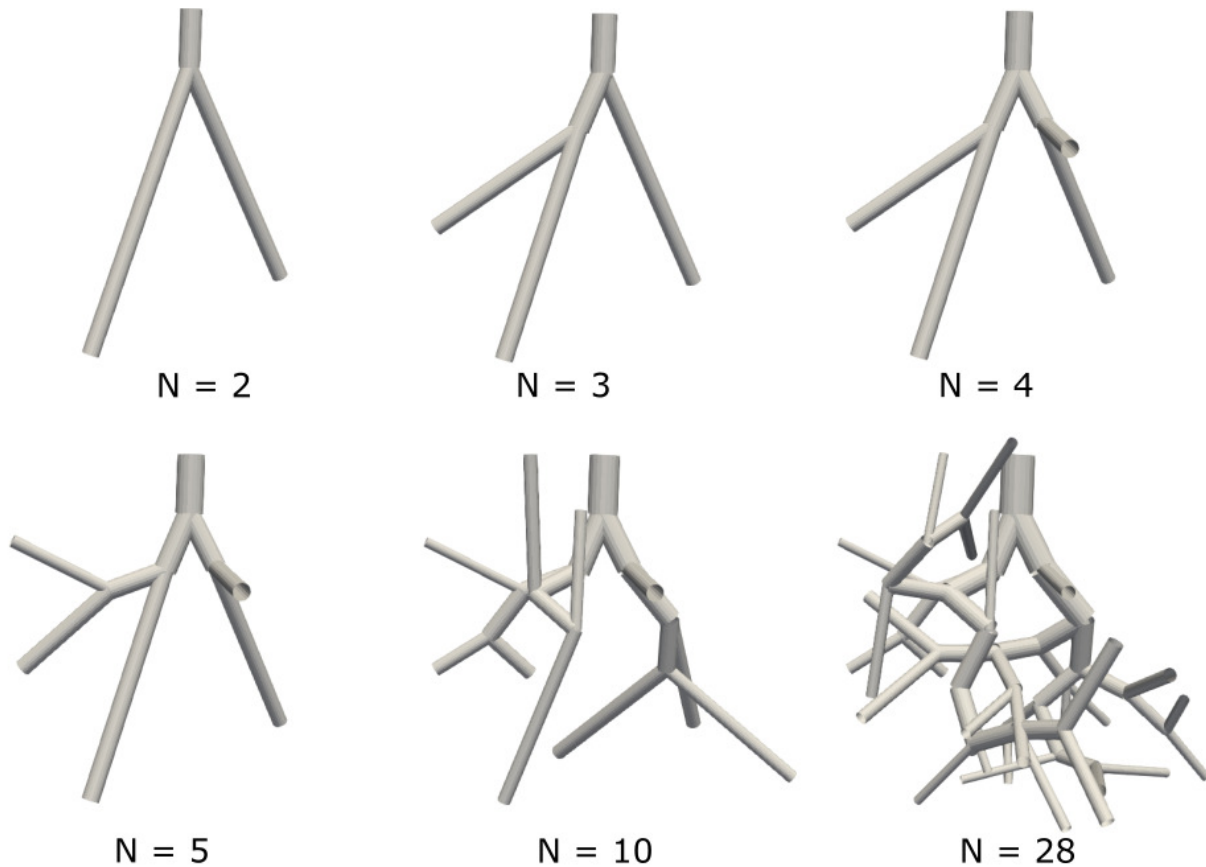
Figure 5.2: The evolution of an arterial network through various stages of the CCO algorithm.

Figure 5.3 shows the test cases with bifurcation angle constraints without any maximum length constraint. As it can be seen in this figure, there is no bifurcation with too large or small angle. In this study, we assumed a bifurcation angle between 30 and 150 degrees. This constraint helps generation of a structured network and in fact decreases the computation time for generation of large networks. The angle constraint ensures systematic generation of bifurcation. The input data to generate these networks were as follows: $Q_{perf} = 0.1ml/s$, $p_{term} = 83mm\,Hg$, and $p_{perf} = 133mm\,Hg$.

N = 21   N = 40
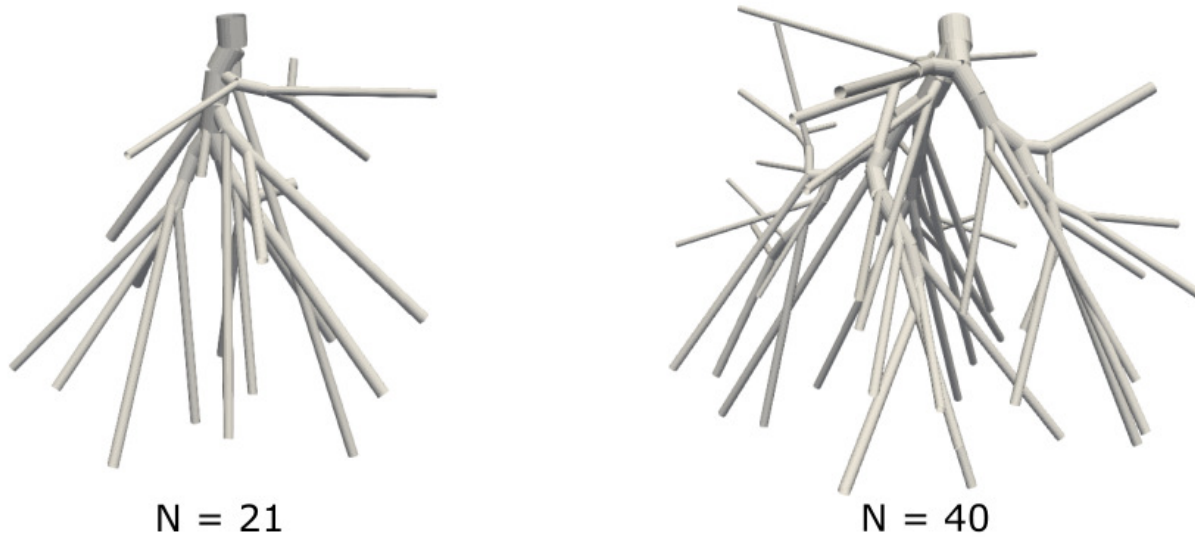
Figure 5.3: The effect of bifurcation angle constraint on the arterial network.

Figure 5.4 shows the generated arterial networks assuming a uniform perfusion block. This means that all the terminal nodes are placed randomly in the domain of interest and all the terminal segments supply a same amount of blood flow. The input data to generate these networks were as follows: $Q_{perf} = 0.1ml/s$, $p_{term} = 83mm\,Hg$, and $p_{perf} = 133mm\,Hg$.

Figure 5.5 demonstrate the generated arterial networks assuming 6 different perfusion compartments. For this case, a weighted random coordinates generator was used to add terminal nodes inside the domain. The weights were selected based on the percentage of blood supply at each compartment. As it can be seen, the CCO algorithm generated a network of vasculature with larger number of segments in regions with higher probability of blood perfusion.

<center>N = 21   N = 20   N = 24   N = 40</center>
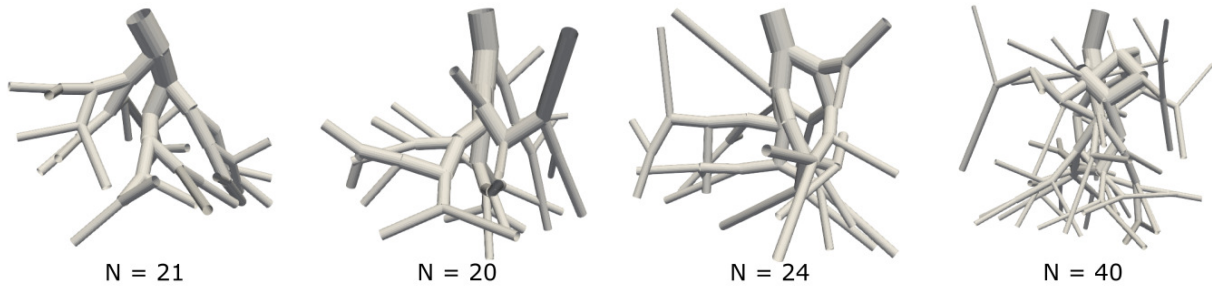
Figure 5.4: Generation of a network with various numbers of terminal nodes without any perfusion map. This figure shows the random evolution of vascular network.

The terminal flow for all the segments in a specific compartment was assumed to be constant, but different for different compartments. The input data to generate these networks were as follows: $Q_{perf} = 0.05 ml/s$, $p_{term} = 83 mm\,Hg$, and $p_{perf} = 133 mm\,Hg$.

<center>N = 47   N = 69   N = 79</center>

<center>5   20 25
Perfusion %</center>
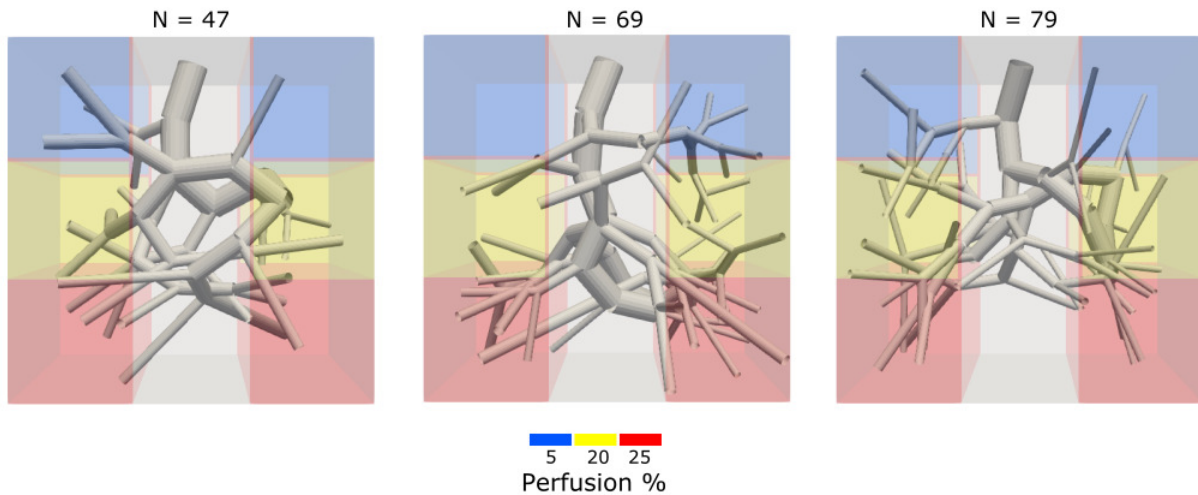
Figure 5.5: Arterial network generated in a block with multiple perfusion areas. the middle block has zero percentage of blood perfusion and the results do not show any terminal segment in this area.

Figure 5.6 shows the generation of arterial network in a theoretical layered perfusion map. In this case, it is assumed that the bottom layer has the largest perfusion flow. As it can be seen, the generated networks are structured in a way that the number of terminal segments at the bottom of the block is larger than other layers. The input data to generate these networks were as follows: $Q_{perf} = 0.02 ml/s$, $p_{term} = 83 mm\,Hg$, and $p_{perf} = 133 mm\,Hg$.

Figure 5.7 shows the generated vascular network using 65 terminal nodes (124 segments) inside a spherical domain. The perfusion map was assumed to be consisted of 5 compartments

<center>101</center>

5   20 25 40
Perfusion %
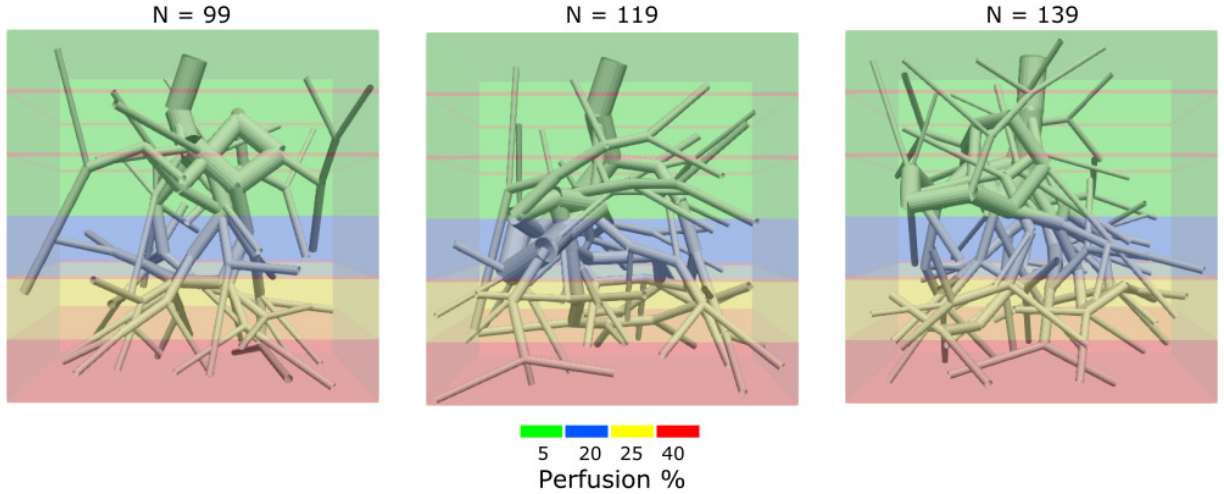
Figure 5.6: Arterial network generated based on a layered perfusion map. The results show higher density of terminal segments in the bottom of the block.

with highest percentage of perfusion flow at the outer layer of the sphere. The input data to generate this network were as follows: $Q_{perf} = 0.03ml/s$, $p_{term} = 83mm\,Hg$, and $p_{perf} = 133mm\,Hg$.

Figure 5.8 shows the a tree with 35 terminal segments. The left panel shows the generated network from the developed automatic arterial network generation software colored by the cross-sectional area of each segment. The right panel shows the same network after tuning the areas so that the flows at terminal segments match the perfusion map when considering deformable walls for the network. The input data to generate these network were as follows: $Q_{perf} = 0.05ml/s$, $p_{term} = 83mm\,Hg$, and $p_{perf} = 133mm\,Hg$.

5.4   Discussion

The main motivation behind developing the presented automatic arterial generation package was to study the structure of an arterial network based on the perfusion maps. Specially, in case of microvascular disease that imaging techniques cannot capture the network, such algorithms can be used to computationally generate the corresponding microvascular net-
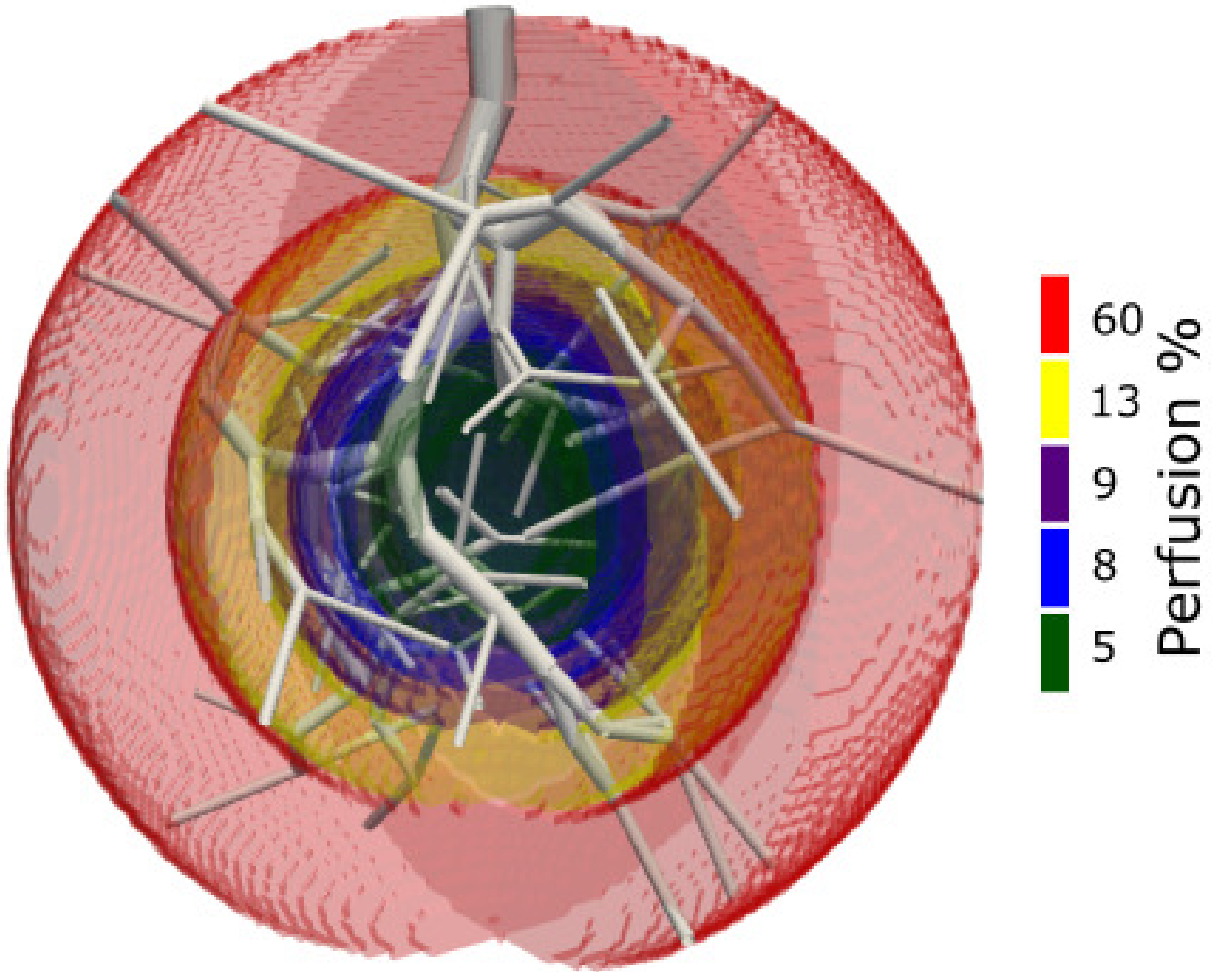
Figure 5.7: Arterial network generated based on a spherical perfusion map (125 segments). A quarter of the sphere is sliced out to better visualize the generated network.

work based on the mathematical and physiological laws and the perfusion maps obtained from positron emission tomography (PET) data, oxygen supply in the tissue, or fractional myocardial blood volume (fMBV) maps obtained from ferumoxytol-enhanced magnetic resonance imaging. Another use case of such algorithm is to discover the hierarchy in a network, lengths of segments, and density of arterial sub-trees in different regions.

The theoretical results showed an interesting transition in the structure of the tree in different stages. The distribution of flows in the terminal segments can change the location of the upstream bifurcations in the early stage of development (Fig. 5.4). This change in the
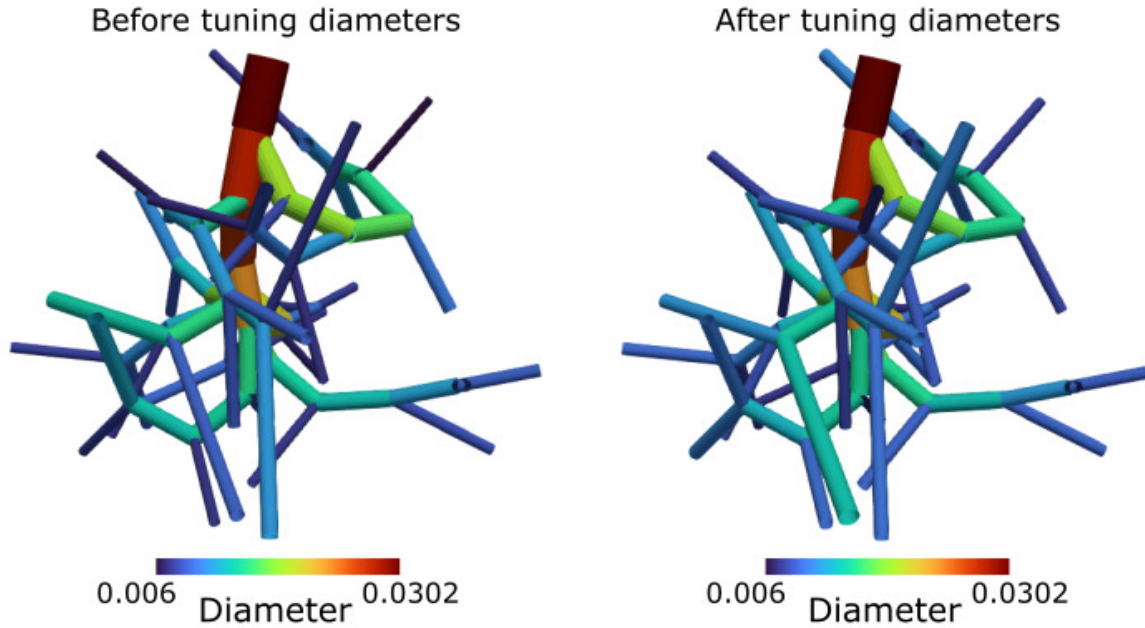
Figure 5.8: Global tuning of the segment diameter. The left panel shows the generate network with 35 terminal segments using the developed arterial network generation software. The right panel shows the same network after tuning each segment's diameter so that the collective flow at the terminal matches the perfusion data when considering deformable wall for the network.

geometry of the network is related to the fact that different flow distribution results in different segment diameters and a change in the location of optimized bifurcation. This slight change can significantly alter the path of the segment when more terminal nodes are added.

It should be noted that straight arterial segments were used in this study to decrease the computational cost. In reality, the arterial segments are not straight but they follow the curvature of a tissue. Even in the case of microvascular network, the segments are not perfectly straight. However, adding a constraint to the algorithm to follow a surface is possible even if the segments are assumed straight [209]. To do so, one can generate the terminal nodes in a specific radius of a segment and let the network grow based on the local growth of the subtree. On the other hand, using curved segments adds many additional degrees of freedom to the optimization process which leads to higher computational cost.

The presented results in this chapter show the capability of the developed package to simulate the generation of arterial/microvascular networks based on physiological principles. One can

use CT images to create the 3D model of visible arteries around an organ and generate the arterial network based on the 3D model. Using the developed 1D-3D solver in previous chapter, enables us to simulate the blood flow distribution in a large network of vessels. It should be noted that due to the randomness of the generated tree, it will be unlikely to use this model as a replica of real vascular networks. However, incorporating more physiological constraints can lead to a more realistic model.

In summary, we developed an automatic vascular network generation package based on the known physiological and mathematical laws. The results showed the potential of this algorithm in generation of such networks for different theoretical perfusion maps (Figs. 5.5 and 5.6). This work is in progress to create more realistic vascular networks. The next steps are adding an arbitrary surface constraint so that the network can be developed around curved surfaces, improving boundary conditions, and the ability to simulate the microvascular network inside an organ.

Chapter 6

Conclusion

This dissertation consisted of two main sections: (i) the association between hemodynamic/biotransport parameters and longitudinal changes in the plaque vulnerability characteristics, and (ii) developing a 1D automatic vascular network generation package with the ability to be coupled with a 3D patient-specific model in *Simvascular*.

In the first part, we have studied the near-wall transport of major biochemicals and cells contributing to the initiation and progression of atherosclerosis. The near-wall transport of low-density lipoprotein, nitric oxide, adenosine triphosphate, oxygen, monocytes, and monocyte chemoattractant protein-1 was simulated in 8 diseased human coronary arteries and 2 healthy swine coronary arteries. The results of this study showed that near-wall localization patterns are dictated by WSS magnitude and vectorial features (WSS LCS). Our results were compared with prior mechanotransduction studies and we presented a comprehensive theory for the role of WSS in atherosclerosis. High WSS magnitude protected against atherosclerosis by increasing the production or flux of atheroprotective biochemicals and decreasing the near-wall localization of atherogenic biochemicals. Low WSS magnitude promoted atherosclerosis by increasing atherogenic biochemical localization. Finally, the

attracting WSS LCS's role was more complex where it promoted or prevented atherosclerosis based on different biochemicals.

To find the association between hemodynamic/biotransport parameters calculated in Chapter 2 and the longitudinal changes in the vulnerability characteristics of the plaques, we developed an atherosclerotic plaque quantification software to accurately quantify the vulnerability characteristics of coronary artery plaques using a segment-specific method. The developed software has the ability to visualize DICOM image series, create arterial centerlines, generate the cross-sectional view of the vessel, quantify the volumes of low attenuation plaque, fibrous plaque, calcium plaque, and the lumen. For qualitative parameters such as napkin-ring sign, positive remodeling, severe stenosis, and spotty calcification, the user is provided an option to select the presence of these characteristics in each segment of the coronary artery. This software uses the vesselness enhancement algorithm to prevent organ over-projection effect, vessel wall and plaque membership functions to ensure the inclusion of the whole vessel in the segmented image, and an adaptive threshold method to accurately quantify different plaque components. We used this software to quantify 16 diseased coronary arteries (8 baseline and 8 follow-up) and found the association of hemodynamic/biotransport parameters at baseline with the longitudinal changes in the plaque characteristics. Our statistical analysis showed that WSS magnitude and the divergence of WSS vectors are moderately correlated with the longitudinal changes in the fibrous plaque volume and presence of napkin-ring sign in the follow-up. Our results did not show any meaningful association between atherogenic/atheroprotective biochemical localization and the longitudinal changes in the vulnerability characteristics.

In the second part (Chapters 4 and 5), a framework was proposed to couple the 1D and 3D solvers in *Simvascular* and a package was developed to automatically generate a 1D network of arteries that can be used in the developed hybrid 1D-3D solver. The performance of our coupled 1D-3D solver was compared against the existing data in the literature and showed

good agreement with them. The automatic vascular network generation package uses the well-known constrained constructive optimization (CCO) algorithm to locally optimize the location of each bifurcation and uses an iterative algorithm to tune the areas of all the segments in the arterial tree when a deformable arterial wall is assumed. The developed package was tested for multiple 3D perfusion maps and different aspects of generated networks were discussed. The developed packages can be linked together to study the microvascular disease as well as vulnerable plaques in coronary arteries.

6.1   Future directions

There are several areas that this study can be extended to in the future:

1. The developed plaque quantification and 3D model segmentation can be used for a larger population to increase the power of statistical analysis. Increasing the sample size will also increases the diversity of various characteristics of vulnerable plaques. This can lead to more meaningful correlation between the hemodynamic/biotransport parameters and the longitudinal changes in the atherosclerotic plaque.

2. The developed plaque quantification and 3D model segmentation can be used for a population under prescription of novel drugs to analyze how the hemodynamics can affect the efficacy of the drug in various segments of the coronary arteries. The developed software provides a powerful tool for researchers to study the role of various wall shear stress parameters in progression of atherosclerosis.

3. The developed 1D-3D solver and the vascular tree generation package can be coupled to study the effect of stenosis on the blood supply in the microvascular network. We are planning to use the developed package to study the blood flow distribution in the heart tissue using blood perfusion maps and patient-specific models.

4. The developed framework for automatic vascular tree generation algorithm can be enhanced by including more physiological laws, adding a surface conforming algorithm, and combining it with other existing algorithms such as Monte Carlo recursive algorithm, to be able to create circulatory networks which connect the arterial side to the venous circulation through a physiologically consistent capillary bed.

Bibliography

[1] S. S. Virani, A. Alonso, E. J. Benjamin, M. S. Bittencourt, C. W. Callaway, A. P. Carson, A. M. Chamberlain, A. R. Chang, S. Cheng, F. N. Delling, *et al.*, "Heart disease and stroke statistics-2020 update: A report from the american heart association.," *Circulation*, vol. 141, no. 9, p. e139, 2020.

[2] A. J. Lusis, "Genetics of atherosclerosis," *Trends in Genetics*, vol. 28, no. 6, pp. 267–275, 2012.

[3] D. E. Conway and M. A. Schwartz, "Flow-dependent cellular mechanotransduction in atherosclerosis," *J Cell Sci*, vol. 126, no. 22, pp. 5101–5109, 2013.

[4] S. Waxman, F. Ishibashi, and J. E. Muller, "Detection and treatment of vulnerable plaques and vulnerable patients: novel approaches to prevention of coronary events," *Circulation*, vol. 114, no. 22, pp. 2390–2411, 2006.

[5] A. Millon, J.-L. Mathevet, L. Boussel, P. L. Faries, Z. A. Fayad, P. C. Douek, and P. Feugier, "High-resolution magnetic resonance imaging of carotid atherosclerosis identifies vulnerable carotid plaques," *Journal of vascular surgery*, vol. 57, no. 4, pp. 1046–1051, 2013.

[6] K. Yamada, M. Kawasaki, S. Yoshimura, M. Shirakawa, K. Uchida, S. Shindo, S. Nishida, Y. Iwamoto, S. Nakahara, and Y. Sato, "High-intensity signal in carotid plaque on routine 3d-tof-mra is a risk factor of ischemic stroke," *Cerebrovascular Diseases*, vol. 41, no. 1-2, pp. 13–18, 2016.

[7] J. R. Levick, *An introduction to cardiovascular physiology.* Butterworth-Heinemann, 2013.

[8] J. Zhou, Y. Li, and S. Chien, "Shear stress–initiated signaling and its regulation of endothelial function," *Arteriosclerosis, Thrombosis, and Vascular Biology*, vol. 34, no. 10, pp. 2191–2198, 2014.

[9] S. Baratchi, K. Khoshmanesh, O. L. Woodman, S. Potocnik, K. Peter, and P. McIntyre, "Molecular sensors of blood flow in endothelial cells," *Trends in Molecular Medicine*, vol. 23, no. 9, pp. 850–868, 2017.

[10] Z. Peng, B. Shu, Y. Zhang, and M. Wang, "Endothelial response to pathophysiological stress," *Arteriosclerosis, Thrombosis, and Vascular Biology*, vol. 39, no. 11, pp. e233–e243, 2019.

[11] K. Nakajima, T. Nakano, and A. Tanaka, "The oxidative modification hypothesis of atherosclerosis: the comparison of atherogenic effects on oxidized ldl and remnant lipoproteins in plasma," *Clinica Chimica Acta*, vol. 367, no. 1-2, pp. 36–47, 2006.

[12] G. Rath, C. Dessy, O. Feron, *et al.*, "Caveolae, caveolin and control of vascular tone: nitric oxide (no) and endothelium derived hyperpolarizing factor (edhf) regulation," *J Physiol Pharmacol*, vol. 60, no. Suppl 4, pp. 105–109, 2009.

[13] B. J. Buckley, Z. M. Marshall, and A. R. Whorton, "Nitric oxide stimulates nrf2 nuclear translocation in vascular endothelium," *Biochemical and Biophysical Research Communications*, vol. 307, no. 4, pp. 973–979, 2003.

[14] B. G. Coon, N. Baeyens, J. Han, M. Budatha, T. D. Ross, J. S. Fang, S. Yun, J. Thomas, and M. A. Schwartz, "Intramembrane binding of ve-cadherin to vegfr2 and vegfr3 assembles the endothelial mechanosensory complex," *Journal of Cell Biology*, vol. 208, no. 7, pp. 975–986, 2015.

[15] M. Y. Pahakis, J. R. Kosky, R. O. Dull, and J. M. Tarbell, "The role of endothelial glycocalyx components in mechanotransduction of fluid shear stress," *Biochemical and Biophysical Research Communications*, vol. 355, no. 1, pp. 228–233, 2007.

[16] R. Xing, A. M. Moerman, Y. Ridwan, M. J. Daemen, A. van der Steen, F. Gijsen, and K. van der Heiden, "Temporal and spatial changes in wall shear stress during atherosclerotic plaque progression in mice," *Royal Society Open Science*, vol. 5, no. 3, p. 171447, 2018.

[17] M. O. Khan, T. Nishi, S. Imura, J. Seo, H. Wang, Y. Honda, K. Nieman, I. S. Rogers, J. A. Tremmel, J. Boyd, *et al.*, "Colocalization of coronary plaque with wall shear stress in myocardial bridge patients," *Cardiovascular Engineering and Technology*, pp. 1–11, 2022.

[18] L. Grindberg, *Topics in ultrascale scientific computing with application in biomedical modeling*. PhD thesis, Brown University, 2009.

[19] L. Grinberg, T. Anor, E. Cheever, J. R. Madsen, and G. E. Karniadakis, "Simulation of the human intracranial arterial tree," *Philosophical Transactions of the Royal Society A: Mathematical, Physical and Engineering Sciences*, vol. 367, no. 1896, pp. 2371–2386, 2009.

[20] N. Grande Gutiérrez, T. Sinno, and S. L. Diamond, "A 1d–3d hybrid model of patient-specific coronary hemodynamics," *Cardiovascular Engineering and Technology*, vol. 13, no. 2, pp. 331–342, 2022.

[21] J. Mynard and P. Nithiarasu, "A 1d arterial blood flow model incorporating ventricular pressure, aortic valve and regional coronary flow using the locally conservative galerkin (lcg) method," *Communications in numerical methods in engineering*, vol. 24, no. 5, pp. 367–417, 2008.

[22] L. Grinberg, E. Cheever, T. Anor, J. R. Madsen, and G. Karniadakis, "Modeling blood flow circulation in intracranial arterial networks: a comparative 3d/1d simulation study," *Annals of biomedical engineering*, vol. 39, no. 1, pp. 297–309, 2011.

[23] L. Formaggia, J.-F. Gerbeau, F. Nobile, and A. Quarteroni, "On the coupling of 3d and 1d navier–stokes equations for flow problems in compliant vessels," *Computer methods in applied mechanics and engineering*, vol. 191, no. 6-7, pp. 561–582, 2001.

[24] W. Schreiner, R. Karch, M. Neumann, F. Neumann, P. Szawlowski, and S. Roedler, "Optimized arterial trees supplying hollow organs," *Medical engineering & physics*, vol. 28, no. 5, pp. 416–429, 2006.

[25] J. N. Ulysses, L. A. Berg, E. M. Cherry, B. R. Liu, R. W. Dos Santos, B. G. de Barros, B. M. Rocha, and R. A. de Queiroz, "An optimization-based algorithm for the construction of cardiac purkinje network models," *IEEE Transactions on Biomedical Engineering*, vol. 65, no. 12, pp. 2760–2768, 2018.

[26] Y. Pan, F. Zhou, Z. Song, H. Huang, Y. Chen, Y. Shen, Y. Jia, and J. Chen, "Oleanolic acid protects against pathogenesis of atherosclerosis, possibly via fxr-mediated angiotensin (ang)-(1–7) upregulation," *Biomedicine & Pharmacotherapy*, vol. 97, pp. 1694–1700, 2018.

[27] S. Zha, F. Wang, Z. Li, Z. Ma, L. Yang, and F. Liu, "Pj34, a parp1 inhibitor, promotes endothelial repair in a rabbit model of high fat diet-induced atherosclerosis," *Cell Cycle*, vol. 18, no. 17, pp. 2099–2109, 2019.

[28] P. F. Davies, K. A. Barbee, M. V. Volin, A. Robotewskyj, J. Chen, L. Joseph, *et al.*, "Spatial relationships in early signaling events of flow-mediated endothelial mechanotransduction," *Annual Review of Physiology*, vol. 59, no. 1, pp. 527–549, 1997.

[29] J. L. Johnson and A. C. Newby, "Macrophage heterogeneity in atherosclerotic plaques," *Current Opinion in Lipidology*, vol. 20, no. 5, p. 370, 2009.

[30] P. A. Cahill and E. M. Redmond, "Vascular endothelium–gatekeeper of vessel health," *Atherosclerosis*, vol. 248, pp. 97–109, 2016.

[31] F. E. Curry and R. H. Adamson, "Endothelial glycocalyx: permeability barrier and mechanosensor," *Annals of Biomedical Engineering*, vol. 40, no. 4, pp. 828–839, 2012.

[32] X. Zhang, D. Sun, J. W. Song, J. Zullo, M. Lipphardt, L. Coneh-Gould, and M. S. Goligorsky, "Endothelial cell dysfunction and glycocalyx–a vicious circle," *Matrix Biology*, vol. 71, pp. 421–431, 2018.

[33] M. Alimohammadi, C. Pichardo-Almarza, O. Agu, and V. Díaz-Zuccarini, "A multi-scale modelling approach to understand atherosclerosis formation: A patient-specific case study in the aortic bifurcation," *Proceedings of the Institution of Mechanical Engineers, Part H: Journal of Engineering in Medicine*, vol. 231, no. 5, pp. 378–390, 2017.

[34] L. M. Cancel, A. Fitting, and J. M. Tarbell, "In vitro study of ldl transport under pressurized (convective) conditions," *American Journal of Physiology-Heart and Circulatory Physiology*, vol. 293, no. 1, pp. H126–H132, 2007.

[35] U. Olgac, D. Poulikakos, S. C. Saur, H. Alkadhi, and V. Kurtcuoglu, "Patient-specific three-dimensional simulation of ldl accumulation in a human left coronary artery in its healthy and atherosclerotic states," *American Journal of Physiology-Heart and Circulatory Physiology*, vol. 296, no. 6, pp. H1969–H1982, 2009.

[36] J. M. Tarbell, "Shear stress and the endothelial transport barrier," *Cardiovascular Research*, vol. 87, no. 2, pp. 320–330, 2010.

[37] A. M. Plata, S. J. Sherwin, and R. Krams, "Endothelial nitric oxide production and transport in flow chambers: the importance of convection," *Annals of Biomedical Engineering*, vol. 38, no. 9, pp. 2805–2816, 2010.

[38] X. Liu, Y. Fan, X. Y. Xu, and X. Deng, "Nitric oxide transport in an axisymmetric stenosis," *Journal of the Royal Society Interface*, vol. 9, no. 75, pp. 2468–2478, 2012.

[39] J. Chen, Z. Ye, X. Wang, J. Chang, M. Yang, H. Zhong, F. Hong, and S. Yang, "Nitric oxide bioavailability dysfunction involves in atherosclerosis," *Biomedicine & Pharmacotherapy*, vol. 97, pp. 423–428, 2018.

[40] H. W. Choi and A. I. Barakat, "Modulation of atp/adp concentration at the endothelial cell surface by flow: effect of cell topography," *Annals of Biomedical Engineering*, vol. 37, no. 12, p. 2459, 2009.

[41] K. R. Qin, C. Xiang, Z. Xu, L. L. Cao, S. S. Ge, and Z. L. Jiang, "Dynamic modeling for shear stress induced atp release from vascular endothelial cells," *Biomechanics and Modeling in Mechanobiology*, vol. 7, no. 5, pp. 345–353, 2008.

[42] K. Theodorou and R. A. Boon, "Endothelial cell metabolism in atherosclerosis," *Frontiers in Cell and Developmental Biology*, vol. 6, p. 82, 2018.

[43] F. Iori, L. Grechy, R. W. Corbett, W. Gedroyc, N. Duncan, C. G. Caro, and P. E. Vincent, "The effect of in-plane arterial curvature on blood flow and oxygen transport in arterio-venous fistulae," *Physics of Fluids*, vol. 27, no. 3, p. 031903, 2015.

[44] E. A. Murphy, A. S. Dunne, D. M. Martin, and F. J. Boyle, "Oxygen mass transport in stented coronary arteries," *Annals of Biomedical Engineering*, vol. 44, no. 2, pp. 508–522, 2016.

[45] J. Tarbell, M. Mahmoud, A. Corti, L. Cardoso, and C. Caro, "The role of oxygen transport in atherosclerosis and vascular disease," *Journal of the Royal Society Interface*, vol. 17, no. 165, p. 20190732, 2020.

[46] M. Cilla, E. Pena, and M. A. Martinez, "Mathematical modelling of atheroma plaque formation and development in coronary arteries," *Journal of The Royal Society Interface*, vol. 11, no. 90, p. 20130866, 2014.

[47] W. Hao, S. Gong, S. Wu, J. Xu, M. R. Go, A. Friedman, and D. Zhu, "A mathematical model of aortic aneurysm formation," *PloS One*, vol. 12, no. 2, 2017.

[48] P. Yao, H. Zhao, W. Mo, and P. He, "Laminar shear stress promotes vascular endothelial cell autophagy through upregulation with rab4," *DNA and Cell Biology*, vol. 35, no. 3, pp. 118–123, 2016.

[49] A. D. Chalmers, A. Cohen, C. A. Bursill, and M. R. Myerscough, "Bifurcation and dynamics in a mathematical model of early atherosclerosis," *Journal of Mathematical Biology*, vol. 71, no. 6-7, pp. 1451–1480, 2015.

[50] K. Leemasawatdigul and H. Gappa-Fahlenkamp, "Development of a mathematical model to describe the transport of monocyte chemoattractant protein-1 through a three-dimensional collagen matrix," *Cardiovascular Pathology*, vol. 21, no. 3, pp. 219–228, 2012.

[51] S. Fazli, E. Shirani, and M. R. Sadeghi, "Numerical simulation of LDL mass transfer in a common carotid artery under pulsatile flows," *Journal of Biomechanics*, vol. 44, no. 1, pp. 68–76, 2011.

[52] S. Kim and D. P. Giddens, "Mass transport of low density lipoprotein in reconstructed hemodynamic environments of human carotid arteries: the role of volume and solute flux through the endothelium," *Journal of Biomechanical Engineering*, vol. 137, no. 4, 2015.

[53] V. Díaz-Zuccarini, G. Di Tomaso, O. Agu, and C. Pichardo-Almarza, "Towards personalised management of atherosclerosis via computational models in vascular clinics: technology based on patient-specific simulation approach," *Healthcare Technology Letters*, vol. 1, no. 1, pp. 13–18, 2014.

[54] M. Alimohammadi, C. Pichardo-Almarza, O. Agu, and V. Díaz-Zuccarini, "Development of a patient-specific multi-scale model to understand atherosclerosis and calcification locations: comparison with in vivo data in an aortic dissection," *Frontiers in Physiology*, vol. 7, p. 238, 2016.

[55] S. V. Lopez-Quintero, X. Ji, D. A. Antonetti, and J. M. Tarbell, "A three-pore model describes transport properties of bovine retinal endothelial cells in normal and elevated glucose," *Investigative Ophthalmology & Visual Science*, vol. 52, no. 2, pp. 1171–1180, 2011.

[56] D. Hardman, B. J. Doyle, S. I. K. Semple, J. M. J. Richards, D. E. Newby, W. J. Easson, and P. R. Hoskins, "On the prediction of monocyte deposition in abdominal aortic aneurysms using computational fluid dynamics," *Proceedings of the Institution of Mechanical Engineers, Part H: Journal of Engineering in Medicine*, vol. 227, no. 10, pp. 1114–1124, 2013.

[57] T. Goyal, S. Mitra, M. Khaidakov, X. Wang, S. Singla, Z. Ding, S. Liu, and J. L. Mehta, "Current concepts of the role of oxidized ldl receptors in atherosclerosis," *Current Atherosclerosis Reports*, vol. 14, no. 2, pp. 150–159, 2012.

[58] K. Ghimire, J. Zaric, B. Alday-Parejo, J. Seebach, M. Bousquenaud, J. Stalin, G. Bieler, H. Schnittler, and C. Rüegg, "Magi1 mediates enos activation and no production in endothelial cells in response to fluid shear stress," *Cells*, vol. 8, no. 5, p. 388, 2019.

[59] G. K. Kolluru, S. Sinha, S. Majumder, A. Muley, J. H. Siamwala, R. Gupta, and S. Chatterjee, "Shear stress promotes nitric oxide production in endothelial cells by sub-cellular delocalization of enos: A basis for shear stress mediated angiogenesis," *Nitric Oxide*, vol. 22, no. 4, pp. 304–315, 2010.

[60] A. M. Andrews, D. Jaron, D. G. Buerk, P. L. Kirby, and K. A. Barbee, "Direct, real-time measurement of shear stress-induced nitric oxide produced from endothelial cells in vitro," *Nitric Oxide*, vol. 23, no. 4, pp. 335–342, 2010.

[61] A. Farghadan and A. Arzani, "The combined effect of wall shear stress topology and magnitude on cardiovascular mass transport," *International Journal of Heat and Mass Transfer*, vol. 131, pp. 252–260, 2019.

[62] S. Zumerle, B. Calì, F. Munari, R. Angioni, F. Di Virgilio, B. Molon, and A. Viola, "Intercellular calcium signaling induced by atp potentiates macrophage phagocytosis," *Cell Reports*, vol. 27, no. 1, pp. 1–10, 2019.

[63] S. Wang, R. Chennupati, H. Kaur, A. Iring, N. Wettschureck, and S. Offermanns, "Endothelial cation channel piezo1 controls blood pressure by mediating flow-induced atp release," *The Journal of Clinical Investigation*, vol. 126, no. 12, pp. 4527–4536, 2016.

[64] A. J. Brown, Z. Teng, P. C. Evans, J. H. Gillard, H. Samady, and M. R. Bennett, "Role of biomechanical forces in the natural history of coronary atherosclerosis," *Nature Reviews Cardiology*, vol. 13, no. 4, p. 210, 2016.

[65] A. Arzani, A. M. Gambaruto, G. Chen, and S. C. Shadden, "Wall shear stress exposure time: a Lagrangian measure of near-wall stagnation and concentration in cardiovascular flows," *Biomechanics and Modeling in Mechanobiology*, vol. 16, no. 3, pp. 787–803, 2017.

[66] N. Baeyens and M. A. Schwartz, "Biomechanics of vascular mechanosensation and remodeling," *Molecular Biology of the Cell*, vol. 27, no. 1, pp. 7–11, 2016.

[67] M. R. K. Mofrad and R. D. Kamm, *Cellular mechanotransduction: diverse perspectives from molecules to tissues.* Cambridge University Press, 2009.

[68] E. Tzima, M. Irani-Tehrani, W. B. Kiosses, E. Dejana, D. A. Schultz, B. Engelhardt, G. Cao, H. DeLisser, and M. A. Schwartz, "A mechanosensory complex that mediates the endothelial cell response to fluid shear stress," *Nature*, vol. 437, no. 7057, pp. 426–431, 2005.

[69] B. P. Hierck, K. Van der Heiden, F. E. Alkemade, S. Van de Pas, *et al.*, "Primary cilia sensitize endothelial cells for fluid shear stress," *Developmental Dynamics*, vol. 237, no. 3, pp. 725–735, 2008.

[70] C. Cheng, R. van Haperen, M. de Waard, L. C. A. van Damme, D. Tempel, L. Hanemaaijer, G. W. A. van Cappellen, J. Bos, C. J. Slager, D. J. Duncker, *et al.*, "Shear stress affects the intracellular distribution of enos: direct demonstration by a novel in vivo technique," *Blood*, vol. 106, no. 12, pp. 3691–3698, 2005.

[71] K. Kliche, P. Jeggle, H. Pavenstädt, and H. Oberleithner, "Role of cellular mechanics in the function and life span of vascular endothelium," *Pflügers Archiv-European Journal of Physiology*, vol. 462, no. 2, pp. 209–217, 2011.

[72] A. M. Malek, S. L. Alper, and S. Izumo, "Hemodynamic shear stress and its role in atherosclerosis," *JAMA*, vol. 282, no. 21, pp. 2035–2042, 1999.

[73] Z. Li, M. Martin, J. Zhang, H. Huang, L. Bai, J. Zhang, J. Kang, M. He, J. Li, M. R. Maurya, *et al.*, "Klf4 regulation of ch25h and lxr mitigates atherosclerosis susceptibility," *Circulation*, vol. 136, no. 14, p. 1315, 2017.

[74] M. A. Alaiti, G. Orasanu, D. Tugal, Y. Lu, and M. K. Jain, "Kruppel-like factors and vascular inflammation: implications for atherosclerosis," *Current Atherosclerosis Reports*, vol. 14, no. 5, pp. 438–449, 2012.

[75] N. Baeyens, C. Bandyopadhyay, B. G. Coon, S. Yun, and M. A. Schwartz, "Endothelial fluid shear stress sensing in vascular health and disease," *The Journal of Clinical Investigation*, vol. 126, no. 3, pp. 821–828, 2016.

[76] H. Xiao, M. Lu, T. Y. Lin, Z. Chen, G. Chen, W. Wang, T. Marin, T. Shentu, L. Wen, B. Gongol, *et al.*, "Sterol regulatory element binding protein 2 activation of nlrp3 inflammasome in endothelium mediates hemodynamic-induced atherosclerosis susceptibility," *Circulation*, vol. 128, no. 6, pp. 632–642, 2013.

[77] M. Dabagh, P. Jalali, P. J. Butler, A. Randles, and J. M. Tarbell, "Mechanotransmission in endothelial cells subjected to oscillatory and multi-directional shear flow," *Journal of The Royal Society Interface*, vol. 14, no. 130, p. 20170185, 2017.

[78] S. Feng, N. Bowden, M. Fragiadaki, C. Souilhol, S. Hsiao, M. Mahmoud, S. Allen, D. Pirri, B. T. Ayllon, S. Akhtar, *et al.*, "Mechanical activation of hypoxia-inducible factor 1α drives endothelial dysfunction at atheroprone sites," *Arteriosclerosis, Thrombosis, and Vascular Biology*, vol. 37, no. 11, pp. 2087–2101, 2017.

[79] J. Tran, A. Magenau, M. Rodriguez, C. Rentero, T. Royo, C. Enrich, S. R. Thomas, T. Grewal, and K. Gaus, "Activation of endothelial nitric oxide (enos) occurs through different membrane domains in endothelial cells," *PLoS One*, vol. 11, no. 3, 2016.

[80] K. Sriram, J. G. Laughlin, P. Rangamani, and D. M. Tartakovsky, "Shear-induced nitric oxide production by endothelial cells," *Biophysical Journal*, vol. 111, no. 1, pp. 208–221, 2016.

[81] J. Y.-J. Shyy and S. Chien, "Role of integrins in endothelial mechanosensing of shear stress," *Circulation Research*, vol. 91, no. 9, pp. 769–775, 2002.

[82] M. Siragusa and I. Fleming, "The enos signalosome and its link to endothelial dysfunction," *Pflügers Archiv-European Journal of Physiology*, vol. 468, no. 7, pp. 1125–1137, 2016.

[83] H. H. Lipowsky, "Role of the glycocalyx as a barrier to leukocyte-endothelium adhesion," in *Molecular, Cellular, and Tissue Engineering of the Vascular System*, pp. 51–68, Springer, 2018.

[84] T. C. Laurent and J. R. Fraser, "Hyaluronan.," *The FASEB Journal*, vol. 6, no. 7, pp. 2397–2404, 1992.

[85] J. Colombelli, A. Besser, H. Kress, E. G. Reynaud, P. Girard, E. Caussinus, U. Haselmann, J. V. Small, U. S. Schwarz, and E. H. K. Stelzer, "Mechanosensing in actin stress fibers revealed by a close correlation between force and protein localization," *Journal of Cell Science*, vol. 122, no. 10, pp. 1665–1679, 2009.

[86] M. Yoshigi, L. M. Hoffman, C. C. Jensen, H. J. Yost, and M. C. Beckerle, "Mechanical force mobilizes zyxin from focal adhesions to actin filaments and regulates cytoskeletal reinforcement," *The Journal of Cell Biology*, vol. 171, no. 2, pp. 209–215, 2005.

[87] B. Wojciak-Stothard and A. J. Ridley, "Shear stress–induced endothelial cell polarization is mediated by rho and rac but not cdc42 or pi 3-kinases," *The Journal of Cell Biology*, vol. 161, no. 2, pp. 429–439, 2003.

[88] S. Chien, "Mechanotransduction and endothelial cell homeostasis: the wisdom of the cell," *American Journal of Physiology-Heart and Circulatory Physiology*, vol. 292, no. 3, pp. H1209–H1224, 2007.

[89] S. Li, M. Kim, Y. Hu, S. Jalali, D. D. Schlaepfer, T. Hunter, S. Chien, and J. Y. J. Shyy, "Fluid shear stress activation of focal adhesion kinase linking to mitogen-activated protein kinases," *Journal of Biological Chemistry*, vol. 272, no. 48, pp. 30455–30462, 1997.

[90] S. Lehoux, "Molecular mechanisms of the vascular responses to hemodynamic forces," in *Biomechanics of Coronary Atherosclerotic Plaque*, pp. 51–88, Elsevier, 2020.

[91] K. A. Gerhold and M. A. Schwartz, "Ion channels in endothelial responses to fluid shear stress," *Physiology*, vol. 31, no. 5, pp. 359–369, 2016.

[92] K. Shaikh, A. Kinninger, L. Cherukuri, D. Birudaraju, R. Nakanishi, S. Almeida, E. Jayawardena, C. Shekar, F. Flores, S. Hamal, *et al.*, "Aged garlic extract reduces low attenuation plaque in coronary arteries of patients with diabetes: A randomized, double-blind, placebo-controlled study," *Experimental and Therapeutic Medicine*, vol. 19, no. 2, pp. 1457–1461, 2020.

[93] A. Updegrove, N. M. Wilson, J. Merkow, H. Lan, A. L. Marsden, and S. C. Shadden, "Simvascular: An open source pipeline for cardiovascular simulation," *Annals of Biomedical Engineering*, vol. 45, no. 3, pp. 525–541, 2017.

[94] M. Petranovic, A. Soni, H. Bezzera, R. Loureiro, A. Sarwar, C. Raffel, E. Pomerantsev, I. Jang, T. J. Brady, S. Achenbach, *et al.*, "Assessment of nonstenotic coronary lesions by 64-slice multidetector computed tomography in comparison to intravascular ultrasound: evaluation of nonculprit coronary lesions," *Journal of Cardiovascular Computed Tomography*, vol. 3, no. 1, pp. 24–31, 2009.

[95] A. Hoogendoorn, A. M. Kok, E. M. J. Hartman, G. de Nisco, *et al.*, "Multidirectional wall shear stress promotes advanced coronary plaque development: comparing five shear stress metrics," *Cardiovascular Research*, vol. 116, no. 6, pp. 1136–1146, 2020.

[96] G. De Nisco, A. M. Kok, C. Chiastra, D. Gallo, A. Hoogendoorn, F. Migliavacca, J. J. Wentzel, and U. Morbiducci, "The atheroprotective nature of helical flow in coronary arteries," *Annals of Biomedical Engineering*, vol. 47, no. 2, pp. 425–438, 2019.

[97] K. B. Hansen, A. Arzani, and S. C. Shadden, "Finite element modeling of near-wall mass transport in cardiovascular flows," *International Journal for Numerical Methods in Biomedical Engineering*, vol. 35, no. 1, p. e3148, 2019.

[98] S. Tada, "Numerical study of oxygen transport in a carotid bifurcation," *Physics in Medicine & Biology*, vol. 55, no. 14, p. 3993, 2010.

[99] M. Mortensen and K. Valen-Sendstad, "Oasis: a high-level/high-performance open source navier–stokes solver," *Computer Physics Communications*, vol. 188, pp. 177–188, 2015.

[100] H. J. Kim, I. E. Vignon-Clementel, J. S. Coogan, C. A. Figueroa, K. E. Jansen, and C. A. Taylor, "Patient-specific modeling of blood flow and pressure in human coronary arteries," *Annals of Biomedical Engineering*, vol. 38, no. 10, pp. 3195–3209, 2010.

[101] Y. Huo and G. S. Kassab, "Intraspecific scaling laws of vascular trees," *Journal of The Royal Society Interface*, vol. 9, no. 66, pp. 190–200, 2012.

[102] A. Arzani, "Accounting for residence-time in blood rheology models: do we really need non-newtonian blood flow modelling in large arteries?," *Journal of The Royal Society Interface*, vol. 15, no. 146, p. 20180486, 2018.

[103] P. Eslami, J. Tran, Z. Jin, J. Karady, R. Sotoodeh, M. T. Lu, U. Hoffmann, and A. Marsden, "Effect of wall elasticity on hemodynamics and wall shear stress in patient-specific simulations in the coronary arteries," *Journal of Biomechanical Engineering*, vol. 142, no. 2, 2020.

[104] A. Arzani, A. M. Gambaruto, G. Chen, and S. C. Shadden, "Lagrangian wall shear stress structures and near-wall transport in high-schmidt-number aneurysmal flows," *Journal of Fluid Mechanics*, vol. 790, pp. 158–172, 2016.

[105] A. Arzani and S. C. Shadden, "Wall shear stress fixed points in cardiovascular fluid mechanics," *Journal of Biomechanics*, vol. 73, pp. 145–152, 2018.

[106] V. Mazzi, D. Gallo, K. Calò, M. Najafi, M. O. Khan, G. De Nisco, D. A. Steinman, and U. Morbiducci, "A Eulerian method to analyze wall shear stress fixed points and manifolds in cardiovascular flows," *Biomechanics and Modeling in Mechanobiology*, pp. 1–21, 2019.

[107] G. De Nisco, P. Zhang, K. Calò, X. Liu, R. Ponzini, C. Bignardi, G. Rizzo, X. Deng, D. Gallo, and U. Morbiducci, "What is needed to make low-density lipoprotein transport in human aorta computational models suitable to explore links to atherosclerosis? impact of initial and inflow boundary conditions," *Journal of Biomechanics*, vol. 68, pp. 33–42, 2018.

[108] K. E. Jansen, C. H. Whiting, and G. M. Hulbert, "A generalized-alpha method for integrating the filtered Navier-Stokes equations with a stabilized finite element method," *Computer Methods in Applied Mechanics and Engineering*, vol. 190, no. 3-4, pp. 305–319, 2000.

[109] U. Olgac, V. Kurtcuoglu, and D. Poulikakos, "Computational modeling of coupled blood-wall mass transport of ldl: effects of local wall shear stress," *American Journal of Physiology-Heart and Circulatory Physiology*, vol. 294, no. 2, pp. H909–H919, 2008.

[110] C. C. Michel and F. E. Curry, "Microvascular permeability," *Physiological Reviews*, vol. 79, no. 3, pp. 703–761, 1999.

[111] U. Förstermann, N. Xia, and H. Li, "Roles of vascular oxidative stress and nitric oxide in the pathogenesis of atherosclerosis," *Circulation Research*, vol. 120, no. 4, pp. 713–735, 2017.

[112] J. Loscalzo and J. A. Vita, *Nitric oxide and the cardiovascular system*. Springer Science & Business Media, 2000.

[113] M. U. Nollert and L. V. McIntire, "Convective mass transfer effects on the intracellular calcium response of endothelial cells," *Journal of Biomechanical Engineering*, vol. 114, no. 3, 1992.

[114] H. W. Choi, K. W. Ferrara, and A. I. Barakat, "Modulation of atp/adp concentration at the endothelial surface by shear stress: effect of flow recirculation," *Annals of Biomedical Engineering*, vol. 35, no. 4, pp. 505–516, 2007.

[115] K. John and A. I. Barakat, "Modulation of atp/adp concentration at the endothelial surface by shear stress: effect of flow-induced atp release," *Annals of Biomedical Engineering*, vol. 29, no. 9, pp. 740–751, 2001.

[116] L. Grechy, F. Iori, R. W. Corbett, W. Gedroyc, N. Duncan, C. G. Caro, and P. E. Vincent, "The effect of arterial curvature on blood flow in arterio-venous fistulae: Realistic geometries and pulsatile flow," *Cardiovascular Engineering and Technology*, vol. 8, no. 3, pp. 313–329, 2017.

[117] M. Cilla, M. A. Martínez, and E. Peña, "Effect of transmural transport properties on atheroma plaque formation and development," *Annals of Biomedical Engineering*, vol. 43, no. 7, pp. 1516–1530, 2015.

[118] H. Yu, Y. Zeng, J. Hu, and C. Li, "Fluid shear stress induces the secretion of monocyte chemoattractant protein-1 in cultured human umbilical vein endothelial cells," *Clinical Hemorheology and Microcirculation*, vol. 26, no. 3, pp. 199–207, 2002.

[119] T. David, "Wall shear stress modulation of atp/adp concentration at the endothelium," *Annals of Biomedical Engineering*, vol. 31, no. 10, pp. 1231–1237, 2003.

[120] O. Parodi, T. P. Exarchos, P. Marraccini, F. Vozzi, Z. Milosevic, D. Nikolic, A. Sakellarios, P. K. Siogkas, D. I. Fotiadis, and N. Filipovic, "Patient-specific prediction of coronary plaque growth from cta angiography: a multiscale model for plaque formation and progression," *Ieee Transactions on Information Technology in Biomedicine*, vol. 16, no. 5, pp. 952–965, 2012.

[121] P. E. Vincent and P. D. Weinberg, "Flow-dependent concentration polarization and the endothelial glycocalyx layer: multi-scale aspects of arterial mass transport and their implications for atherosclerosis," *Biomechanics and Modeling in Mechanobiology*, vol. 13, no. 2, pp. 313–326, 2014.

[122] L. H. Timmins, D. S. Molony, P. Eshtehardi, M. C. McDaniel, J. N. Oshinski, D. P. Giddens, and H. Samady, "Oscillatory wall shear stress is a dominant flow characteristic affecting lesion progression patterns and plaque vulnerability in patients with coronary artery disease," *Journal of The Royal Society Interface*, vol. 14, no. 127, p. 20160972, 2017.

[123] V. Peiffer, S. J. Sherwin, and P. D. Weinberg, "Does low and oscillatory wall shear stress correlate spatially with early atherosclerosis? a systematic review," *Cardiovascular Research*, p. cvt044, 2013.

[124] O. Smedby, "Do plaques grow upstream or downstream? an angiographic study in the femoral artery," *Arteriosclerosis, Thrombosis, and Vascular Biology*, vol. 17, no. 5, pp. 912–918, 1997.

[125] P. H. Stone, S. Saito, S. Takahashi, Y. Makita, S. Nakamura, T. Kawasaki, A. Takahashi, *et al.*, "Prediction of progression of coronary artery disease and clinical outcomes using vascular profiling of endothelial shear stress and arterial plaque characteristics: the PREDICTION study," *Circulation*, vol. 126, no. 2, pp. 172–181, 2012.

[126] C. Stefanadis, C. K. Antoniou, D. Tsiachris, and P. Pietri, "Coronary atherosclerotic vulnerable plaque: current perspectives," *Journal of the American Heart Association*, vol. 6, no. 3, p. e005543, 2017.

[127] S. Motoyama, M. Sarai, H. Harigaya, H. Anno, K. Inoue, T. Hara, H. Naruse, J. Ishii, H. Hishida, N. D. Wong, *et al.*, "Computed tomographic angiography characteristics of atherosclerotic plaques subsequently resulting in acute coronary syndrome," *Journal of the American College of Cardiology*, vol. 54, no. 1, pp. 49–57, 2009.

[128] H.-J. Chang, F. Y. Lin, S.-E. Lee, D. Andreini, J. Bax, F. Cademartiri, K. Chinnaiyan, B. J. Chow, E. Conte, R. C. Cury, *et al.*, "Coronary atherosclerotic precursors of acute coronary syndromes," *Journal of the American College of Cardiology*, vol. 71, no. 22, pp. 2511–2522, 2018.

[129] M. Ferencik, T. Mayrhofer, D. O. Bittner, H. Emami, S. B. Puchner, M. T. Lu, N. M. Meyersohn, A. V. Ivanov, E. C. Adami, M. R. Patel, *et al.*, "Use of high-risk coronary atherosclerotic plaque detection for risk stratification of patients with stable chest pain: a secondary analysis of the promise randomized clinical trial," *JAMA cardiology*, vol. 3, no. 2, pp. 144–152, 2018.

[130] M. Cilla, E. Pena, and M. A. Martinez, "Mathematical modelling of atheroma plaque formation and development in coronary arteries," *Journal of The Royal Society Interface*, vol. 11, no. 90, p. 20130866, 2014.

[131] S.-E. Lee, J. M. Sung, A. Rizvi, F. Y. Lin, A. Kumar, M. Hadamitzky, Y.-J. Kim, E. Conte, D. Andreini, G. Pontone, *et al.*, "Quantification of coronary atherosclerosis in the assessment of coronary artery disease," *Circulation: Cardiovascular Imaging*, vol. 11, no. 7, p. e007562, 2018.

[132] S. Dahal and M. J. Budoff, "Implications of serial coronary computed tomography angiography in the evaluation of coronary plaque progression," *Current opinion in lipidology*, vol. 30, no. 6, pp. 446–451, 2019.

[133] L. Saba, T. Saam, H. R. Jäger, C. Yuan, T. S. Hatsukami, D. Saloner, B. A. Wasserman, L. H. Bonati, and M. Wintermark, "Imaging biomarkers of vulnerable carotid plaques for stroke risk prediction and their potential clinical implications," *The Lancet Neurology*, 2019.

[134] H. E. Barrett, K. Van der Heiden, E. Farrell, F. J. Gijsen, and A. C. Akyildiz, "Calcifications in atherosclerotic plaques and impact on plaques biomechanics," *Journal of biomechanics*, 2019.

[135] J. M. Grimm, A. Schindler, T. Freilinger, C. C. Cyran, F. Bamberg, C. Yuan, M. F. Reiser, M. Dichgans, C. Freilinger, K. Nikolaou, *et al.*, "Comparison of symptomatic and asymptomatic atherosclerotic carotid plaques using parallel imaging and 3 t black-blood in vivo cmr," *Journal of Cardiovascular Magnetic Resonance*, vol. 15, no. 1, p. 44, 2013.

[136] R. Pelberg and W. Mazur, *Cardiac CT angiography manual*. Springer, 2015.

[137] I. J. van den Hoogen, A. R. van Rosendael, F. Y. Lin, Y. Lu, A. C. Dimitriu-Leen, J. M. Smit, A. J. Scholte, S. Achenbach, M. H. Al-Mallah, D. Andreini, *et al.*, "Coronary atherosclerosis scoring with semiquantitative ccta risk scores for prediction of major adverse cardiac events: Propensity score-based analysis of diabetic and non-diabetic patients," *Journal of Cardiovascular Computed Tomography*, 2019.

[138] A. Hoogendoorn, A. M. Kok, E. M. Hartman, G. de Nisco, L. Casadonte, C. Chiastra, A. Coenen, S.-A. Korteland, K. Van der Heiden, F. J. Gijsen, *et al.*, "Multidirectional wall shear stress promotes advanced coronary plaque development: comparing five shear stress metrics," *Cardiovascular Research*, vol. 116, no. 6, pp. 1136–1146, 2020.

[139] F. J. Gijsen, J. J. Wentzel, A. Thury, F. Mastik, J. A. Schaar, J. C. Schuurbiers, C. J. Slager, W. J. Van Der Giessen, P. J. De Feyter, A. F. Van Der Steen, *et al.*, "Strain distribution over plaques in human coronary arteries relates to shear stress," *American Journal of Physiology-Heart and Circulatory Physiology*, vol. 295, no. 4, pp. H1608–H1614, 2008.

[140] J. J. Wentzel, Y. S. Chatzizisis, F. J. Gijsen, G. D. Giannoglou, C. L. Feldman, and P. H. Stone, "Endothelial shear stress in the evolution of coronary atherosclerotic plaque and vascular remodelling: current understanding and remaining questions," *Cardiovascular research*, vol. 96, no. 2, pp. 234–243, 2012.

[141] G. De Nisco, A. Hoogendoorn, C. Chiastra, D. Gallo, A. M. Kok, U. Morbiducci, and J. J. Wentzel, "The impact of helical flow on coronary atherosclerotic plaque development," *Atherosclerosis*, 2020.

[142] S. Motoyama, T. Kondo, H. Anno, A. Sugiura, Y. Ito, K. Mori, J. Ishii, T. Sato, K. Inoue, M. Sarai, *et al.*, "Atherosclerotic plaque characterization by 0.5-mm-slice multislice computed tomographic imaging comparison with intravascular ultrasound," *Circulation Journal*, vol. 71, no. 3, pp. 363–366, 2007.

[143] E. S. Kröner, J. E. van Velzen, M. J. Boogers, H.-M. J. Siebelink, M. J. Schalij, L. J. Kroft, A. de Roos, E. E. van der Wall, J. W. Jukema, J. H. Reiber, *et al.*, "Positive remodeling on coronary computed tomography as a marker for plaque vulnerability on virtual histology intravascular ultrasound," *The American Journal of Cardiology*, vol. 107, no. 12, pp. 1725–1729, 2011.

[144] T. Pflederer, M. Marwan, T. Schepis, D. Ropers, M. Seltmann, G. Muschiol, W. G. Daniel, and S. Achenbach, "Characterization of culprit lesions in acute coronary syndromes using coronary dual-source ct angiography," *Atherosclerosis*, vol. 211, no. 2, pp. 437–444, 2010.

[145] M. G. Dalager, M. Bøttcher, G. Andersen, J. Thygesen, E. M. Pedersen, L. Dejbjerg, O. Gøtzsche, and H. E. Bøtker, "Impact of luminal density on plaque classification by ct coronary angiography," *The international journal of cardiovascular imaging*, vol. 27, no. 4, pp. 593–600, 2011.

[146] S. Schroeder, T. Flohr, A. F. Kopp, C. Meisner, A. Kuettner, C. Herdeg, A. Baumbach, and B. Ohnesorge, "Accuracy of density measurements within plaques located in artificial coronary arteries by x-ray multislice ct: results of a phantom study," *Journal of computer assisted tomography*, vol. 25, no. 6, pp. 900–906, 2001.

[147] K. T. Bae, "Intravenous contrast medium administration and scan timing at ct: considerations and approaches," *Radiology*, vol. 256, no. 1, pp. 32–61, 2010.

[148] A. Broersen, M. A. de Graaf, J. Eggermont, R. Wolterbeek, P. H. Kitslaar, J. Dijkstra, J. J. Bax, J. H. Reiber, and A. J. Scholte, "Enhanced characterization of calcified areas in intravascular ultrasound virtual histology images by quantification of the acoustic shadow: validation against computed tomography coronary angiography," *The international journal of cardiovascular imaging*, vol. 32, no. 4, pp. 543–552, 2016.

[149] M. C. de Knegt, M. Haugen, A. K. Jensen, J. J. Linde, J. T. Kühl, J. D. Hove, and K. F. Kofoed, "Coronary plaque composition assessed by cardiac computed tomography using adaptive hounsfield unit thresholds," *Clinical Imaging*, vol. 57, pp. 7–14, 2019.

[150] T. F. Chan and L. A. Vese, "Active contours without edges," *IEEE Transactions on image processing*, vol. 10, no. 2, pp. 266–277, 2001.

[151] A. F. Frangi, W. J. Niessen, K. L. Vincken, and M. A. Viergever, "Multiscale vessel enhancement filtering," in *International conference on medical image computing and computer-assisted intervention*, pp. 130–137, Springer, 1998.

[152] T. Lindeberg, "Edge detection and ridge detection with automatic scale selection," *International journal of computer vision*, vol. 30, no. 2, pp. 117–156, 1998.

[153] V. I. Kigka, G. Rigas, A. Sakellarios, P. Siogkas, I. O. Andrikos, T. P. Exarchos, D. Loggitsi, C. D. Anagnostopoulos, L. K. Michalis, D. Neglia, *et al.*, "3d reconstruction of coronary arteries and atherosclerotic plaques based on computed tomography angiography images," *Biomedical Signal Processing and Control*, vol. 40, pp. 286–294, 2018.

[154] S. Leschka, S. Seitun, M. Dettmer, S. Baumüller, P. Stolzmann, R. Goetti, H. Scheffel, G. Feuchtner, K. Wunnicke, S. Wildermuth, *et al.*, "Ex vivo evaluation of coronary atherosclerotic plaques: characterization with dual-source ct in comparison with histopathology," *Journal of cardiovascular computed tomography*, vol. 4, no. 5, pp. 301–308, 2010.

[155] M. Galonska, F. Ducke, T. Kertesz-Zborilova, R. Meyer, H. Guski, and F. D. Knollmann, "Characterization of atherosclerotic plaques in human coronary arteries with 16-slice multidetector row computed tomography by analysis of attenuation profiles," *Academic radiology*, vol. 15, no. 2, pp. 222–230, 2008.

[156] W. Kabsch, "A discussion of the solution for the best rotation to relate two sets of vectors," *Acta Crystallographica Section A: Crystal Physics, Diffraction, Theoretical and General Crystallography*, vol. 34, no. 5, pp. 827–828, 1978.

[157] W. Kabsch, "A solution for the best rotation to relate two sets of vectors," *Acta Crystallographica Section A: Crystal Physics, Diffraction, Theoretical and General Crystallography*, vol. 32, no. 5, pp. 922–923, 1976.

[158] G. Di Leo and F. Sardanelli, "Statistical significance: p value, 0.05 threshold, and applications to radiomics—reasons for a conservative approach," *European radiology experimental*, vol. 4, no. 1, pp. 1–8, 2020.

[159] P. H. Stone, A. U. Coskun, S. Kinlay, M. E. Clark, M. Sonka, A. Wahle, O. J. Ilegbusi, Y. Yeghiazarians, J. J. Popma, J. Orav, *et al.*, "Effect of endothelial shear stress on the progression of coronary artery disease, vascular remodeling, and in-stent restenosis in humans: in vivo 6-month follow-up study," *Circulation*, vol. 108, no. 4, pp. 438–444, 2003.

[160] Y. S. Chatzizisis, M. Jonas, A. U. Coskun, R. Beigel, B. V. Stone, C. Maynard, R. G. Gerrity, W. Daley, C. Rogers, E. R. Edelman, *et al.*, "Prediction of the localization of high-risk coronary atherosclerotic plaques on the basis of low endothelial shear stress: an intravascular ultrasound and histopathology natural history study," *Circulation*, vol. 117, no. 8, pp. 993–1002, 2008.

[161] J. J. Wentzel, Y. S. Chatzizisis, F. J. Gijsen, G. D. Giannoglou, C. L. Feldman, and P. H. Stone, "Endothelial shear stress in the evolution of coronary atherosclerotic plaque and vascular remodelling: current understanding and remaining questions," *Cardiovascular research*, vol. 96, no. 2, pp. 234–243, 2012.

[162] P. Eshtehardi, M. C. McDaniel, J. Suo, S. S. Dhawan, L. H. Timmins, J. N. G. Binongo, L. J. Golub, M. T. Corban, A. V. Finn, J. N. Oshinsk, *et al.*, "Association of coronary wall shear stress with atherosclerotic plaque burden, composition, and distribution in patients with coronary artery disease," *Journal of the American Heart Association*, vol. 1, no. 4, p. e002543, 2012.

[163] K. C. Koskinas, G. K. Sukhova, A. B. Baker, M. I. Papafaklis, Y. S. Chatzizisis, A. U. Coskun, T. Quillard, M. Jonas, C. Maynard, A. P. Antoniadis, *et al.*, "Thin-capped atheromata with reduced collagen content in pigs develop in coronary arterial regions exposed to persistently low endothelial shear stress," *Arteriosclerosis, thrombosis, and vascular biology*, vol. 33, no. 7, pp. 1494–1504, 2013.

[164] R. Vergallo, M. I. Papafaklis, T. Yonetsu, C. V. Bourantas, I. Andreou, Z. Wang, J. G. Fujimoto, I. McNulty, H. Lee, L. M. Biasucci, *et al.*, "Endothelial shear stress and coronary plaque characteristics in humans: combined frequency-domain optical coherence tomography and computational fluid dynamics study," *Circulation: Cardiovascular Imaging*, vol. 7, no. 6, pp. 905–911, 2014.

[165] M. I. Papafaklis, S. Takahashi, A. P. Antoniadis, A. U. Coskun, M. Tsuda, S. Mizuno, I. Andreou, S. Nakamura, Y. Makita, A. Hirohata, *et al.*, "Effect of the local hemodynamic environment on the de novo development and progression of eccentric coronary atherosclerosis in humans: insights from prediction," *Atherosclerosis*, vol. 240, no. 1, pp. 205–211, 2015.

[166] D. Han, A. Starikov, B. ó Hartaigh, H. Gransar, K. K. Kolli, J. H. Lee, A. Rizvi, L. Baskaran, J. Schulman-Marcus, F. Y. Lin, *et al.*, "Relationship between endothelial wall shear stress and high-risk atherosclerotic plaque characteristics for identification of coronary lesions that cause ischemia: a direct comparison with fractional flow reserve," *Journal of the American Heart Association*, vol. 5, no. 12, p. e004186, 2016.

[167] L. H. Timmins, D. S. Molony, P. Eshtehardi, M. C. McDaniel, J. N. Oshinski, D. P. Giddens, and H. Samady, "Oscillatory wall shear stress is a dominant flow characteristic affecting lesion progression patterns and plaque vulnerability in patients with coronary artery disease," *Journal of The Royal Society Interface*, vol. 14, no. 127, p. 20160972, 2017.

[168] L. Euler, "Principia pro motu sanguinis per arterias determinando: Chapter opera posthuma mathematica et physica anno 1844 detecta," *Ediderunt Ph Fuss et N Fuss Petropoli, Eggers et socios*, vol. 2, pp. 814–823, 1844.

[169] L. Formaggia and A. Veneziani, "Reduced and multiscale models for the human cardiovascular system," *Lecture notes VKI lecture series*, vol. 7, 2003.

[170] F. Nobile, "Coupling strategies for the numerical simulation of blood flow in deformable arteries by 3d and 1d models," *Mathematical and Computer Modelling*, vol. 49, no. 11-12, pp. 2152–2160, 2009.

[171] C. Leguy, E. Bosboom, H. Gelderblom, A. Hoeks, and F. Van de Vosse, "Estimation of distributed arterial mechanical properties using a wave propagation model in a reverse way," *Medical engineering & physics*, vol. 32, no. 9, pp. 957–967, 2010.

[172] M. S. Olufsen, "Structured tree outflow condition for blood flow in larger systemic arteries," *American journal of physiology-Heart and circulatory physiology*, vol. 276, no. 1, pp. H257–H268, 1999.

[173] P. Reymond, F. Merenda, F. Perren, D. Rufenacht, and N. Stergiopulos, "Validation of a one-dimensional model of the systemic arterial tree," *American Journal of Physiology-Heart and Circulatory Physiology*, vol. 297, no. 1, pp. H208–H222, 2009.

[174] M. Willemet, V. Lacroix, and E. Marchandise, "Validation of a 1d patient-specific model of the arterial hemodynamics in bypassed lower-limbs: simulations against in vivo measurements," *Medical engineering & physics*, vol. 35, no. 11, pp. 1573–1583, 2013.

[175] C. M. Quick, W. L. Young, and A. Noordergraaf, "Infinite number of solutions to the hemodynamic inverse problem," *American Journal of Physiology-Heart and Circulatory Physiology*, vol. 280, no. 4, pp. H1472–H1479, 2001.

[176] P. J. Blanco, S. M. Watanabe, E. A. Dari, M. A. R. Passos, and R. A. Feijóo, "Blood flow distribution in an anatomically detailed arterial network model: criteria and algorithms," *Biomechanics and modeling in mechanobiology*, vol. 13, no. 6, pp. 1303–1330, 2014.

[177] S. Epstein, M. Willemet, P. J. Chowienczyk, and J. Alastruey, "Reducing the number of parameters in 1d arterial blood flow modeling: less is more for patient-specific simulations," *American Journal of Physiology-Heart and Circulatory Physiology*, vol. 309, no. 1, pp. H222–H234, 2015.

[178] P. Perdikaris, L. Grinberg, and G. E. Karniadakis, "An effective fractal-tree closure model for simulating blood flow in large arterial networks," *Annals of biomedical engineering*, vol. 43, no. 6, pp. 1432–1442, 2015.

[179] J. G. Isaksen, Y. Bazilevs, T. Kvamsdal, Y. Zhang, J. H. Kaspersen, K. Waterloo, B. Romner, and T. Ingebrigtsen, "Determination of wall tension in cerebral artery aneurysms by numerical simulation," *Stroke*, vol. 39, no. 12, pp. 3172–3178, 2008.

[180] M. Mahmoudi, C. Jennings, K. Pereira, A. F. Hall, and A. Arzani, "Guiding the prostatic artery embolization procedure with computational uid dynamics," *Journal of Biomechanical Engineering*, 2022.

[181] M. Mahmoudi, A. Farghadan, D. R. McConnell, A. J. Barker, J. J. Wentzel, M. J. Budoff, and A. Arzani, "The story of wall shear stress in coronary artery atherosclerosis: biochemical transport and mechanotransduction," *Journal of Biomechanical Engineering*, vol. 143, no. 4, 2021.

[182] L. Zhong, J.-M. Zhang, B. Su, R. S. Tan, J. C. Allen, and G. S. Kassab, "Application of patient-specific computational fluid dynamics in coronary and intra-cardiac flow simulations: Challenges and opportunities," *Frontiers in physiology*, vol. 9, p. 742, 2018.

[183] D. Lopes, H. Puga, J. Teixeira, and R. Lima, "Blood flow simulations in patient-specific geometries of the carotid artery: A systematic review," *Journal of Biomechanics*, vol. 111, p. 110019, 2020.

[184] C. Chiastra, S. Migliori, F. Burzotta, G. Dubini, and F. Migliavacca, "Patient-specific modeling of stented coronary arteries reconstructed from optical coherence tomography: Towards a widespread clinical use of fluid dynamics analyses," *Journal of cardiovascular translational research*, vol. 11, no. 2, pp. 156–172, 2018.

[185] A. Razavi, S. Sachdeva, P. C. Frommelt, and J. F. LaDisa Jr, "Patient-specific numerical analysis of coronary flow in children with intramural anomalous aortic origin of coronary arteries," in *Seminars in Thoracic and Cardiovascular Surgery*, vol. 33, pp. 155–167, Elsevier, 2021.

[186] P. J. Blanco, M. Pivello, S. Urquiza, and R. Feijóo, "On the potentialities of 3d–1d coupled models in hemodynamics simulations," *Journal of biomechanics*, vol. 42, no. 7, pp. 919–930, 2009.

[187] S. Urquiza, P. Blanco, M. Vénere, and R. Feijóo, "Multidimensional modelling for the carotid artery blood flow," *Computer Methods in Applied Mechanics and Engineering*, vol. 195, no. 33-36, pp. 4002–4017, 2006.

[188] Z. Chi, L. Beile, L. Deyu, and F. Yubo, "Application of multiscale coupling models in the numerical study of circulation system," *Medicine in Novel Technology and Devices*, p. 100117, 2022.

[189] P. Blanco, S. Urquiza, and R. Feijóo, "Assessing the influence of heart rate in local hemodynamics through coupled 3d-1d-0d models," *International Journal for Numerical Methods in Biomedical Engineering*, vol. 26, no. 7, pp. 890–903, 2010.

[190] A. Updegrove, N. M. Wilson, J. Merkow, H. Lan, A. L. Marsden, and S. C. Shadden, "Simvascular: an open source pipeline for cardiovascular simulation," *Annals of biomedical engineering*, vol. 45, no. 3, pp. 525–541, 2017.

[191] M. J. Grote and J. B. Keller, "Exact nonreflecting boundary conditions for the time dependent wave equation," *SIAM Journal on Applied Mathematics*, vol. 55, no. 2, pp. 280–297, 1995.

[192] I. Patlashenko, D. Givoli, and P. Barbone, "Time-stepping schemes for systems of volterra integro-differential equations," *Computer methods in applied mechanics and engineering*, vol. 190, no. 43-44, pp. 5691–5718, 2001.

[193] SimVascular, "Genbc tutorial," 2022.

[194] N. Xiao, J. Alastruey, and C. Alberto Figueroa, "A systematic comparison between 1-d and 3-d hemodynamics in compliant arterial models," *International journal for numerical methods in biomedical engineering*, vol. 30, no. 2, pp. 204–231, 2014.

[195] Q. Fang, S. Sakadžić, L. Ruvinskaya, A. Devor, A. M. Dale, and D. A. Boas, "Oxygen advection and diffusion in a three-dimensional vascular anatomical network," *Optics express*, vol. 16, no. 22, pp. 17530–17541, 2008.

[196] F. Schmid, P. S. Tsai, D. Kleinfeld, P. Jenny, and B. Weber, "Depth-dependent flow and pressure characteristics in cortical microvascular networks," *PLoS computational biology*, vol. 13, no. 2, p. e1005392, 2017.

[197] F. Cassot, F. Lauwers, C. Fouard, S. Prohaska, and V. Lauwers-Cances, "A novel three-dimensional computer-assisted method for a quantitative study of microvascular networks of the human cerebral cortex," *Microcirculation*, vol. 13, no. 1, pp. 1–18, 2006.

[198] W. K. El-Bouri and S. J. Payne, "Multi-scale homogenization of blood flow in 3-dimensional human cerebral microvascular networks," *Journal of theoretical biology*, vol. 380, pp. 40–47, 2015.

[199] M. Peyrounette, Y. Davit, M. Quintard, and S. Lorthois, "Multiscale modelling of blood flow in cerebral microcirculation: Details at capillary scale control accuracy at the level of the cortex," *PloS one*, vol. 13, no. 1, p. e0189474, 2018.

[200] K. Kidoguchi, M. Tamaki, T. Mizobe, J. Koyama, T. Kondoh, E. Kohmura, T. Sakurai, K. Yokono, and K. Umetani, "In vivo x-ray angiography in the mouse brain using synchrotron radiation," *Stroke*, vol. 37, no. 7, pp. 1856–1861, 2006.

[201] G. S. Kassab, C. A. Rider, N. J. Tang, and Y.-C. Fung, "Morphometry of pig coronary arterial trees," *American Journal of Physiology-Heart and Circulatory Physiology*, vol. 265, no. 1, pp. H350–H365, 1993.

[202] M. Georg, T. Preusser, and H. K. Hahn, "Global constructive optimization of vascular systems," 2010.

[203] M. H. Tawhai, A. Pullan, and P. Hunter, "Generation of an anatomically based three-dimensional model of the conducting airways," *Annals of biomedical engineering*, vol. 28, no. 7, pp. 793–802, 2000.

[204] S. R. Aylward and E. Bullitt, "Initialization, noise, singularities, and scale in height ridge traversal for tubular object centerline extraction," *IEEE transactions on medical imaging*, vol. 21, no. 2, pp. 61–75, 2002.

[205] L. Papamanolis, H. J. Kim, C. Jaquet, M. Sinclair, M. Schaap, I. Danad, P. van Diemen, P. Knaapen, L. Najman, H. Talbot, *et al.*, "Myocardial perfusion simulation for coronary artery disease: a coupled patient-specific multiscale model," *Annals of biomedical engineering*, vol. 49, no. 5, pp. 1432–1447, 2021.

[206] M. Schneider, J. Reichold, B. Weber, G. Székely, and S. Hirsch, "Tissue metabolism driven arterial tree generation," *Medical image analysis*, vol. 16, no. 7, pp. 1397–1414, 2012.

[207] G. Hamarneh and P. Jassi, "Vascusynth: Simulating vascular trees for generating volumetric image data with ground-truth segmentation and tree analysis," *Computerized medical imaging and graphics*, vol. 34, no. 8, pp. 605–616, 2010.

[208] J. Keelan, E. M. Chung, and J. P. Hague, "Simulated annealing approach to vascular structure with application to the coronary arteries," *Royal Society open science*, vol. 3, no. 2, p. 150431, 2016.

[209] C. Jaquet, L. Najman, H. Talbot, L. Grady, M. Schaap, B. Spain, H. J. Kim, I. Vignon-Clementel, and C. A. Taylor, "Generation of patient-specific cardiac vascular networks: a hybrid image-based and synthetic geometric model," *IEEE Transactions on Biomedical Engineering*, vol. 66, no. 4, pp. 946–955, 2018.

[210] R. Karch, F. Neumann, M. Neumann, and W. Schreiner, "A three-dimensional model for arterial tree representation, generated by constrained constructive optimization," *Computers in biology and medicine*, vol. 29, no. 1, pp. 19–38, 1999.

[211] S. G. Johnson, "The nlopt nonlinear-optimization package," 2022.

[212] M. J. Powell, "A direct search optimization method that models the objective and constraint functions by linear interpolation," in *Advances in optimization and numerical analysis*, pp. 51–67, Springer, 1994.